Steel joint ductility - coupling and membrane effects in adjacent T-stubs

Auteur : Gillieaux, Margaux
Promoteur(s) : Demonceau, Jean-François
Faculté : Faculté des Sciences appliquées
Diplôme : Master en ingénieur civil des constructions, à finalité spécialisée en "civil engineering"
Année académique : 2024-2025
URI/URL : http://hdl.handle.net/2268.2/23337

University of Liège
Faculty of Applied Sciences

Steel joint ductility - coupling and membrane effects in adjacent T-stubs

Master's thesis completed to obtain the degree of

Master in Civil Engineering conducted by Gillieaux Margaux

Supervisor :
J-F. Demonceau

Jury :
A. Neutelers
L. Duchene
M. Latour

Academic Year
2024 – 2025

Acknowledgements

First and foremost, I would like to express my deepest gratitude to my mentor and supervisor, Jean-François Demonceau, for his expertise and for giving me the opportunity to work in such a fascinating and complex field. The robustness of buildings is a subject particularly meaningful to me, especially given its connection to the events of September 11th, which coincides with my birthdate. His guidance, pedagogy, and constructive advice have been indispensable to the completion of this thesis.

I would also like to extend my heartfelt appreciation to Arnaud Neutelers, who has been an invaluable support throughout my research, always available to assist me. His kindness and scientific rigor greatly contributed to the refinement of my work.

I would further like to sincerely thank the members of my thesis committee, L. Duchene and M. Latour, for their time and dedication in evaluating this work.

I am equally grateful to my friends both within and outside the university sphere who have consistently supported me throughout my studies. Their friendship and encouragement have helped me reach the completion of this thesis and this study with joy and serenity.

Last but not least, I want to thank my parents, my sisters, and my partner for their unwavering support during both the highs and lows of this journey. Their encouragement, support, and love have given me the confidence to believe in my abilities.

Abstract

Title : Steel joint ductility - coupling and membrane effects in adjacent T-stubs

The robustness of buildings constitutes a major and recurring challenge in the construction sector. The resistance of the joints plays a key role in the evaluation of the performance of a structure facing a catastrophic event. Furthermore, the reuse of construction elements is established as a second major objective aiming to reduce the environmental impact of the sector.

The study of metallic joints is thus a central subject, with a particular interest in T-stubs, components of many joints. The main objective of this work is to contribute to a better understanding of the behaviour of T-stubs.

The methodology adopted in this thesis relies first on a literature review, presenting different existing analytical models as well as a critical analysis of available experimental studies.

Two of the specimens from these experimental studies were numerically modelled in order to validate the relevance of the numerical modelling.

Following this validation, a parametric study was conducted, varying three dimensionless parameters. The results obtained allowed to reassess certain parameters used in the Eurocode 3 analytical model, notably regarding the inaccurate prediction of the positions of the plastic hinges. This study also highlighted the emergence of membrane effects and coupling effects.

This effect manifests when the base, a T-stub thicker than the one studied, itself undergoes deformation. This phenomenon, rarely addressed in the literature, opens new promising research perspectives, notably regarding the possibility of a ductility reserve, as was incidentally observed in the work of Faralli.

This effect can therefore offer great prospects in the field of robustness. On the other hand, this significant ductility reserve could become a major challenge in the development of innovations for the reuse of metallic elements.

Résumé

Titre : Ductilité des assemblages en acier - effets de couplage et effets membranaires pour des T-stubs adjacents

La robustesse des bâtiments constitue un défi majeur et récurrent dans le secteur de la construction. La résistance des assemblages joue un rôle clé dans l'évaluation de la tenue d'un ouvrage face à un événement catastrophique. Par ailleurs, la réutilisation des éléments de construction s'inscrit comme un second objectif majeur visant à réduire l'impact environnemental du secteur.

L'étude des assemblages métalliques est ainsi un sujet central, avec un intérêt particulier pour les T-stubs, composants de nombreux assemblages. L'objectif principal de ce travail est de contribuer à une meilleure compréhension du comportement des T-stubs.

La méthodologie adoptée dans cette thèse s'appuie d'abord sur une revue de la littérature, présentant différents modèles analytiques existants ainsi qu'une analyse critique des études expérimentales disponibles.

Deux des specimens de ces études expérimentales ont été modélisés numériquement afin de valider la pertinence de la modélisation numérique.

À la suite de cette validation, une étude paramétrique a été menée, faisant varier trois paramètres adimensionnels. Les résultats obtenus ont permis de réintérroger certains paramètres utilisés dans le modèle analytique de l'Eurocode 3, notamment en ce qui concerne la prédiction erronées des localisations des rotules plastiques. Cette étude a également mis en évidence l'apparition d'effets membranaires et d'effets de couplage.

Cet effet se manifeste lorsque la base, un T-stub plus épais que celui étudié, subit elle-même une déformation. Ce phénomène, peu abordé dans la littérature, ouvre de nouvelles perspectives de recherche prometteuses, notamment quant à la possibilité d'une réserve de ductilité, comme cela a été de manière fortuite observé dans les travaux de Faralli.

Cet effet peut donc offrir de grandes perspectives dans le domaine de la robustesse. En revanche, cette réserve de ductilité importante pourrait représenter un défi majeur dans le développement d'innovations pour la réutilisation des éléments métalliques.

Nomenclature

χ	The moment-curvature relationship
Δ	A displacement
Δ_e	The T-stub elastic displacement
Δ_p	The T-stub plastic displacement
Δ_u	The T-stub ultimate displacement
Δ_y	The T-stub displacement at yielding
ϵ_{eng}	The engineering strain
δ_{H1}	The distance between the weld toe and the first plastic hinge
δ_{H2}	The distance between the bolt axis and the second plastic hinge
ϵ	A strain
ϵ_h	The strain at the end of the plastic strain
$\epsilon_{h,true}$	The true strain associated to the strain at the end of the plastic strain
$\epsilon_{m,true}$	The true strain associated to the ultimate strain
ϵ_{sh}	The strain at the end of the plastic strain
ϵ_{true}	The true strain
ϵ_u	The ultimate strain of steel
$\epsilon_{u,b}$	The ultimate strain of the bolt
$\epsilon_{u,true}$	The true ultimate strain
ϵ_y	The yielding strain of a steel
$\epsilon_{y,b}$	The yielding strain of the bolt
λ	The ratio of m and n
ϕ	The relative rotation of a joint
σ	A stress
σ_{eng}	The engineering stress
σ_{true}	The true stress
θ_p	The plastic rotation of a plastic hinge
ζ	A parameter introduced to simplify the bolt head work equation in the Neutelers model
a'	The distance between the point located at 50% of the projection of the weld thickness and the inner edge of bolt hole
a_c	The weld thickness in the Faralli campaign
a_w	The weld thickness

A_s	The area of the threaded shaft of bolt
B	The width of the T-stub or the bolt load
b'	The distance between the prying force location and the inner edge of the bolt hole
b_f	The length of the T-stub
b_p	The length of the T-stub
$B_{T,Rd}$	The plastic strength of one bolt
$B_{u,Rd}$	The ultimate strength of one bolt
C	The distance between the weld toe and the bolt axis
d_b	The diameter of a bolt
d_e	The distance between the bolt axis and the flange edge in the width direction
d_h	The diameter of a bolt hole
d_{plate}	The base thickness
d_w	The washer diameter
E	The Young modulus
e	The distance between the bolt axis and the flange edge in the width direction
E_b	The Young modulus of bolt
$E_{h,true}$	The true hardening modulus
$E_{u,true}$	The true ultimate modulus
e_w	The distance between the bolt axis and the equivalent bolt load point of application
F	An effort
$f_{m,true}$	The true stress associated to the ultimate stress and ultimate strain
F_{pl}	The plastic strength
$F_{T,Rd}$	The plastic strength of the T-stub
$F_{T,1,Rd}$	The plastic strength of mode 0, without prying force
$F_{T,1,Rd}$	The plastic strength of mode 1
$F_{T,2,Rd}$	The plastic strength of mode 2
$F_{T,3,Rd}$	The plastic strength of mode 3
f_u	The ultimate stress of steel
F_u	The ultimate force
$f_{u,b}$	The ultimate stress of bolt
f_y	The yielding stress of steel
F_y	The plastic force
$f_{y,b}$	The yielding stress of bolt
g	The distance between two bolt rows
G	A parameter introduced to simplify the bolt head work equation in Neutelers model

h	The width of the T-stub
h_f	The projection of the weld thickness
I	The bending inertia
k_{base}	The stiffness of a base
k_{bolt}	The stiffness of a bolt
k_{plate}	The stiffness of a plate
k_{eff}	The initial stiffness of a T-stub
k_{rel}	The stiffness ratio of the bolt to the plate
L	The length of the T-stub
L_b	The bolt length
$l_{eff,1}$	The effective length of mode 1
$l_{eff,2}$	The effective length of mode 2
$l_{eff,c}$	The effective length of the circular yield line pattern
$l_{eff,c,Neutelers}$	The effective length of Neutelers circular yield line pattern
$l_{eff,c,Warnant}$	The effective length of Warnant circular yield line pattern
$l_{eff,nc,1}$	The effective length of the short yield line pattern
$l_{eff,nc,2}$	The effective length of Zoetemeijer yield line pattern
l_{head}	The length of the head of bolt
l_{nut}	The length of the nut of bolt
l_w	The length of the washer
m	The distance between the bolt axis and the point located at 80% of the projection of the weld thickness
M	A bending moment
M_j	The bending moment transmitted by a joint
M_p	The plastic bending moment
m_{pl}	The plastic bending moment per unit of length
$M_{pl,1,Rd}$	The plastic bending moment of mode 1
$M_{pl,2,Rd}$	The plastic bending moment of mode 2
M_u	The ultimate bending moment
n	The distance between the bolt axis and the prying forces location
p_f	The distance between the web and the bolt axis
Q	The prying force
$S_{j,ini}$	The rotational stiffness of a joint
T	The plastic resistance in the Struik and De back model
t_f	The flange thickness
t_p	The flange thickness
t_w	The web thickness
w	The distance between two bolt rows

Contents

Chapter 1

Introduction

1.1 Technical context

Historically, research in structural engineering primarily focused on calculating the resistance of individual elements or entire structures. The primary objective was to determine whether a given element could withstand specific loads.

However, the construction field has faced several catastrophic events, such as the 9/11 attacks. This monumental tragedy prompted a paradigm shift in the approach of designing buildings and structures. Beyond ensuring that a structure can resist various loads without experiencing excessive deformations, there is now a focus on understanding how a structure behaves when subjected to extreme events, such as localized explosions or partial structural failures. The goal is to improve the robustness of a structure. One of the key factors contributing to this robustness is the ductility of structural joints.

A structure is analysed under specific scenarios, such as the sudden loss of a column, to ensure that the remaining structure can sustain its integrity for a sufficient period to allow for a safe evacuation of the building. In such cases, all structural elements must be designed with an adequate safety margin to account for these extreme conditions.

Initially, the behaviour of connections and assemblies within structures was not a primary research focus. However, advancements in structural engineering research have significantly expanded the understanding of joint behaviour and its critical role in the overall performance and resilience of structures.

At this stage, the behaviour of the assemblies has been explored at a preliminary level. However, there remains several important aspects that would benefit from further investigation and detailed analysis in order to gain a comprehensive understanding of their response up to the ultimate load.

Previously, Warnant A. [**1**] developed a thesis at the University of Liège focusing on the behaviour of metallic construction joints. Additionally, this work is closely related to the thesis of Neutelers A. [**2**], who studied the behavior of T-stub elements symmetricaly bolted. Their research provided significant insights but also raised new questions.

It is of particular interest to extend this line of research by investigating a comparable configuration in which the T-stub element is connected to a rigid base. Furthermore, this thesis supports the broader objective of promoting material reuse in construction, and may, for instance, provide valuable insights for the design of fusible assemblies.

1.2 Objectives

The objective of this study is to evaluate whether the findings presented by Neutelers A. [**2**] can be generalized to an alternative configuration, thereby contributing to a more comprehensive understanding of the structural behaviour of such assemblies.

In addition, this thesis aims to contribute to the broader objectives of enhancing structural robustness and promoting the reusability of structural components.

1.3 Methodology

To address this research question, a combined approach involving literature review, experimental study, and numerical modelling was adopted. Following the selection of a relevant experimental campaign, two representative cases of short T-stubs were chosen to be reproduced numerically using the Abaqus software. The validity of the numerical model was assessed by comparing its results with available experimental data. Once validated, a parametric analysis was carried out to investigate the influence of key geometric parameters on the mechanical behaviour of the connection used in the Eurocode 3. For example, the variation of the base plate thickness was examined to explore configurations ranging from a symmetric setup to a deep base, which can be considered as rigid.

Chapter 2

State-of-the-art

This chapter focuses on the current state of the literature regarding the behaviour of a T-stub. It begins with an overview, starting with the component method, an approach used to characterize a structural joint. The second part of this chapter defines the T-stub and its key characteristics. Finally, the main existing model and three improved models are used and explained in this section.

2.1 Characterization of a joint

2.1.1 Classification of a joint

A joint consists of one or more components designed to connect two elements, such as two columns, two beams, or a beam and a column. For simplicity, it is often modelled as either a hinged connection or a fully rigid connection. These two idealized situations were commonly used in the past. However, the actual behaviour is typically found between these two idealized cases. Three parameters are used to characterize the joint [**3**]: *rotational stiffness* ($S_{j,ini}$), *transmitted bending moment* (M_j) and *the relative rotation* between the two components of the joint (ϕ).

The three factors are illustrated in Figure 2.1.

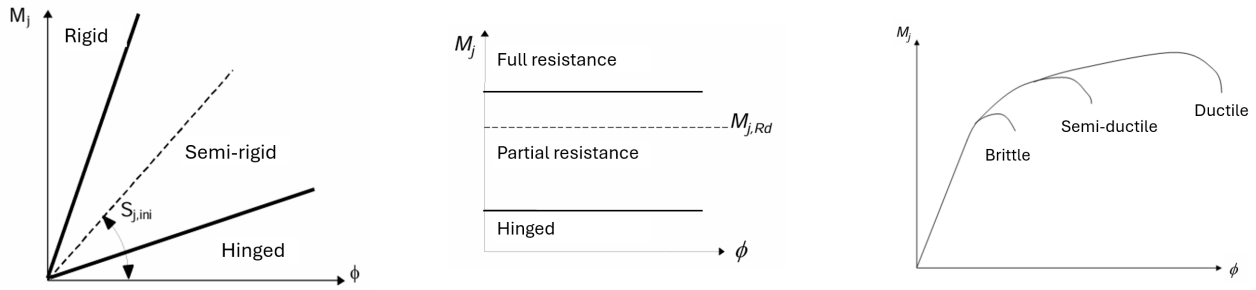

(a) Stiffness (b) Resistance (c) Ductility

Figure 2.1: The classification of the joint [**2**]

- **The stiffness**: The boundary for determining the category of the studied joint is based on the initial rotational stiffness ($S_{j,ini}$). The limits are proportional to the term $\frac{E \cdot I}{L}$ which represents flexural stiffness on the length as detailed in [**4**].
- **The resistance** : The resistance is characterized by the maximum bending moment that the joint can transmit.
- **The ductility** : The ductility is characterized by the relative rotation (ϕ) between the axis of the connected members. [**5**]

2.1.2 The component method

The component method is used to model the assembly as a sum of multiple smaller elements. Each element contributes to the joint response and is referred to as a *component*. The first step in applying *the component method* is to identify each component of the studied joint. For instance, if the assembly between a column and a beam is considered as shown on the Figure 2.2, each component must be identified individually. In general, three main zones can be highlighted: compression zone, tension zone and shear zone.

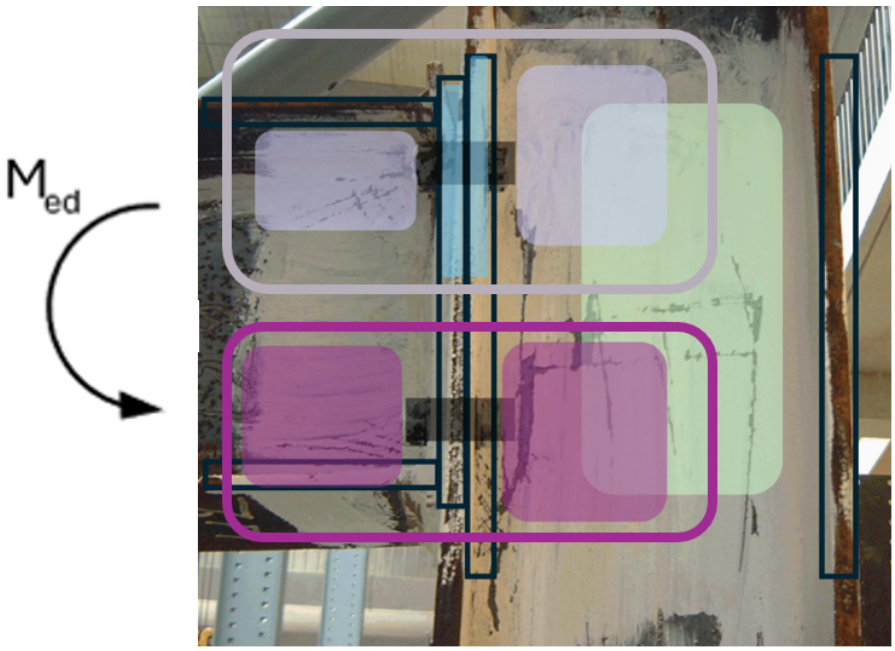

Figure 2.2: Identification of principal zones on the pictures from the source [**3**]

In this example, a bending moment is applied to the joint. This bending moment can be modelled as two axial forces acting on the two flanges of the beam: tension in the upper flange and compression in the lower flange. The height of the beam can be seen as the lever arm.

In the compression zone, *the lower part of the beam's web and the flange* are parts of the assembly and are in compression. This compressive force is transmitted directly through contact with *the flange of the column*.

In the tension zone, the tension in the *upper part of the beam's web* transfers the force to *the end plate of the beam in bending*. The force is then applied to *the flange of the column in bending* via *the bolts in tension*. Finally, *the upper part of the column* is in tension because of the direct connection.

Due to the bending moment, the lower part of the beam's web is in compression, while the upper part is in tension. This situation leads to the formation of a shear zone on the web.

All components are shown in the schematic in Figure 2.3. Each component contributes, to varying degrees, to the transfer of the bending moment from the beam to the column.

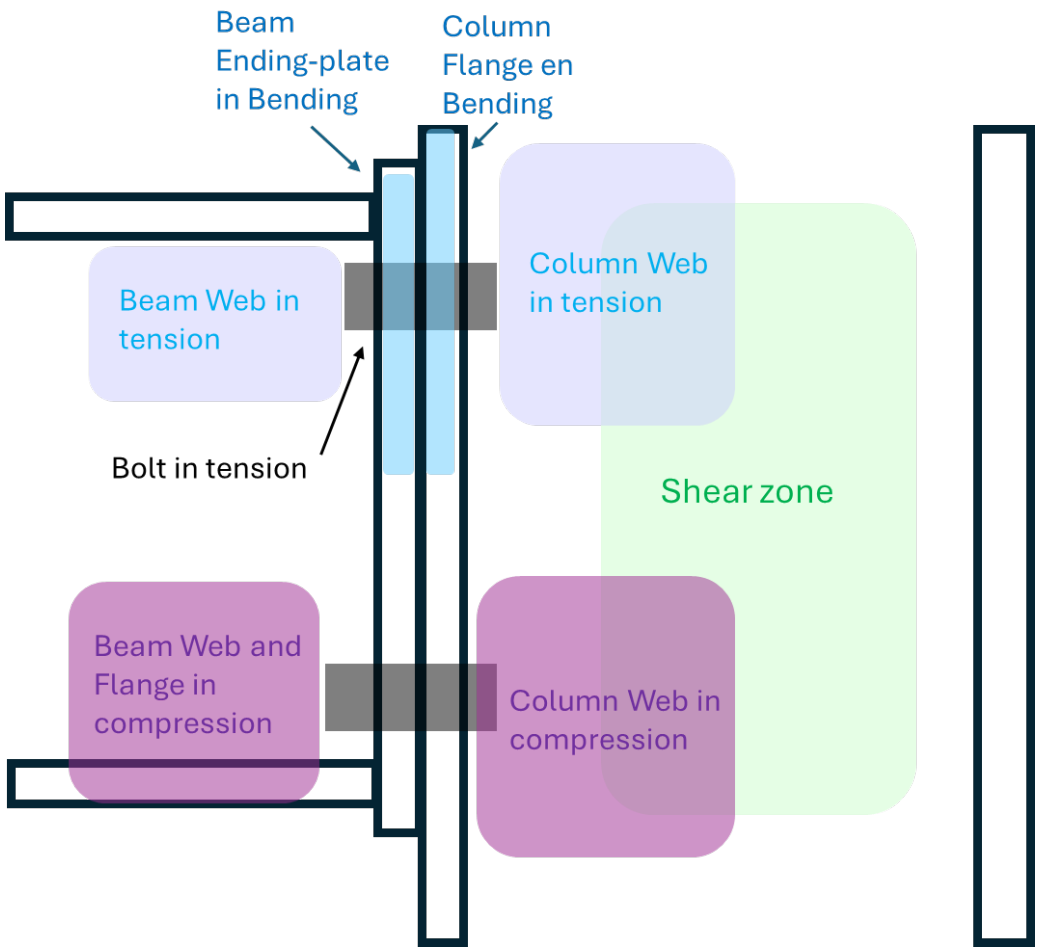

Figure 2.3: Identification of the components

Now that each component has been identified, they can be characterized according to Eurocode 3 [4]. Each component can be modelled by dashpots or springs. In the joint studied, the spring model is as shown in Figure 2.4.

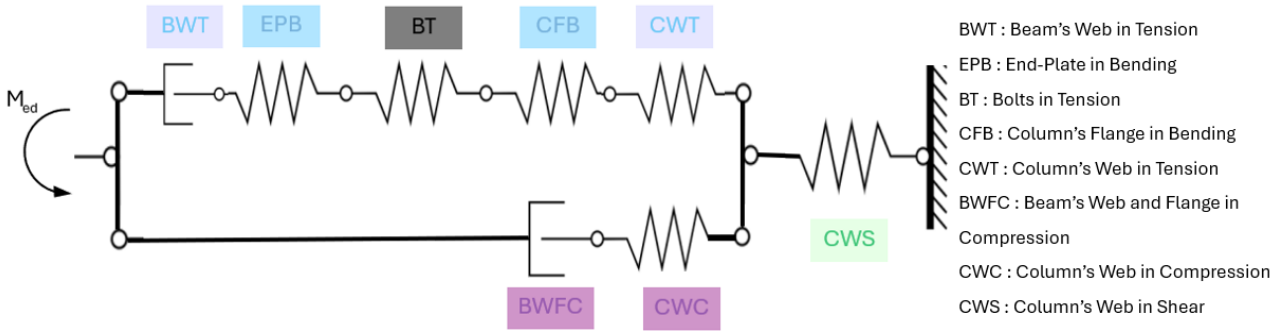

Figure 2.4: Spring model of the analysed case [4]

This type of assembly is quite common. In such a joint, the End-Plate in Bending, Bolts in Tension, and the Column Flange in Bending can be modelled as equivalent unstiffened components.

Once all these steps are completed, the different components can be assembled to characterize the overall joint using static equilibrium principles.

In this final step, all the springs and dashpots are combined into a single *effective spring* characterized by an effective stiffness and a relative rotation.

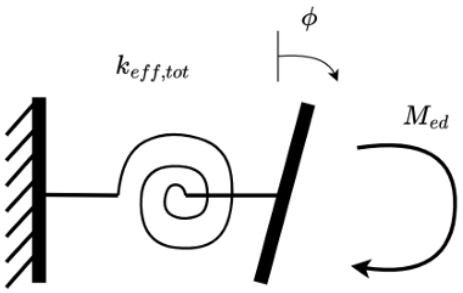

Figure 2.5: Equivalent torsional spring [**4**]

The joint is now fully characterized and can be used in analyses to determine, for example, the displacement of a structure. However, the behaviour of the T-stub may still not be fully defined specially at the ultimate state.

2.2 The T-stub

As explained previously, each joint can be characterized using *the component method*. A joint with a flange in bending and a end plate in bending connected with bolts can be identified and compared to *an equivalent T-stub*. In fact, the portion of the component under tension can be modelled as a T-stub.

In general, a T-stub consists of two metal plates welded together in the shape of a T. Then, this structure is bolted to another T-stub or another plate. It allows the transfer of forces between two elements.

The T-stub is characterized by several parameters, which can be seen in Figure 2.6.

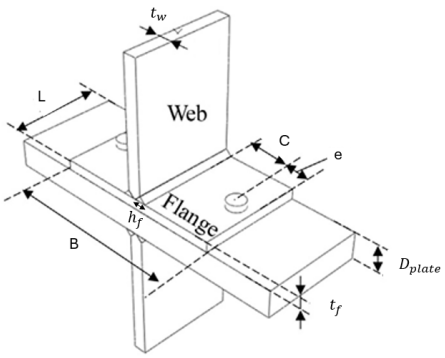

(a) Scheme from the experimental article [**11**]

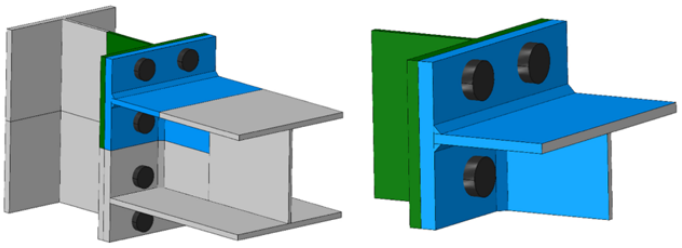

(b) Design from the experimental article [**15**]

Figure 2.6: Visualization of a T-stub

2.2.1 The three failure modes

Typically, a T-stub is subjected to a tensile force applied to the web. In such cases, the bolts attempt to anchor the flange of the T-stub to its base or to a second T-stub. Between the force applied to the web and the resistance of the bolts, deformations are observed.

Under such loading, the T-stub undergoes progressive deformation until failure occurs. Based on numerous experimental investigations, three distinct failure modes have been identified.

- **Mode 1**

In this first configuration, *two plastic hinges* can be observed: one close to the weld toe and the other at the bolt hole axis. *Prying forces* develop at the edges of the flange and overload the bolts.

During the loading phase, the bolts attempt to anchor the flange, and a deformation grows progressively until the formation of *a plastic hinge at the weld toe*. Subsequently, prying forces develop on the exterior of the bolt. As loading increases, another plastic hinge is formed, following a yield line pattern along the axis of the bolt.

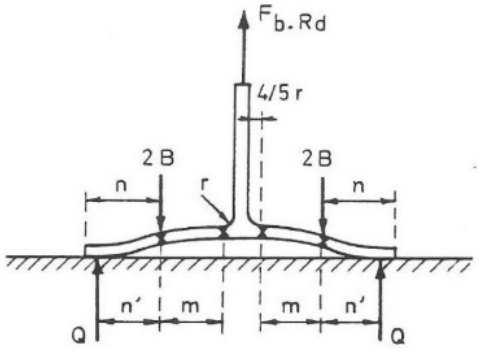

Figure 2.7: Mode of failure 1 [**3**]

Following the evolution, mode 1 can be studied according to 2 different methods. The first one, present in the Eurocode 3, defines the resistance with the formula :

$$F_{T,1,Rd} = \frac{4 \cdot M_{pl,1,Rd}}{m} = \frac{4 \cdot m_{pl} \cdot L_{eff,1}}{m} \tag{2.1}$$

In this situation, the force B of the bolt, shown in Figure 2.7, is considered as *a point force* on the bolt axis, and the prying force is a point force applied at the edge of the flange.

A more precise formula was developed by J.-P. Jaspart [**5**], which is now include in the Eurocode 3 [**4**], leading to the following expression:

$$F_{T,1,Rd} = \frac{M_{pl,1,Rd} \cdot (32 \cdot n + 2 \cdot d_w)}{8 \cdot m \cdot n - d_w(m+n)} \tag{2.2}$$

The parameter m and n are distances defined in Figure 2.8. d_w denotes the diameter of the washer, while $M_{pl,1,Rd}$ refers to the product of *the effective length* and *the plastic bending moment per unit length*.

The difference from the previous situation is that the force applied by the bolt is not considered as a point force (Figure 2.8a) but is *uniformly distributed* (Figure 2.8b) across the diameter of the washer. With this consideration, a portion of the bolt contributes to virtual work as it restrains part of the flange's displacements.

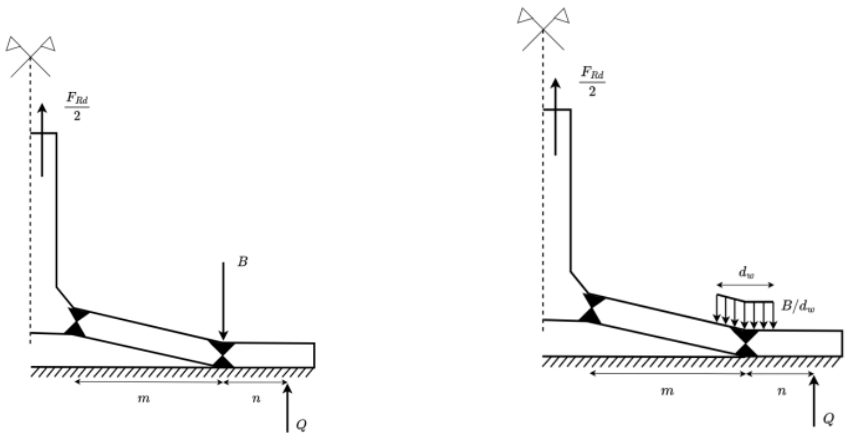

(a) Method 1 (b) Method 2

Figure 2.8: Difference of the 2 methods of the Eurocode 3 for the failure mode 1 [**2**]

- **Mode 2**

In the second mode, the geometry of the T-stub is such that *one plastic hinge* develops at the weld toe. The prying force overloads the bolts that they reach failure before the formation of a second plastic hinge.

This intermediate state has a resistance calculated according to the formula :

$$F_{T,2,Rd} = \frac{2 \cdot M_{pl,2,Rd} + n \cdot \sum B_{T,Rd}}{m + n} \tag{2.3}$$

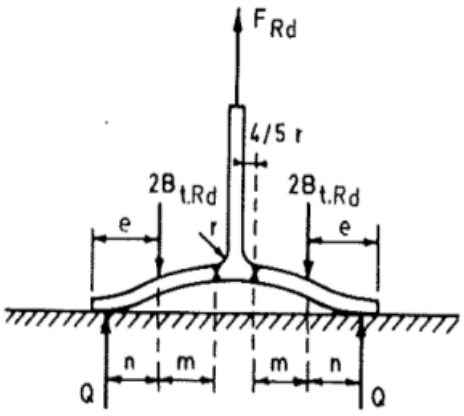

Figure 2.9: Mode of failure 2 [**3**]

In this formula, the distance parameters m and n are used just as $M_{pl,2,Rd}$ which corresponds to *the plastic bending moment associated with the second mode*. This moment is the product of *the effective length* corresponding to the mode 2 and the plastic bending moment per unit length. In this second mode, the plastic strength for the bolts is taken into account.

- **Mode 3**

The last mode is governed by *the failure of the bolts*. Before the formation of plastic hinge, the bolts reach its ultimate resistance and fail. The formula corresponds to the tensile strength of the bolt. In this case, prying forces are not observed.

$$F_{T,3,Rd} = \sum B_{T,Rd} \tag{2.4}$$

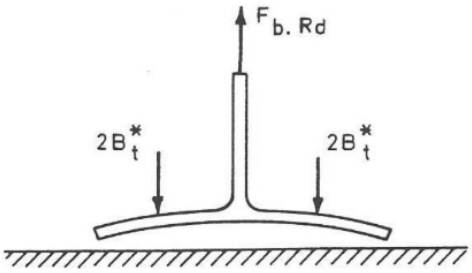

Figure 2.10: Mode of failure 3 [**3**]

Finally, to determine the actual force that the T-stub can support, the minimum value between the three determined forces is used to identify the type of failure and the maximum load the joint can withstand.

$$F_{T,Rd} = min(F_{T,1,Rd}; F_{T,2,Rd}; F_{T,3,Rd}) \tag{2.5}$$

The actual failure mode corresponds to the mechanism with the lowest plastic resistance. In all cases, Eurocode 3 assumes that the bolts are subjected to axial tension, without accounting for bending effects.

To visualize the transition between those failure modes, a graph can be used. In this way, one can directly assess the plastic resistance as a function of the T-stub flange thickness. It is important to note that this representation is only valid under the condition that flange thickness is the only varying parameter, while all other variables remain constant.

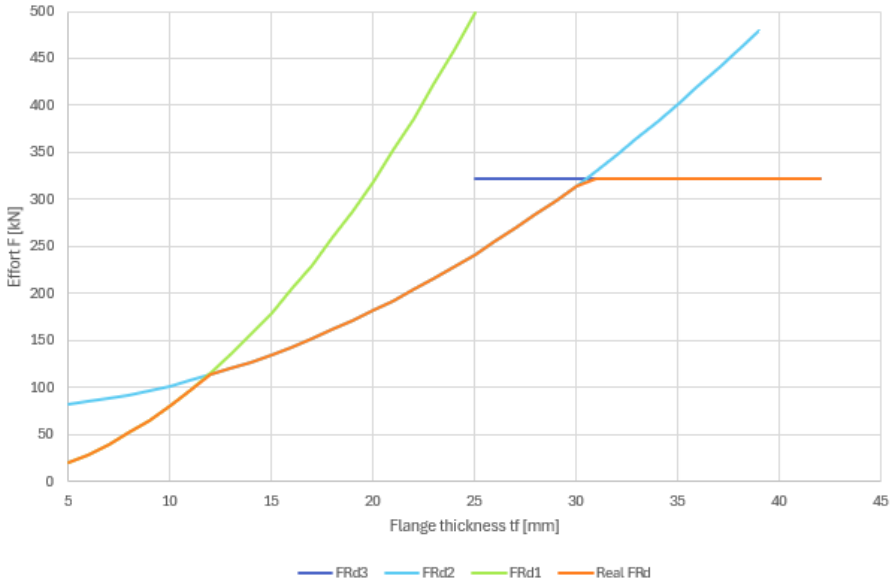

Figure 2.11: The plastic resistance according to the flange thickness

An alternative case, addressed within the Eurocode 3, considers a specific configuration in which no prying forces are developed. For this scenario, the resistance is determined using the following expression:

$$F_{T,0,Rd} = \frac{2 \cdot M_{pl,1,Rd}}{m} = \frac{2 \cdot L_{eff,1} \cdot m_{pl}}{m} \tag{2.6}$$

In this thesis, this specific case is referred to as Failure Mode 0.

2.2.2 The effective length

Another important point to consider in those formula to determine the resistance of the difference mode is the *effective length*. Indeed, $M_{pl,Rd} = m_{pl} \cdot L_{eff}$.

The *effective length* corresponds to an idealised length that contributes to the resistance of the T-stub. It is the length that minimises the energy. It also depends on the number of bolts and whether the bolts act as a group or individually.

Some source have identified three main possible effective lengths : a circular one, a straight line and a trapeze developed by Zoetemijer **[6]**.

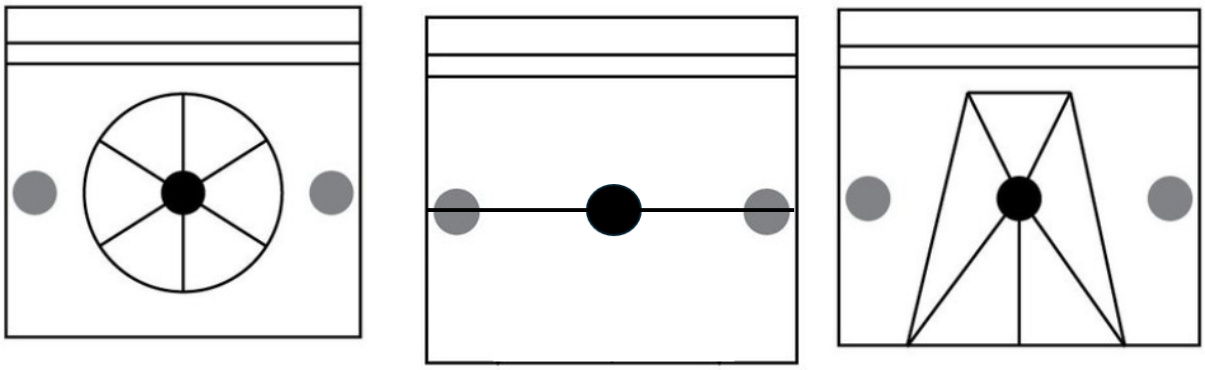

(a) Circular pattern : $L_{eff,c} = 2 \cdot \pi \cdot m$

(b) Straight lines : $L_{eff,nc,1} = L$

(c) Non-circular pattern : $L_{eff,nc,2} = 4 \cdot m + 1,25 \cdot n$

Figure 2.12: Main possibilities of the effective length

These three basic patterns are used in the Eurocode 3 [**4**]. Other line yield patterns have since been studied, such as in the thesis of A. Warnant [**1**], which considered the yield pattern as a straight line along the bolt's axis, with a semi-circle around the bolt's head.

A. Neutelers [**2**] developed another yield pattern based on the previous one. The main difference is the location of the straight line relative to the bolt's axis.

In any case, the real effective length is the minimum length among all possible yield line patterns.

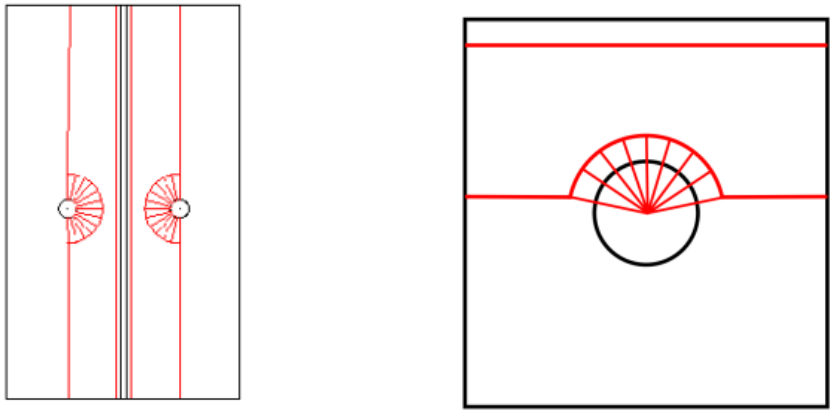

(a) $L_{eff,c,Warnant}$ [**1**] (b) $L_{eff,c,Neutelers}$ [**2**]

Figure 2.13: Other possibilities of the effective length

$$L_{eff,c,Warnant} = \frac{L + L - 2 \cdot m + \pi \cdot m}{2} \tag{2.7}$$

$$L_{eff,c,Neutelers} = L - 2 \cdot \sqrt{\frac{d_w^2}{4} - \delta_{H2}^2} + \frac{d_w}{2} \cdot (\pi - 2 \cdot arcsin(\frac{\delta_{H2}^2}{\frac{d_w}{2}})) \tag{2.8}$$

In this formula, δ_{H2} is the distance between the bolt's axis and the axis of the yield line.

With all this information, it is possible to determine *the effective length* of both mode 1 and mode 2. According to the definition of the mode 2, which presents only one hinge, the second mode is not able to follow a circular yielding pattern.

$$L_{eff,1} = min(L_{eff,c}; L_{eff,nc,1}; L_{eff,nc,2}; L_{eff,nc,Warnant}; L_{eff,nc,Neutelers}) \tag{2.9}$$

$$L_{eff,2} = min(L_{eff,nc,1}; L_{eff,nc,2}) \tag{2.10}$$

A T-stub can be classified as short or long. *A short T-stub is a T-stub whose effective length is equal to its physical length.*

2.3 Existing models for characterization

At this stage, several models have been elaborated to estimate *the ultimate or plastic force* of a T-stub. The simplest and most widely known is the method outlined in the Eurocode 3.

This thesis compares the results from experimental data with the Eurocode model and three other improved models : Zhao model, Neutelers model and Struik and De Back model.

An important parameter of the behaviour curve is the plastic resistance, which represents the force at the limit of the elastic domain. This value has multiple definitions depending on the research context. To determine the plastic limit from a graph, two main approaches exist. The first one is *the intersection* force, which corresponds to the point where the slope of the plastic domain intersects the

y-axis (Figure 2.14a). The second method involves determining the force at the point where *the slope of the plastic domain intersects with the slope of the elastic domain* (Figure 2.14b). These two values are quite close to each other.

In all cases, the plastic resistance is often an approximation.

In this thesis, *the second method*, involving the intersection of the two slopes, has been chosen.

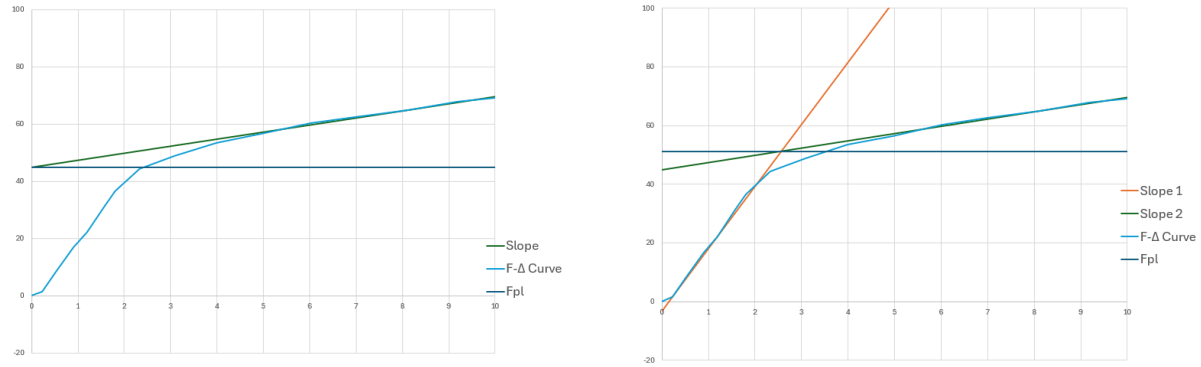

(a) First option (b) **Second option**

Figure 2.14: Options to define the plastique force

2.3.1 Eurocode 3

The Eurocode 3 [**4**] idealises the T-stub as a conventional beam system.

As outlined in the previous section, two analytical approaches are available for determining the resistance associated with failure mode 1. In this thesis, *the second method* (thinking by professor Jaspart) is adopted. According to this approach, the bolt force is assumed to be *uniformly distributed*, and *the prying force* is considered to act at the edge of the flange.

Based on these assumptions, the Eurocode 3 prescribes the following parameters: $e_w = \frac{d_w}{4}$ and $n = min(e; 1,25 \cdot m)$, where m denotes the distance between the two plastic hinges characteristic of failure mode 1. Since the exact location of the hinge adjacent to the weld is generally unknown, the Eurocode 3 assumes its position to be at a distance of $0,8 \cdot h_f$ from the web.

In the Eurocode 3, the following equilibrium is considered.

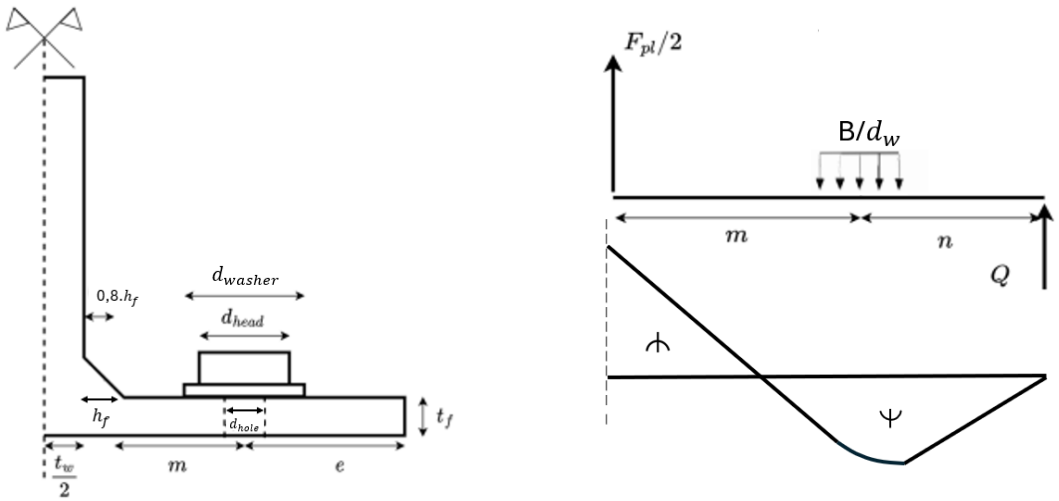

(a) Geometry of a half T-stub (b) Beam model

Figure 2.15: Modelisation of the two methods of the Eurocode 3 [**4**]

The T-stub is analysed as a *one-dimensional beam structure*. This simplified 1D model means that certain effects are not taken into consideration, such as the interaction between the momentum and the shear force (MV interaction), 3D effects, and geometric non-linearities.

This model allows, for the development of the various equilibrium and energy balances, to derive the difference formula from (2.2) to (2.5). Only the three main methods for defining the effective length are defined and used in the Eurocode 3 (Figure 2.12).

Geometry is required, as well as the constitutive laws for both the bolt and the plate.

The two constitutive laws can be obtained through experimental testing, and certain data are essential. These data can be derived from the graph. The idealization of the material's constitutive laws is shown in Figure 2.16. Moreover, the Eurocode 3 adopts a constitutive law based on engineering stress-strain data.

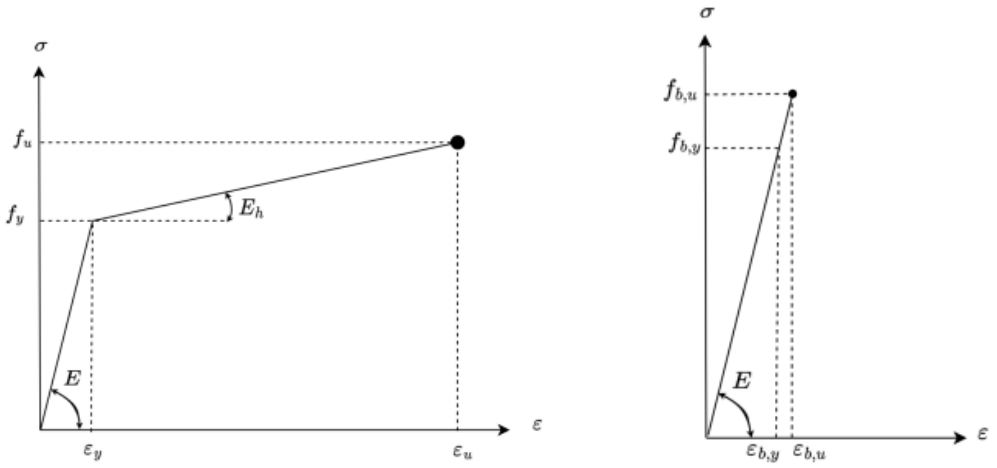

(a) Constitutive law of a plate (b) Constitutive law of a bolt

Figure 2.16: Example of constitutive laws used in the Eurocode model **[2]**

According to the principle of *the component method*, *effective stiffness* is calculated based on the different *stiffnesses of the active components*. In the case of a T-stub fixed to a rigid base, the stiffnesses considered are those of the flange and the bolts.

So, the initial stiffness is calculated as :

$$K_{ini} = \frac{1}{\sum_i \frac{1}{k_i}} \tag{2.11}$$

With k_i is representing the stiffness of each active element to be considered.

The objective of this method is to determine *the displacement-force relationship*. Using the resistance and stiffness of the T-stub, it is possible to construct a bilinear or trilinear curve.

The trilinear curve allows the identification of the transition between the elastic and plastic domains by taking an intermediate stiffness equals to one-third of the initial stiffness. It is important to note that the Eurocode 3 does not incorporate information on the ultimate behaviour, limiting accuracy in the prediction of ultimate failure.

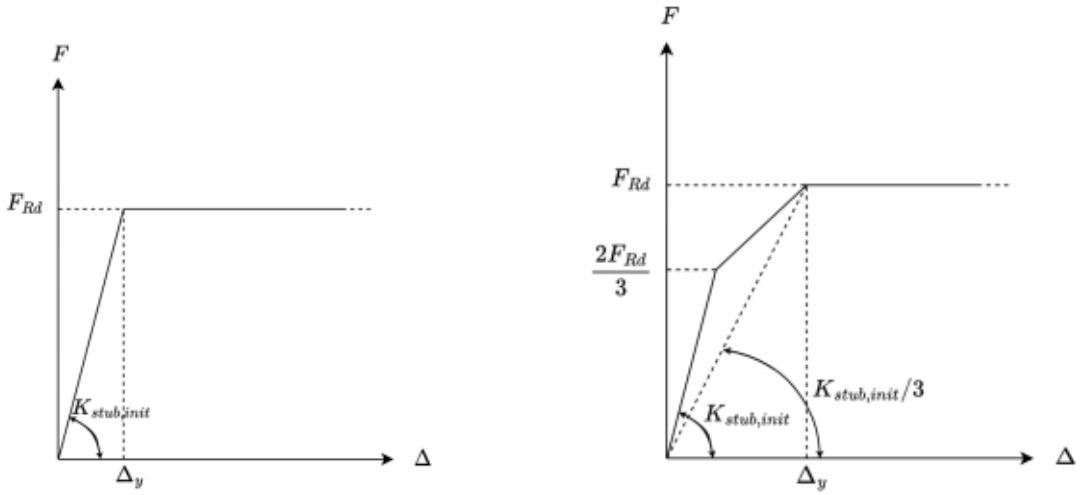

(a) The bilinear curve (b) The trilinear curve

Figure 2.17: The Δ-F curve [**2**]

This model is the most widely recognized, as it is presented in the Eurocode 3. However, no information is provided regarding the ultimate displacement or ultimate strength.

2.4 Improved models for characterization

2.4.1 Zhao model

The Zhao model [**7**] is an improvement of the Piluso model ([**8**] and [**9**]) and includes the results from Jaspart's thesis. In this case, the T-stub is no longer treated as a beam model but is studied as *an assembly of a plate and bolts*, in 2D.

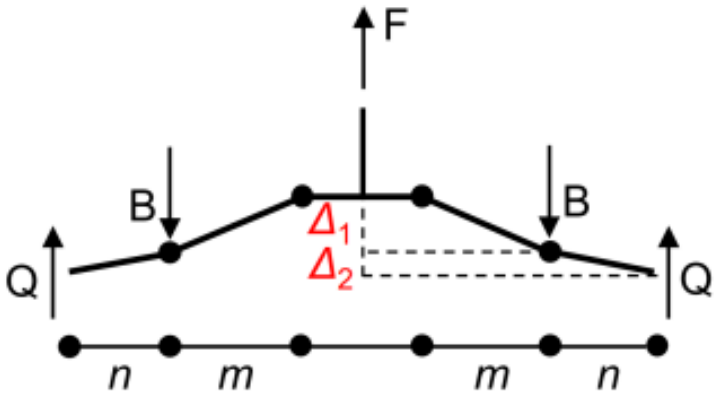

Figure 2.18: The Zhao model [**7**]

Several improvements have been implemented, including ensuring *the compatibility of displacements* between the flange and the bolt, employing more accurate constitutive laws, and approximating geometric non-linearities. However, the interaction of the MV and 3D effects may still not be fully accounted for, and the bolt is considered to be subjected only to tensile forces, *neglecting bending effects*.

The objective of this model is to enhance the prediction of handling after the yielding point. To achieve this, the constitutive laws are refined using *the true stress-true strain curve*. This curve is based on the engineering stress-strain curve and reflects better the real evolution of the material taking into

account the area variation. To construct this new true constitutive law, the equations below are used for each point on the curve.

$$\epsilon_{true} = ln(1 + \epsilon_{eng}) \tag{2.12}$$

$$\sigma_{true} = \sigma_{eng} \cdot (1 + \epsilon_{eng}) \tag{2.13}$$

The constitutive law of the bolt is also improved, as it takes into account not only two points but three, including the necking of the bolt.

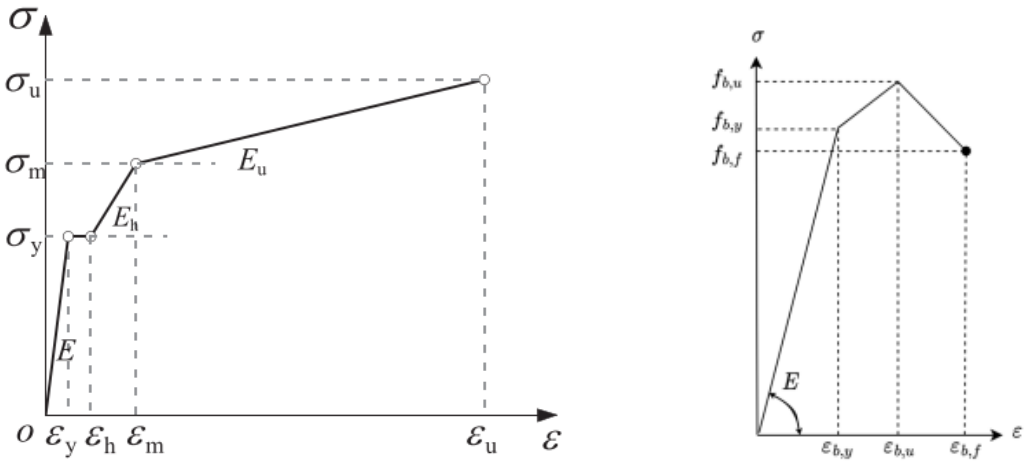

(a) Constitutive law of a plate

(b) Constitutive law of a bolt

Figure 2.19: Example of constitutive law use in Zhao model [**2**]

Moreover, the Zhao model provides a more precise description of the different failure modes. Indeed, it has been observed that the bolt can fail even under mode 1. The Zhao model thus proposes *four types of failure*: mode 2 and mode 3, as explained previously, and mode 1 FF, when the flange is the cause of failure, and mode 1 BR, when the bolt is the cause.

Regarding the displacement, the Zhao model, which considers a combination of bolts and plates, accounts for both the deformation of the plate and the elongation of the bolt. Indeed, to determine the displacement more precisely, the complex constitutive law allows the calculation of a curvature χ for a given moment.

This curvature is essential for evaluating the rotation. And the rotation of the plastic hinges allows to determine the plastic displacement.

Finally, the total displacement is the sum of the plastic displacement and the elastic displacement.

The method constructs two *force-displacement curves*: one for the plate and one for the bolt. Afterward, it is necessary to *combine the two curves manually.* The forces are simply written in increasing order, but particular attention must be given to the displacements to the compatibility of the displacement.

Two examples of curve combinations are shown in Figure 2.20. The first represents a failure where the flange fails. Indeed, the ultimate strength of the bolt is greater than the one of the flange. The second corresponds to a failure driven by the bolt.

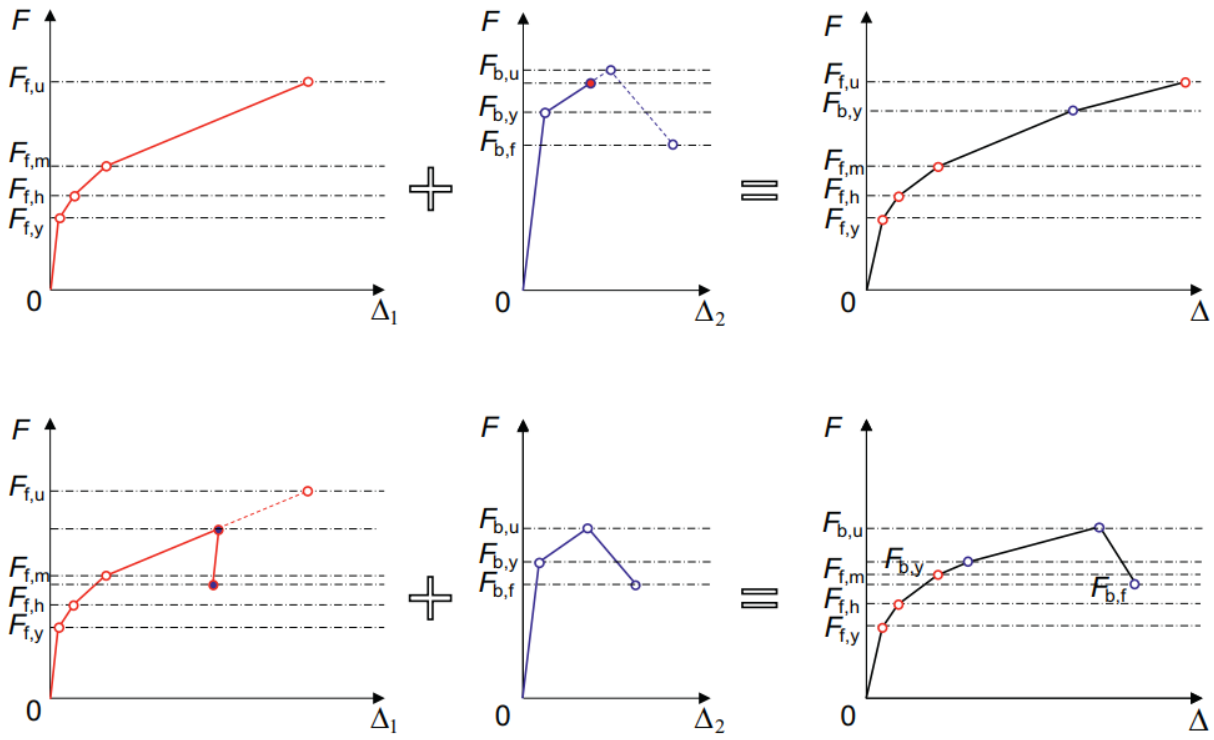

Figure 2.20: The construction of the $\Delta - F$ curve with the Zhao model [**7**]

Just like that, the Zhao model allows the calculation of as many points as desired for the curve. Thus, the curve is quite comprehensive.

2.4.2 Neutelers model

A. Neutelers [**2**] has developed a new model and formula to *determine the plastic resistance* of a T-stub. At this point, the constitutive laws are the same as those used in the Eurocode model, as shown in Figure 2.16.

The modelling is again based on *a beam model*. This model still does not account for 3D effects and assumes that *the bolt is only loaded in tension*. However, in this model, the bolt may apply *a triangular force under the head of the bolt* on the flange.

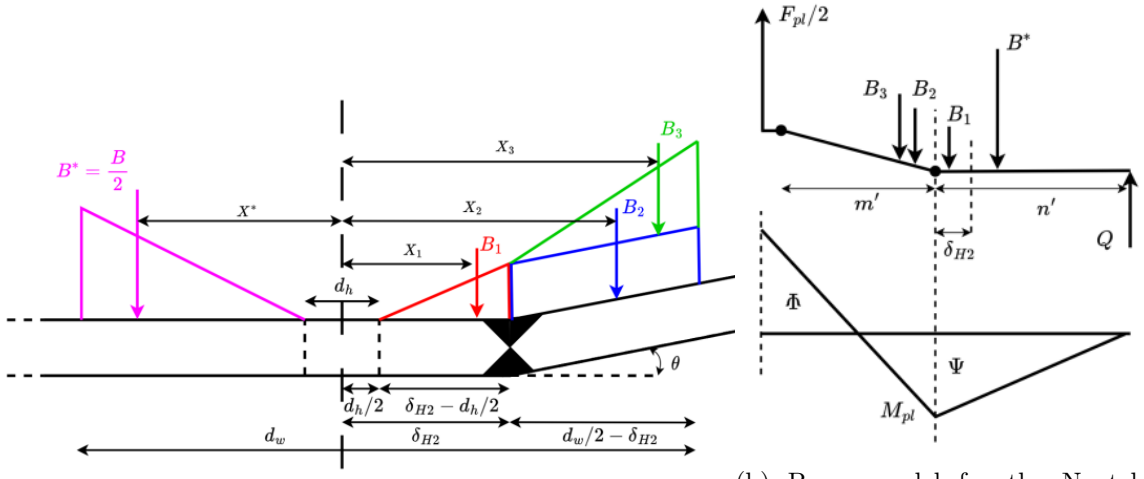

(a) Triangular stress distribution

(b) Beam model for the Neutelers's model

Figure 2.21: Modelisation of the Neutelers's method [**2**]

Compared to other models, *the position of the hinge* has been determined more precisely through a large number of tests. A relationship has been established between the plate-to-bolt stiffness ratio and the location of the plastic hinges. This position of the hinge close to the bolt is located beneath the bolt head but is not aligned with the axis of the bolt.

Once the correct position of the hinge has been determined, *the T-stub is classified*, allowing for *the effective length* to be calculated for a given moment. This classification is based on a criterion involving the ratio of the bending stiffness of the plate to the axial stiffness of the bolt. If this ratio is greater than *the empirical limit 90 mm²*, the T-stub is considered to be *rigid*; if it is smaller, the T-stub is considered *flexible*.

If this ratio exceeds 90 mm², the rigid T-stub exhibits *a two-line mechanism*. In contrast, a flexible T-stub demonstrates *a hybrid mechanism*. Then, the formula for calculating the plastic strength can be applied.

$$F_{pl} = \frac{2 \cdot M_{pl} \cdot (2 \cdot G - \zeta \cdot (d_w - 2 \cdot \delta_{H2})^2)}{m' \cdot G + n' \cdot \zeta \cdot (d_w - 2 \cdot \delta_{H2})^2} \tag{2.14}$$

With the parameter :

$$G = (2 \cdot \delta_{H2} - d_h)^2 + (d_w - d_h)^2 \cdot (6 \cdot \delta_{H2} + d_h + 2 \cdot d_w - 12 \cdot n') \tag{2.15}$$

$$\zeta = 2 \cdot \delta_{H2} - 2 \cdot d_h + 2 \cdot d_w \tag{2.16}$$

2.4.3 Struik and De Back model

The Struik and De Back model [**10**] was developed in 1969, marking an early contribution to the study of T-stub elements. Like the Neutelers model, it is primarily employed to calculate the *plastic resistance*.

As in previous approaches, the Struik and De Back model follows *a beam analogy*, as illustrated in Figure 2.22.

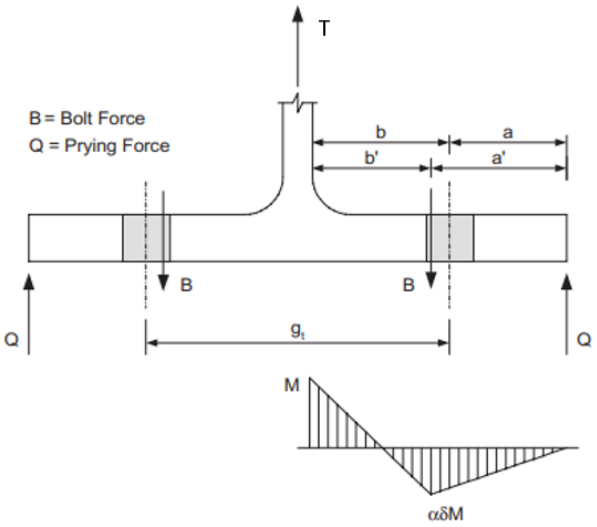

Figure 2.22: The beam model for the Struik and De Back model [**10**]

In this model, the force exerted by the bolt is considered as *a concentrated load, applied at the inner edge of the bolt hole*. The *b* parameter represents the distance between the bolt axis and the midpoint of the weld toe. Like in previous models, *the prying force* is assumed to act at the outer edge of the T-stub flange.

Three different equilibrium conditions can be developed to evaluate the plastic resistance, T, of the T-stub.

- **1. First Equilibrium**: The moment equilibrium between the face of the web and the axis of the bolt.
- **2. Second Equilibrium**: This moment equilibrium is evaluated at the exterior of the bolt axis.
- **3. Third Equilibrium**: This condition involves the force equilibrium of the entire flange.

These equilibrium equations can be expressed as:

$$T \cdot b' = M \cdot [1 + (\alpha + \delta)] \tag{2.17}$$

$$Q \cdot a' = \alpha \cdot \delta \cdot M \tag{2.18}$$

$$B = T + Q \tag{2.19}$$

At the failure, the momentum leads to the plastic moment of the flange : $M_p = \frac{f_y \cdot p \cdot t_f^2}{4}$

Using this plastic moment and the equilibrium conditions, the plastic resistance T can be determined through *three distinct methods* corresponding to the different equilibrium cases. The actual plastic resistance of the T-stub is then taken as *the minimum value* among these three, ensuring a conservative estimation of its load-carrying capacity.

$$T = \frac{(1+\delta)}{2 \cdot b'} \cdot p \cdot f_y \cdot t_f^2 \tag{2.20}$$

$$T = \frac{2 \cdot B \cdot a'}{a' + b'} + \frac{p \cdot f_y \cdot t_f^2}{2 \cdot (a' + b')} \tag{2.21}$$

$$T = 2 \cdot B \tag{2.22}$$

Some similarities can be observed between the formula for this three equilibrium and for the three failure mode for each mode developed in the Eurocode model (equation (2.1), (2.3) and (2.4))

2.5 Summary of the different models

This section presents a comparative analysis of various structural models. The reference model, as defined in the Eurocode 3, is evaluated alongside three alternative models proposed in the literature.

The Eurocode model, the Neutelers model and the Struik and De Back model are all based on beam system. In contrast, the Zhao model adopts a hybrid approach, representing the system as a combination of plates and bolts assembly.

The primary distinction among these models lies in the assumed distribution of stress under the bolt head. The Eurocode's first approach considers *a concentrated load applied along the bolt axis* such as Zhao model, whereas the Struik and De Back model applies *the concentrated load at the inner edge of the bolt hole.* In its second approach, the Eurocode 3 assumes *an uniformly distributed load* beneath the bolt washer. Meanwhile, the Neutelers model introduces an enhanced approach by assuming a *triangularly distributed load.*

Beyond the methodological differences, it should be noted that the Neutelers and Struik and De Back models are exclusively used to determine *the plastic resistance*. In contrast, the Eurocode model allows for the evaluation of *a bilinear or trilinear force–displacement* ($\Delta - F$) response. The Zhao model further refines this analysis by enabling *the computation of multiple points* along the $\Delta - F$ curve up to structural failure.

Given these characteristics, only the Zhao model is capable of capturing *the membrane effect* in the system's response.

Model	Type	Load distribution	$\Delta - F$ curve	Catenary effect
Eurocode Method 1	Beam model	Concentrated at bolt axis	Bilinear or trilinear	Not modelled
Eurocode Method 2	Beam model	Uniform under washer	Bilinear or trilinear	Not modelled
Neutelers	Beam model	Triangular distribution under washer	Plastic resistance only	Not modelled
Struik and De Back	Beam model	Concentrated at the inner edge of bolt hole	Plastic resistance only	Not modelled
Zhao	Plates + bolts model	Concentrated at bolt axis	Up to failure	Modelled

Chapter 3

Experimental studies

3.1 Existing experimental studies

To advance this thesis and validate our numerical model, several experimental studies are analysed in this chapter. A comparison is conducted to determine which one of this study is the most appropriate to use in the thesis. Each essay study examined to ensure that the experimental conditions are similar to those required, and that all necessary data are available.

3.1.1 Tartaglia

This first campaign aims to compare multiple specimens with variations in certain parameters, subjected to high deformation and assembled using preloaded bolts. In every case, the T-stub is fixed on a rigid base.

It compares HR and HV bolts. The thickness of the flange varies in a range between 8 and 20 mm. The article also proposes a comparison of two configurations : *long T-stub and short T-stub*. The dimensions are shown on the Figure 3.1

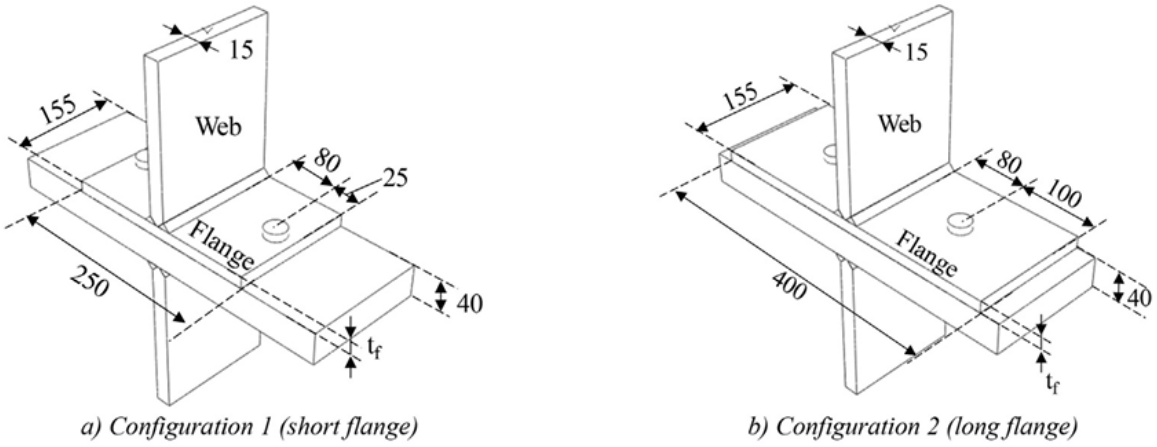

Figure 3.1: Two configurations for the campaign led by Tartaglia [**11**]

Characteristics of each specimen can be distinguished thanks to its name. It starts every time with a T for T-stubs. After you can find L or S to know in which configuration you are (long or short). Then you can find HR or HV according to the type of bolts. Finally, the thickness of the flange is added.

The Table 3.1 presents the characteristics of all the tested specimens. The two highlighted specimens are used specifically in a later section of this thesis (T-S-HR-8 and T-S-HR-20).

Specimen	d_{plate} [mm]	t_w [mm]	t_f [mm]	B [mm]	L [mm]	e [mm]	C [mm]	a_w [mm]	h_f [mm]
T-S-HR-8	40	15	8	250	155	25	80	8,84	12,5
T-S-HR-12	40	15	12	250	155	25	80	8,84	12,5
T-S-HR-15	40	15	15	250	155	25	80	8,84	12,5
T-S-HR-20	40	15	20	250	155	25	80	8,84	12,5
T-L-HR-8	40	15	8	400	155	100	80	8,84	12,5
T-L-HR-12	40	15	12	400	155	100	80	8,84	12,5
T-L-HR-15	40	15	15	400	155	100	80	8,84	12,5
T-L-HR-20	40	15	20	400	155	100	80	8,84	12,5
T-S-HV-8	40	15	8	250	155	25	80	8,84	12,5
T-S-HV-12	40	15	12	250	155	25	80	8,84	12,5
T-S-HV-15	40	15	15	250	155	25	80	8,84	12,5
T-S-HV-20	40	15	20	250	155	25	80	8,84	12,5
T-L-HV-8	40	15	8	400	155	100	80	8,84	12,5
T-L-HV-12	40	15	12	400	155	100	80	8,84	12,5
T-L-HV-15	40	15	15	400	155	100	80	8,84	12,5
T-L-HV-20	40	15	20	400	155	100	80	8,84	12,5

Table 3.1: All the specimens of the Tartaglia experimental study

The article also communicates the results of the mechanical features of the investigated materials. The Young's modulus, the yielding stress, the ultimate stress and the ultimate deformation are given in a table. This information is available for each thickness and for the two types of bolt. The results are in the Table 3.2.

Specimen	Coupon thickness/Bolt diameter [mm]	Young's modulus E [MPa]	Yielding stress f_y [MPa]	Ultimate stress f_u [MPa]	Ultimate deformation ϵ_u [-]
Flange 8	8	208 247	369	858	0,28
Flange 10	10	209 855	455	1045	0,275
Flange 12	12	213 105	396	919	0,287
Flange 15	15	210 085	409	945	0,27
Flange 20	20	208 755	390	1 007	0,283
HR bolt	16	143 024	1 001	1 143	0,046
HV bolt	16	141 388	1 140	1 249	0,044

Table 3.2: Mechanical features of different materials for the Tartaglia experimental study

Once all this information was established, the test was conducted using the setup shown in Figure 3.2. The experiment was performed under a controlled displacement protocol, gradually increasing the displacement until the failure of the specimen was observed.

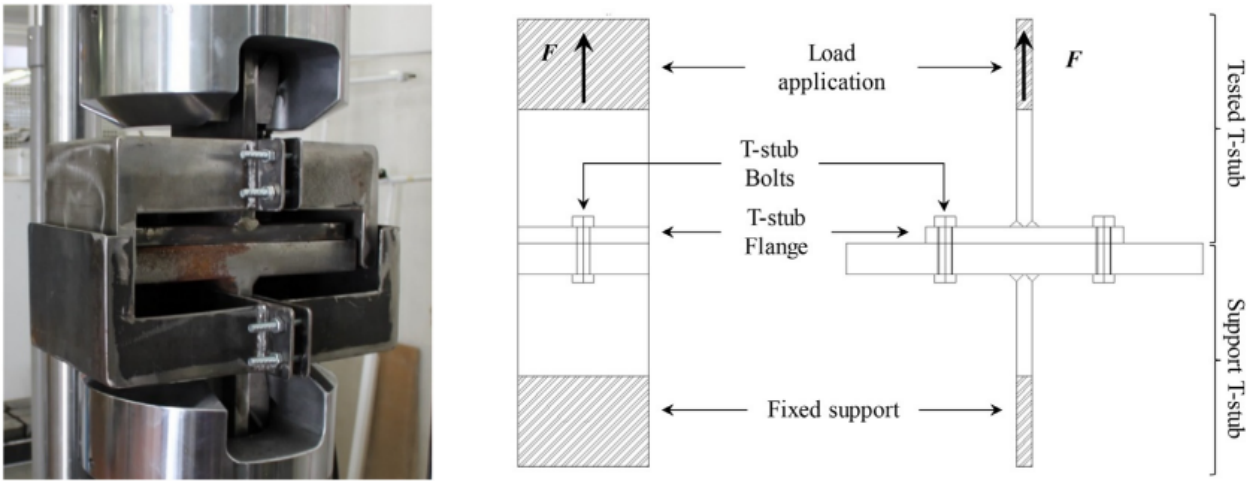

Figure 3.2: The setup for the Tartaglia study experimental [**11**]

3.1.2 Bezerra

This second campaign investigated T-stubs bolted to rigid bases. The study primarily focused on four aspects: the relationship between the applied load and slip displacement, the contact pressure between the T-stub flange and the rigid base, the effect of prying action on the bolts, and bolt failure mechanisms. To conduct this study, three different series of tests were performed, each consisting of three specimens. The main difference between the series is the flange thickness. The specimens were fixed to the rigid base using two bolts with a diameter of 14 mm.

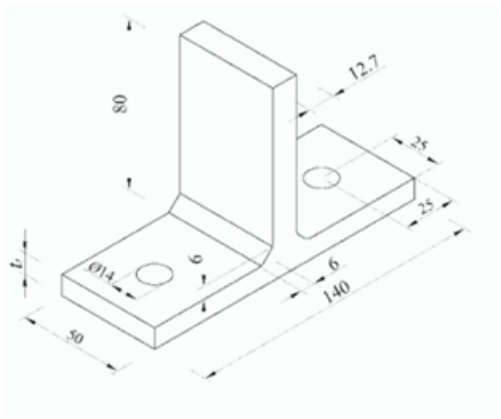

(a) The geometry of the Bezerra study

(b) The specimen P1D after test

Specimen	d_{plate} [mm] (estimated)	t_w [mm]	t_f [mm]	B [mm]	L [mm]	e [mm]	C [mm]	a_w [mm]	h_f [mm]	Number of bolts
P1D	109,5	12,7	4,8	140	50	25	36,65	5,3	6	2
P2D	106,4	12,7	7,9	140	50	25	36,65	5,3	6	2
P3D	101,6	12,7	12,7	140	50	25	36,65	5,3	6	2

Table 3.3: All the specimens of the Bezerra experimental study [**12**]

3.1.3 Faralli

In this study, the objective is to investigate *the second-order effects*. To achieve this, several T-stubs with variations in their geometry are tested. These T-stubs are fixed to a rigid base with additional stiffeners.

The geometry of the T-stub is quite standard, and all the relevant measurements are provided in Figure 3.4. For this campaign, the steel used is S275, which has been characterized through testing to obtain the material's constitutive law and the complete stress-strain curve (σ - ϵ). The bolts employed are of grade 10.9. All the specimens are listed in Table 3.4

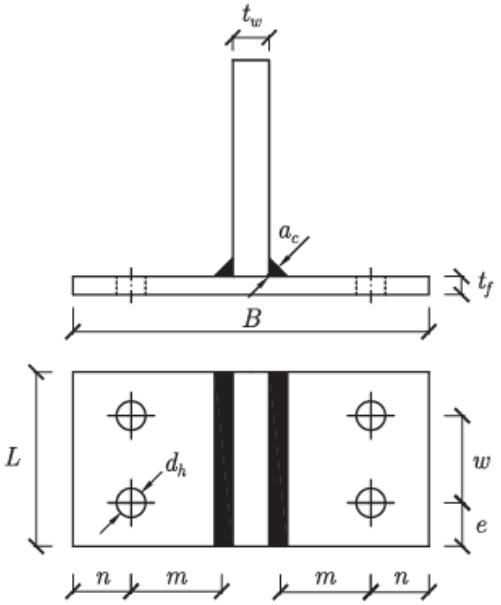

Figure 3.4: The geometry of the Faralli study [**13**]

Specimen	t_f [mm]	t_w [mm]	a_c [mm]	n [mm]	m [mm]	B [mm]	L [mm]	w [mm]	d_h [mm]	d_{plate} [mm]
M16-3-10	10,1	19,6	7,1	31,9	47,2	196	96	48	17,8	25
M16-5-10	10,15	19,7	7,1	31,8	77,7	260	96	48	18,3	25
M16-5-15	15,2	19,8	7,1	31,5	77,1	260	96	48	17,7	25
M18-3-10	10,2	19,6	7,1	36,1	51,6	216	108	54	20,1	25
M18-5-10	10,2	19,7	7,1	34,3	90,3	288	108	54	19,5	25
M18-4-15	15,2	19,9	7,1	36,5	67,1	252	108	54	19,7	25
M18-5-15	15,3	19,7	7,1	37,1	87,6	288	108	54	19,5	25
M20-3-10	9,9	20,4	10	39,2	60,2	242,4	120	60	22	25
M20-5-10	9,9	20,5	10	39,5	92,6	322,4	120	60	22	25
M20-4-15	15,2	20,5	10	39,4	77,5	282,4	120	60	21,8	25
M20-5-15	15,3	20,7	10	40,2	98,4	322,4	120	60	22,9	25
M20-4-20	19,75	20,5	10	39,3	75,2	282,4	120	60	21,9	30
M20-5-20	19,7	20,4	10	39,9	96,4	322,4	120	60	22	30

Table 3.4: The specimens for the Faralli's campaing [**13**]

The setup is relatively simple and clear, with no sensor present. In this case, all displacements are provided by the machine. A notable point is that these displacements account for any variation in the machine's own movement. The setup is shown in Figure 3.5.

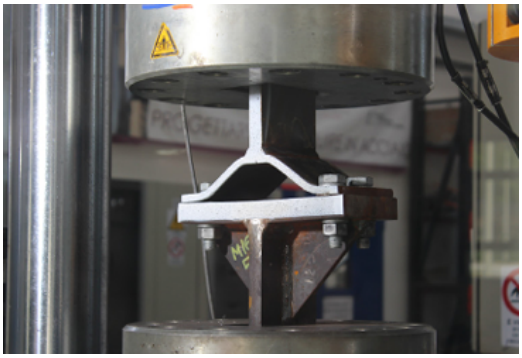

Figure 3.5: The setup of Faralli's campaign [**13**]

Most of the specimens failed according to failure mode 1 characterized by the failure of the flange, or failure mode 2, involving either the failure of the flange or the bolt. All specimens were photographed after testing. Two of these are shown in Figure 3.6. For one specimen, M20-5-15, it can be observed that the base deformed during the test, exhibiting a V-shaped distortion.

(a) M16-5-10

(b) M20-5-15

Figure 3.6: The deformation after the test [**13**]

3.1.4 Khani

This study presents a simple comparison between a coupled T-stub, consisting of two identical T-stubs fixed together, and a T-stub attached to a rigid base. The objective is to analyse their behaviour under a static load with large displacements. Only two specimens have been tested.

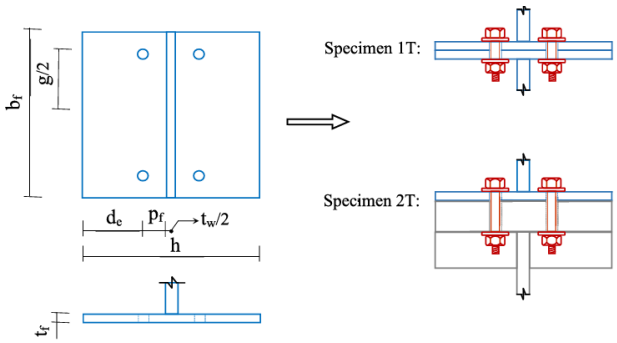

Figure 3.7: The geometry of the specimen for the Khani study [**14**]

Specimen	h [mm]	b_f [mm]	g [mm]	p_f [mm]	t_w [mm]	t_f [mm]	d_e [mm]
1T	300	300	220	40	15	8	102,5
2T	300	300	220	40	15	8	102,5

Table 3.5: The geometry of the different specimens for the study of Khani [**14**]

These tests were conducted using S235 steel and M16 grade 10.9 bolts. The tests were performed under controlled displacement traction. The objective was to obtain and analyse the *force-displacement curve*. Both specimens failed according to failure mode 1. In the coupled T-stub, failure occurred due to the failure of the bolt. In the tied-to-rigid T-stub, failure resulted from punching of the flange as documented in the photographs shown in Figure 3.8.

(a) M16-5-10 (b) M20-5-15

Figure 3.8: The deformation after the test [**14**]

3.1.5 Konya

This campaign aims to test a large number of specimens with variations in their geometry to evaluate differences in the force-displacement response curves and their deformation patterns. The geometry of each specimen is constructed as shown in Figure 3.9a. Other key measurements include t_p, the thickness of the flange, t_w, the thickness of the weld, and d_b, the diameter of the bolt.

The study focuses on specimens with relatively large bolt diameters and thin plates fixed on rigid base. All the parameters specified in the Tables 3.6 are the subjects of the study. Specifically, these include the flange thickness, flange width, the distance between the two rows of bolts, the diameter of the bolt, the distance from the row of bolts to the edge, and the weld thickness.

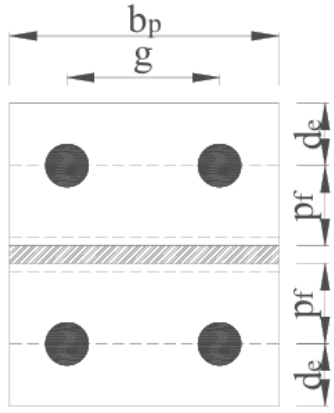

(a) The geometry of the specimen for the Konya study

(b) The deformation of the specimen U11

Figure 3.9: Information about the Konya study [**15**]

Specimen	t_p [mm]	$b_p/2$ [mm]	g/2 [mm]	p_f [mm]	t_w [mm]	d_b [mm]	d_e [mm]
U1	10	120	70	40	10	27	50
U2	8	120	70	40	10	27	50
U3	6	120	70	40	10	27	50
U4	10	120	70	60	10	27	50
U5	8	120	70	60	10	27	50
U6	6	120	70	60	10	27	50
U7	10	120	70	80	10	27	50
U8	8	120	70	80	10	27	50
U9	6	120	70	80	10	27	50
U10	10	120	70	100	10	27	50
U11	8	120	70	100	10	27	50
U12	6	120	70	100	10	27	50
U13	10	120	70	60	10	30	50
U14	8	120	70	60	10	30	50
U15	6	120	70	60	10	30	50
U16	10	120	70	60	10	24	50
U17	8	120	70	60	10	24	50
U18	6	120	70	60	10	24	50
U19	10	120	70	80	10	30	50
U20	8	120	70	80	10	30	50
U21	6	120	70	80	10	30	50
U22	10	120	70	80	10	24	50
U23	8	120	70	80	10	24	50
U24	6	120	70	80	10	24	50
U25	10	120	70	80	20	27	50
U26	8	120	70	80	20	27	50
U27	6	120	70	80	20	27	50
U28	10	120	70	80	30	27	50
U29	8	120	70	80	30	27	50
U30	6	120	70	80	30	27	50
U31	8	120	70	60	10	27	70
U32	8	120	70	60	10	27	90
U33	8	120	70	60	10	27	110
U34	8	120	70	60	10	27	90
U35	8	120	70	60	10	27	90

Table 3.6: The specimens for the study of Konya [**15**]

3.1.6 Summary of the existing studies

A review of the literature reveals that several experimental studies have already been conducted on this topic. In this thesis, only five of these studies are considered. To remain within the scope of this work, all selected studies involve specimens with *a rigid base*. Furthermore, the T-stubs are required to be classified as *short*. Indeed, there is ongoing debate regarding the appropriate method for determining *the effective length*, l_{eff}.

To minimize variability in parameters and avoid controversy surrounding this aspect, it is preferable to restrict the analysis to *short T-stubs*. All selected experimental campaigns are therefore well suited for the objectives of this thesis.

Name	Base	Short/Long	Number of specimen	Material's law
Tartaglia	Rigid	Both	16	Values
Bezerra	Rigid	Short	3	Values
Faralli	Rigid	Short	13	Curve
Khani	Rigid and symmetry	Short	2	Values
Konya	Rigid	Short	35	Values

Table 3.7: Summarry of the existing experimentals studies

3.2 The chosen experimental study

The Tartaglia test campaign has been selected, as it offers optimal experimental conditions. In particular, the analysis focuses on the behaviour of short specimens. This type of T-stub is currently better understood. In addition, the choice of bolt type facilitates the study, with the HR model exhibiting a more consistent behaviour.

To validate the numerical study, specific specimens must be tested. To introduce variability in the structural response, the two specimens selected for numerical analysis are T-S-HR-8 and T-S-HR-20. They are highlighted in the Table 3.1. The difference in flange thickness between these specimens may lead to a change in failure mode.

(a) T-S-HR-8 after test (b) T-S-HR-20 after test

Figure 3.10: Deformation after test of the two principal specimens

3.2.1 Assumptions

Some assumptions are necessary. In fact, the article presenting the test campaigns provides some information, but not all of it. Certain aspects must be defined early in the study to ensure clarity and consistency throughout the numerical analysis.

The material's constitutive law of the T-stub

As previously explained, the article provides specific details regarding the material's constitutive law. However, *no complete stress-strain curve* is shared for the different material depths. All available values are summarized in Table 3.2. At first glance, it is evident that these values do not fully meet expectations and appear incomplete. Since additional information regarding the full curve or the methodology used to obtain the results is unavailable, assumptions have been made to retain the values provided in the article.

For a more comprehensive analysis, the most accurate approach would be to incorporate a damaged plasticity model. However, this step requires additional data to be properly implemented. Consequently, the present thesis is conducted *using an undamaged plasticity model*.

Furthermore, *the plastic plateau length is not specified.* According to Eurocode 3-1-14 [**16**], the Yun-Gardner law provides a formula and a condition for the parameter ϵ_{sh}, which represents the strain at the end of the plastic plateau. This condition requires ϵ_{sh} to be within the range of 0,015 to 0,03. Due to the unusual values of f_u and f_y, this condition is not satisfied. As a simplifying assumption, $\epsilon_{sh} = 0,015$ has been adopted for all thicknesses.

In conclusion, *a trilinear curve is adopted for the material's constitutive law for the steel plate.*

Below are the properties corresponding to two flange thicknesses, as provided in the referenced study. These two cases are then represented on the stress–strain ($\epsilon - \sigma$) diagram to illustrate the material's constitutive law. While these two thicknesses are used as example, the same procedure can be applied to other thickness values.

Specimen	Coupon thickness/Bolt diameter [mm]	Young's modulus E [MPa]	Yielding stress f_y [MPa]	Ultimate stress f_u [MPa]	Ultimate deformation ϵ_u [-]
Flange 8	8	208 247	369	858	0,28
Flange 15	15	210 085	409	945	0,27

Table 3.8: Mechanical features for the Tartaglia experimental study

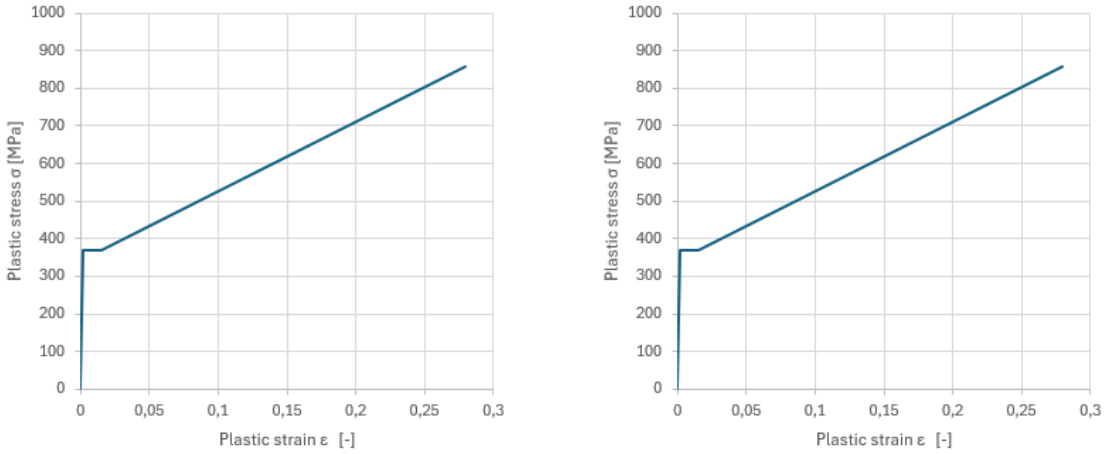

(a) Material's constitutiveslaw for a flange of 8 mm

(b) Material's constitutive law for a flange of 15 mm

Figure 3.11: Examples of material's constitutivs laws with assumptions

The material's constitutive laws here are engineering material's constitutive laws.

Sensor positioning

The article does not specify the exact *positioning of the sensors* used to measure deformation. Ideally, multiple sensors should be placed on both the flange and the web for a more detailed analysis. However, based on the setup image in Figure 3.2, it is not possible to determine the exact locations of the sensors. The only visible possibility suggests that the sensors might be integrated into *the testing machine itself.*

In this case, a particular relevance is the fact that the deformation recorded by the machine includes not only the deformation of the T-stub but also the elongation of both the web and any additional deformations occurring within the machine. While this effect is often neglected, it must be acknowledged for a more accurate interpretation of the results.

3.2.2 Application of the models

All four models (the Eurocode approach and the three improved models) were applicable to the two specimens selected from Tartaglia's study. To maintain clarity and readability throughout this thesis, the complete set of calculations for all four models is provided in Appendix A for the specimen T-S-HR-8. The following section presents the results obtained from the application of these models on the two specimens. Based on the calculations, specimen T-S-HR-8 can be classified as exhibiting failure mode 1, while specimen T-S-HR-20 corresponds to failure mode 2.

T-S-HR-8

The first step consists in evaluating the ability of the models to accurately reflect the experimental behaviour. The Zhao model provides a good estimation of the ultimate displacement but underestimates the ultimate force. Despite this, it closely matches the observed behaviour in both the elastic and plastic phases. However, it does not capture the onset of membrane effects early enough in the deformation process.

In contrast, the force–displacement curve predicted by the Eurocode 3 does not align well with the experimental results. However, in the second and third graphs of the Figure 3.12, it can be observed that the Eurocode 3 correctly estimates the plastic strength, as confirmed in Table 3.9. The relative error is calculated using the actual plastic resistance listed in the first row. The best approximation is highlighted in green.

While most of the other models tend to slightly overestimate the plastic strength, the associated relative error is still within an acceptable range.

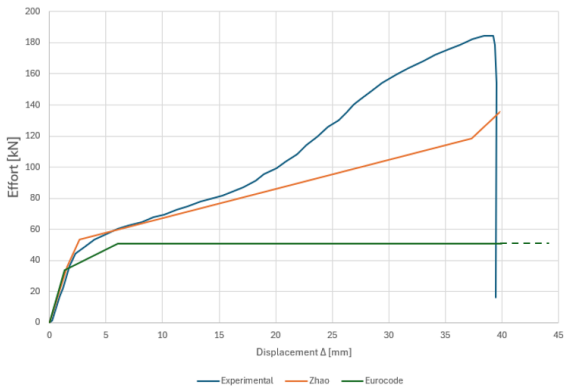

(a) The force-displacement curve with different models

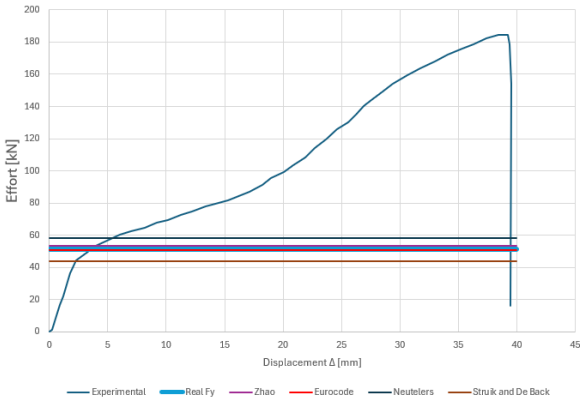

(b) The plastic resistance determine with different models

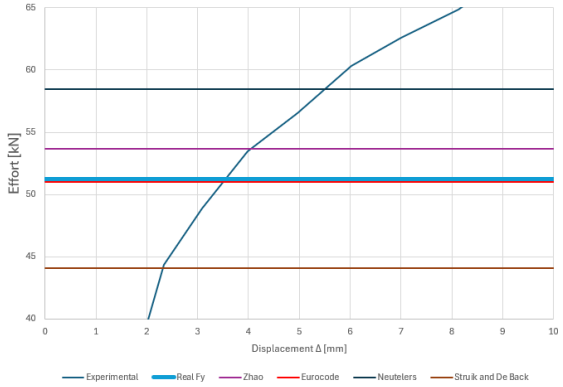

(c) The plastic resistance determine with different models (zoom)

Figure 3.12: Application at the T-stub T-S-HR-8

Model	Mode	F_y [kN]	Relatif error [%]	F_u [kN]	Relatif error [%]
Experimental (real)	1	51,22	-	184,49	-
Zhao	1	53,64	4,7	135,28	-26,67
Eurocode	1	51,01	-0,4	-	-
Neutelers	1	58,47	14,15	-	-
Struik and Deback	1	44,06	-13,97	-	-

Table 3.9: Results for the application of models to the specimen T-S-HR-8

T-S-HR-20

For the second specimen, for which experimental results are available, it can be observed that the Zhao model closely fits the experimental force–displacement curve. Although it provides a better estimation of the ultimate force compared to the first specimen, it fails to accurately predict the ultimate displacement. As expected, the complete force–displacement curve produced by the Eurocode method does not closely reflect the experimental behaviour.

Regarding plastic strength, all the models overestimate the actual value. Among them, the Struik and De Back model exhibits the greatest deviation from the experimental result.

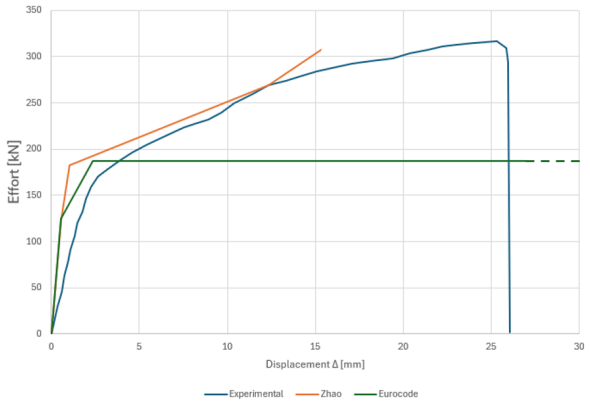

(a) The force-displacement curve with different models

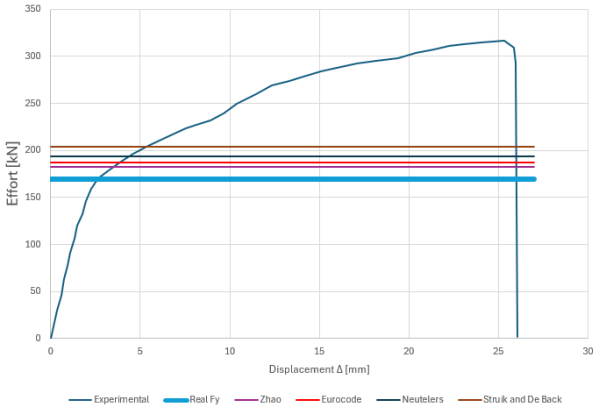

(b) The plastic resistance determine with different models

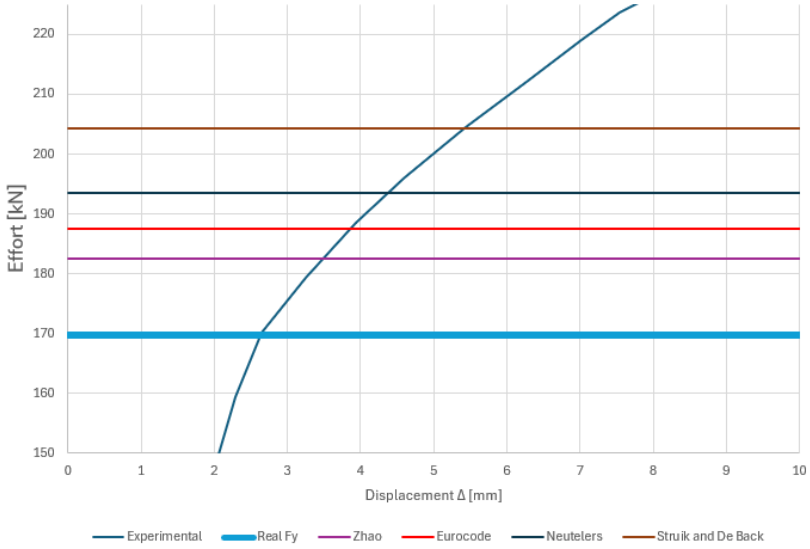

(c) The plastic resistance determine with different models (zoom)

Figure 3.13: Application at the T-stub T-S-HR-20

Model	Mode	F_y [kN]	Relatif error [%]	F_u [kN]	Relatif error [kN]
Experimental (real)	2	169,74	-	316,85	-
Zhao	2	182,5	7,5	307,68	-2,9
Eurocode	2	187,5	10,4	-	-
Neutelers	2	193,5	13,99	-	-
Struik and Deback	2	204,38	20,4	-	-

Table 3.10: Results for the application of models to the specimen T-S-HR-20

Chapter 4

Numerical modelling

Based on the findings discussed in the previous chapter, several studies have investigated the behaviour of T-stubs either fixed to a rigid base or configured as coupled systems. To advance the understanding of alternative T-stub joint configurations, a comprehensive parametric analysis is required. In the present study, such an analysis is conducted using *the non-linear finite element software Abaqus* using an Abaqus's tutorial [**17**] developed by A.Neutelers.

To set up the simulation, a displacement is imposed at the top of the web. For validation, this displacement corresponds to the ultimate displacement observed in the experimental study's graph. Subsequently, the displacement is fixed at 40 mm for the parametric analysis.

As an initial step, it is essential *to validate the numerical model* to ensure that the software yields results that are representative of real physical behaviour. For this purpose, the two specimens from the selected experimental study is simulated on Abaqus. The numerical outcomes are then compared against the experimental force–displacement curves to assess the accuracy and reliability of the model.

4.1 Modelling

To accurately reproduce the specimen in Abaqus, each component of the joint must be modelled individually prior to assembly. The specimen consists of three distinct parts: the base plate, the bolt, and the T-stub. For each component, both *the geometric definition and the corresponding material constitutive laws* are required. Once the model is constructed, further verification steps are necessary to ensure that the numerical results obtained from the Abaqus simulation closely correspond to the experimental data.

To maintain consistency throughout the modelling process, *a uniform system of units* is adopted and applied consistently within the Abaqus environment.

- Length : mm
- Force : N
- Mass : $10^3 kg$
- Stress : MPa
- Density : $10^3 kg/mm^3$

4.1.1 Modelling of the base

The base constitutes the initial component to be modelled. In the preliminary stage of the analysis, it is approximated as *a rectangular parallelepiped*. The experimental study provides limited geometric data, specifying only the depth and width of the base. As illustrated in Figure 3.1, the depth is 40 mm, while the width corresponds to that of the T-stub, which is 155 mm. This approximation is adopted in the first stage of the modelling process. Furthermore, since the total length of the base is

not explicitly provided, it is assumed to exceed the one of the T-stub. Therefore, a nominal length of 500 mm is adopted for modelling purposes.

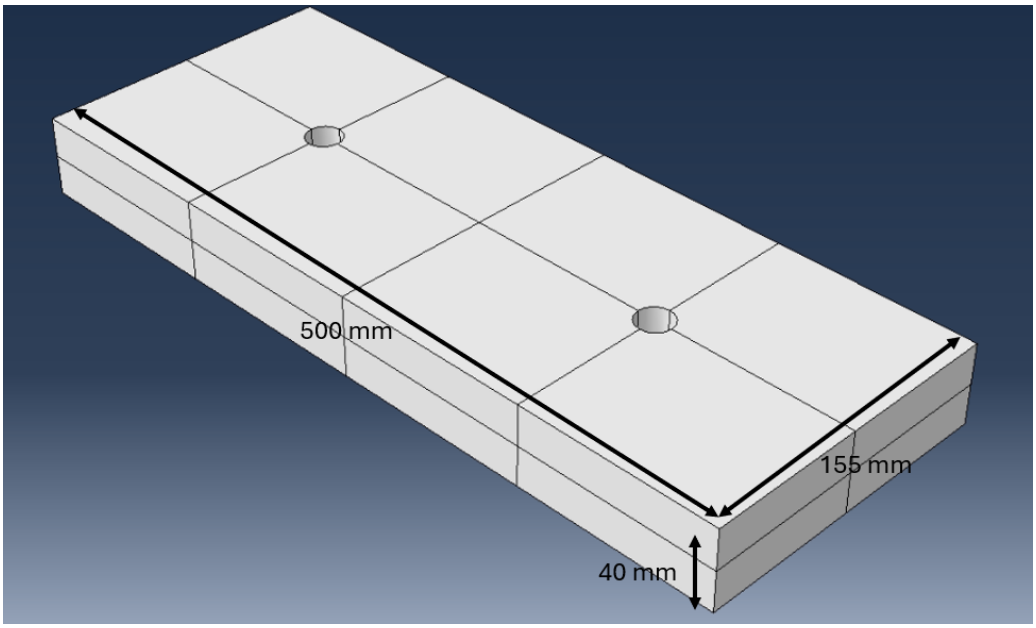

Figure 4.1: Modelling of the base for the experimental essay T-S-HR-8

The objective is to ensure that *the base behaves as a perfectly rigid body.* To guarantee such mechanical behaviour, assumptions regarding the material constitutive law must be defined. At a minimum, two material parameters are required: the Young's modulus (E) and the yield stress (f_y). In this context, both values are chosen to be five times greater than those of the T-stub material. Accordingly, the Young's modulus for the base is set to $E = 1000000MPa$ and the yield strength is taken as $f_y = 2000MPa$. As for the boundary conditions, the base is fully fixed along its lower edges to simulate rigid support.

For the parametric study, the base is modelled with the actual geometry of a T-stub of identical length and width of the T-stub rather than as a rectangular parallelepiped. The material constitutive law used for the base is the same as that applied to the T-stub, corresponding to S355 steel.

4.1.2 Modelling of the bolt

The second component to be modelled is the bolt, which is identical on both sides. *The simplest approach* to represent the bolt is by modelling it as a revolution of rectangular volumes. The dimensions of these rectangular elements vary depending on the combined depths of the base and the T-stub. In the current experimental setup, M16 bolts are employed. Therefore, the geometric characteristics of the bolts can be obtained from standardized technical catalogs[**18**].

The material's constitutive law for the bolt is bilinear and given by the study.

Specimen	Coupon thickness/Bolt diameter [mm]	Young's modulus E [MPa]	Yielding stress f_y [MPa]	Ultimate stress f_u [MPa]	Ultimate deformation ϵ_u [-]
HR bolt	16	143 024	1 001	1143	0,046

Table 4.1: Mechanical features of the bolt for the Tartaglia experimental study

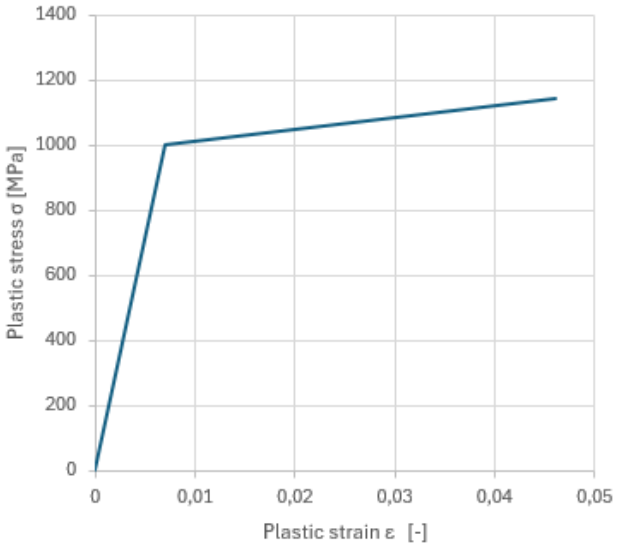

Figure 4.2: Material's constitutive law for the Bolt M16 in the Tartaglia's study

The bolt can be modelled with another method that is closer to the reality. Indeed with this configuration, it considered that there isn't any displacement between the barrel of the bolt and the interior diameter of the washer. With the previous modelling, it's also considered that the resistance of the bolt is the same on every part of the bolt.

The Figure 4.3 illustrates the difference between *the previous and the updated modelling approach*. In the improved configuration, a relative displacement is observed between the barrel and the washer. However, no significant displacement is detected between the washer and the bolt head. This suggests the presence of a substantial frictional force at the interface between the bolt head and the washer.

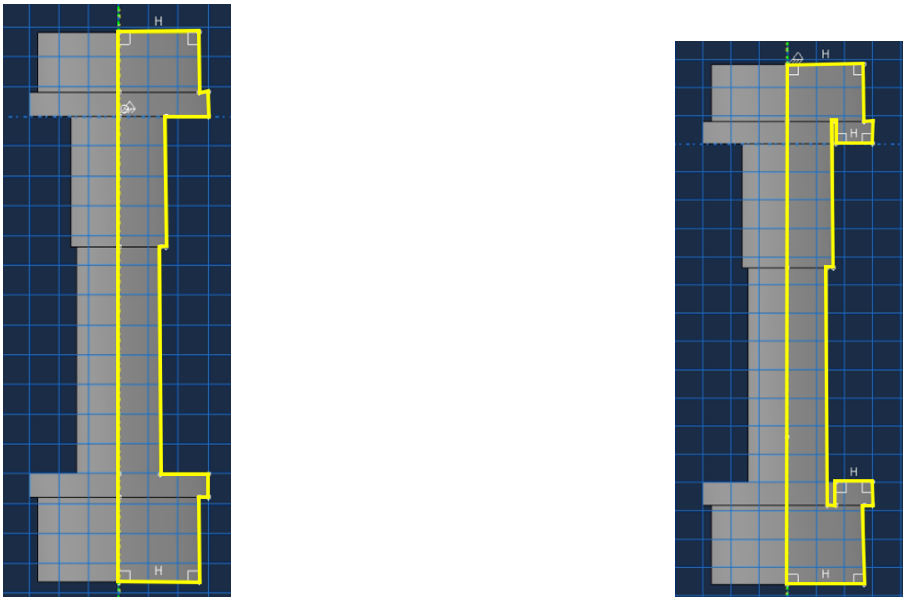

(a) Modelling of the bolt with the original model (b) Modelling of the bolt with the improved model

Figure 4.3: The two possibilities to model the bolt

To further enhance this new modelling approach, a new formula has been developed by A.Neutelers to determine an equivalent Young's modulus for the barrel. The proposed formula is as follows:

$$E_{eq} = \frac{K_b \cdot L_b}{A_s \cdot \frac{L_s}{L_b} + A_{st} \cdot \frac{L_{st}}{L_b}} \tag{4.1}$$

The subscript "s" refers to the characteristics of the barrel without threading, while "st" denotes the threaded barrel configuration. The parameter L_b represents the total length of the barrel. The final parameter, K_b, is an empirical coefficient expressed in N/mm, derived from a series of experimental tests performed on M16 bolt configurations. It should be noted that the commonly adopted value of $K_b = 300\,000 Nmm$ remains an approximation.

It should be noted that while this method enhances the modelling accuracy by better approximating real behaviour, the proposed formula remains an approximation.

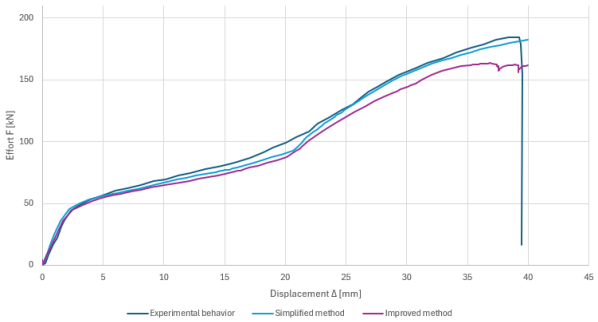

(a) Modelling of the bolt with the improved method and the original method for the T-stub T-S-HR-8

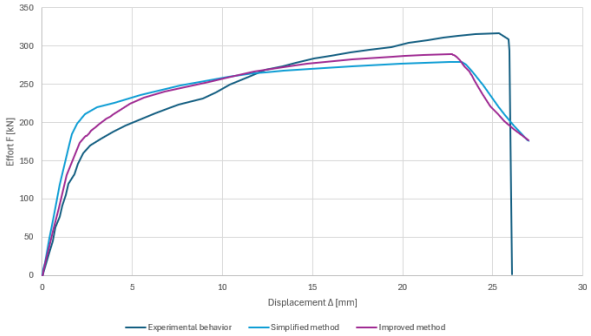

(b) Modelling of the bolt with the improved method and the original method for the T-stub T-S-HR-20

Figure 4.4: Comparison of the 2 methods

4.1.3 Modelling of the T-stub

The T-stub is modelled according to the geometrical characteristics shown in Figure 3.1. The first two specimens selected for the validation phase are highlighted in the Table 3.1. The modelling process follows a logical sequence, and the component is subdivided into sections to generate a regular mesh. The material behaviour is defined using a specific material's constitutive law, based on the assumptions detailed in Section 3.2.1 and example are shown on the graph 3.11

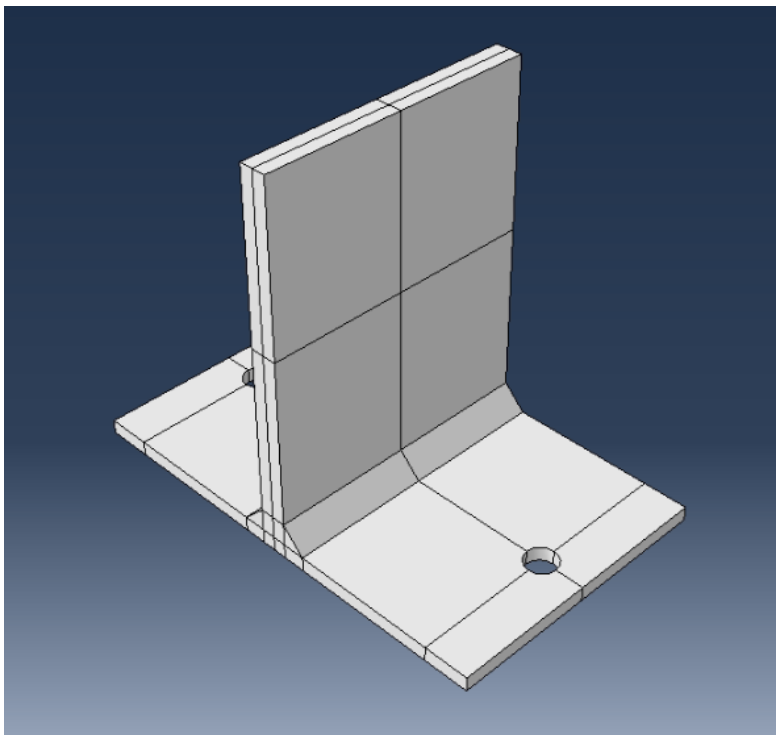

Figure 4.5: Modelling of the T-stub for the experimental essay T-S-HR-8

4.1.4 The assembly

Once all components are modelled, *the assembly* of the elements can be performed. The interactions between the contact surfaces must be defined in Abaqus. A hard contact is assumed in the normal direction to prevent any interpenetration, and a friction coefficient of 0,3 is applied for tangential behaviour. These interaction properties are assigned to *eleven contact surfaces*.
- Flange to washer in green
- Flange to flange in orange
- Flange to nut in pink
- Flange to shank in dark blue

These contact surfaces are highlighted in Figure 4.6, which shows a cross-section along the width of the assembly at mid-span, intersecting the bolt and the T-stub. This view makes it possible to observe the central region of the bolt.

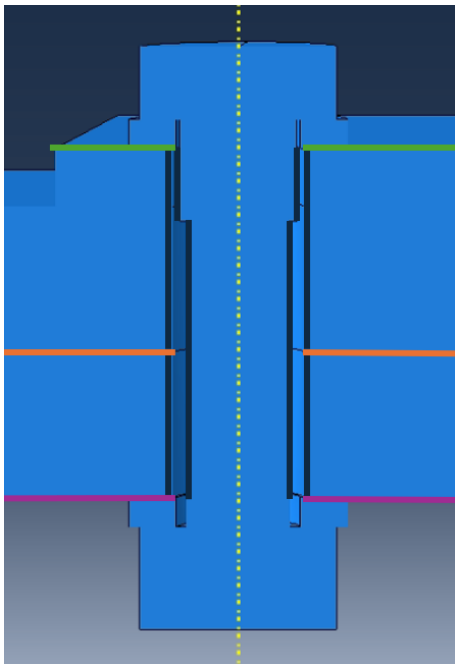

Figure 4.6: Surfaces of interaction

Furthermore, a discussion is conducted regarding the position of the bolt relative to the center of the bolt hole.

4.1.5 Mesh sensitivity

The geometry and size of the mesh can significantly affect the accuracy of the results. A coarse mesh may fail to capture important local behaviours, while a finer mesh improves precision but may introduce numerical instabilities and increase computational cost. Therefore, different mesh configurations are compared for a fixed bolt position.

In the Figure 4.7, the reference curve is compared to four numerical curves obtained using Abaqus, each corresponding to a different mesh configuration. All the tests are made with the improved method to model the bolt.

Options	Base [mm]	Bolt [mm]	T-stub [mm]
Option 1	5	2	2
Option 2	10	2	2
Option 3	5	3	2
Option 4	5	2	4

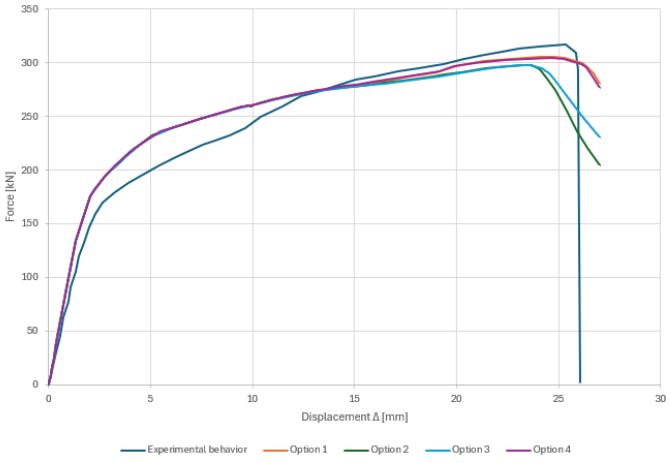

Figure 4.7: Mesh sensibility analysis

The initial portions of the curves for all four options are identical. Subsequently, the curves can be grouped into two distinct categories: Option 2 and Option 3 reach a lower ultimate resistance compared to Option 1 and Option 4.

As a result, Option 2 and Option 3 are set aside, as they deviate more significantly from the reference curve. This is consistent with the fact that the base mesh in Option 2 and the bolt mesh in Option 3 are coarser. In contrast,Option 1 and Option 4 provide ultimate resistance values close to the reference and are therefore both considered acceptable. To ensure sufficient accuracy and avoid overlooking any localized behaviours, Option 1 which uses a thiner mesh for the T-stub, has been selected for the remainder of the study. An additional test with a much thiner mesh (1 mm) was attempted, but the computational time proved to be excessive. *Thus, Option 1 represents the best compromise between accuracy and efficiency.*

4.1.6 Position of bolts

The mesh configuration has now been selected. However, no specific details are provided regarding the position of the bolt relative to the bolt hole. Therefore, *three configurations have been tested in Abaqus*: with the bolt positioned at the hole axis, at the inner edge of the hole, and at the outer edge of the hole (Figure 4.8).

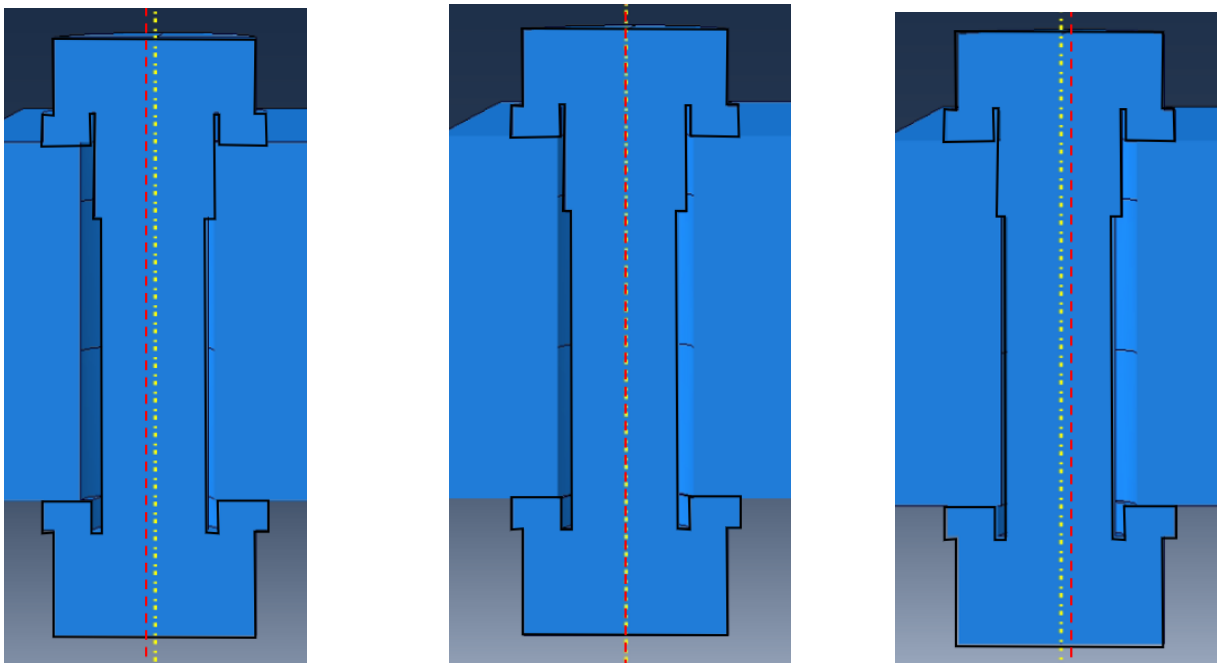

(a) Decentred bolt closer to the web

(b) Centred bolt compared to the bolt axis

(c) Decentred bolt closer to the edge of the T-stub

Figure 4.8: Positions of the bolt

For comparison purposes, the mesh size is fixed at 5 mm for the base, and 2 mm for both the T-stub and the bolt. All corresponding curves are presented in the Figure 4.9.

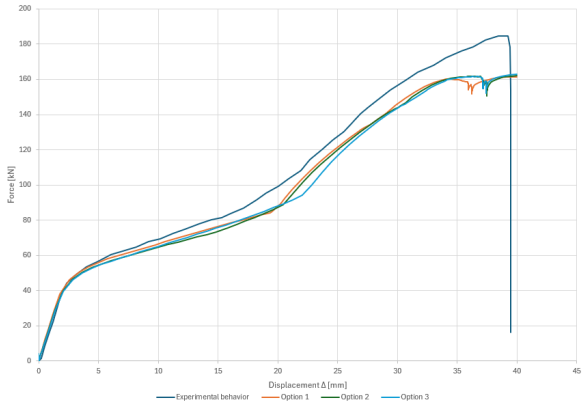

(a) Positions of bolt for the T-stub T-S-HR-8

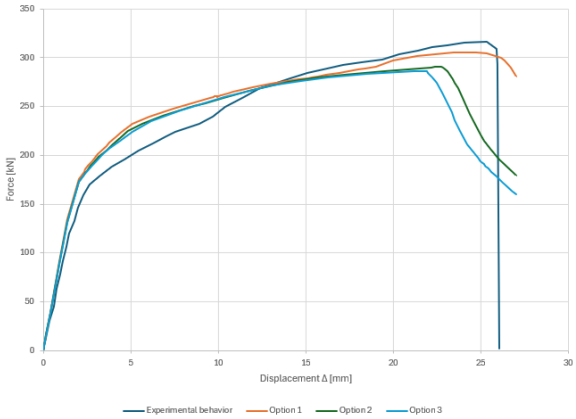

(b) Positions of bolt for the T-stub T-S-HR-20

Figure 4.9: Determination for the most adequate position of the bolt

In this figure, Option 1 corresponds to the case where the bolt is offset toward the inner edge, closer to the web; Option 2 represents the bolt centered in the hole; and Option 3 corresponds to the bolt offset toward the outer edge.

For the T-stub T-S-HR-8, the variation in bolt positions has a negligible effect on the overall behaviour. The only noticeable differences among the three curves appear at the transition from the plastic phase to the onset of the catenary effect. A numerical instability is also observed near the end of the response.

In contrast, for the T-S-HR-20 specimen, more significant differences are observed. The three curves exhibit similar behaviour during the elastic phase and the transition to plasticity. *However, Option 1 provides results that are closest to the experimental ultimate force and therefore appears to best represent the physical behaviour.*

The bolt position that results in the highest ultimate resistance and the most realistic mechanical response is adopted for the remainder of this study.

When the bolt is positioned closer to the inner edge of the bolt hole, Option 1, the ultimate resistance increases. Conversely, as the bolt is placed further from the web, Option 3 , the resistance tends to decrease. One possible explanation for this trend is that a bolt decentered towards the web engages more quickly in the load transfer, whereas a bolt positioned near the outer edge delays washer engagement due to its distance from the initial deformation zone.

It is particularly noteworthy that the position of the bolt within the bolt hole has a significant influence on the force–displacement response according to these simulations. Despite this, *Eurocode 3 does not currently consider the impact of bolt-hole positioning in its design recommendations.*

4.2 Comparison between experimentals and numerical models

As previously explained, to initiate the study, two experimental tests are first examined in details to validate the use of Abaqus as a reliable simulation tool. These two models correspond to specimens T-S-HR-8 and T-S-HR-20, derived from Tartaglia's experimental study. The objective is to accurately replicate these tests in Abaqus by closely matching the physical configuration, including the positioning of bolts and the optimization of the mesh. This ensures that the numerical results approximate the experimental data as closely as possible.

The comparative results are presented below:

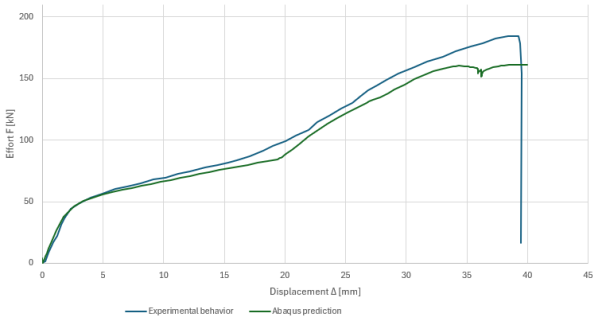

(a) Results for the T-stub T-S-HR-8

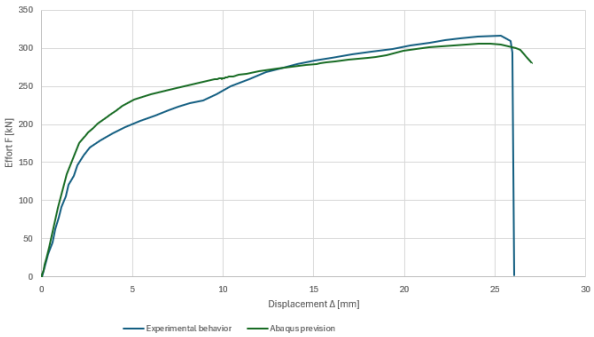

(b) Results for the T-stub T-S-HR-20

Figure 4.10: Comparison between the experimental behaviour of the specimens and the ABAQUS prevision

It can be observed that the numerical and experimental curves exhibit a reasonably good agreement, although the two curves do not perfectly coincide.

This discrepancy can primarily be attributed to several simplifying assumptions. The most significant limitation lies in the incomplete material characterization—detailed information regarding the material's constitutive laws is lacking. Furthermore, no specific data are available concerning the sensors used in the experimental setup or their precise placement. As a result, deviations may arise if the displacement measurements were not taken at identical locations in both the experiment and the simulation.

Additionally, in the referenced experimental study, professional-grade sensors were not employed. Displacement data were instead derived from the testing machine itself, which may introduce measurement errors due to small relative displacements between the testing machine grips and the specimen web.

To further support the validity of the Abaqus simulations, a comparison was conducted between the displacement-force curves provided in the original study, those recalculated using the same experimental framework, and the results obtained in the present simulation. The comparison, shown below, demonstrates that the curve obtained in this study is more closely aligned with the one presented in the original publication.

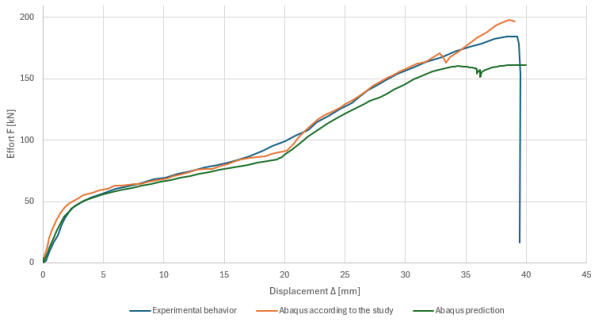

(a) Results for the T-stub T-S-HR-8 and comparatif with the Abaqus results according to the study

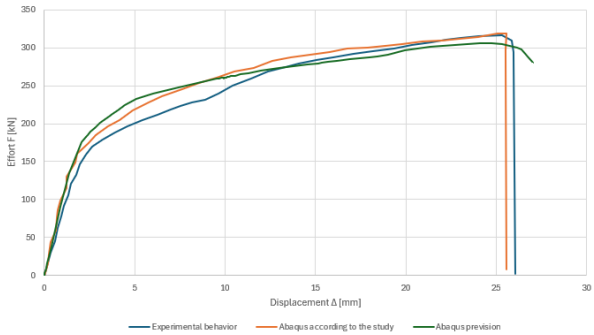

(b) Results for the T-stub T-S-HR-20 and comparatif with Abaqus results according to the study

Figure 4.11: Comparison between the experimental behaviour of the specimens, the Abaqus results according to the study and Abaqus prevision

This level of agreement is considered sufficient to conclude that the Abaqus software is capable of producing results that are in good accordance with experimental observations.

In the study by Tartaglia [**11**], the bolts are also assumed to be preloaded. However, no specific information is provided regarding the magnitude of this preload. Following several simulations, it becomes possible to assess the influence of bolt preloading. Figure 4.12 presents a comparison between the experimental results, the simulation results without any bolt preload, and the results obtained with bolts preloaded to the maximum value prescribed by the Eurocode: $0,7 \cdot f_{u,b} \cdot A_s/1,1 = 114\,217N$.

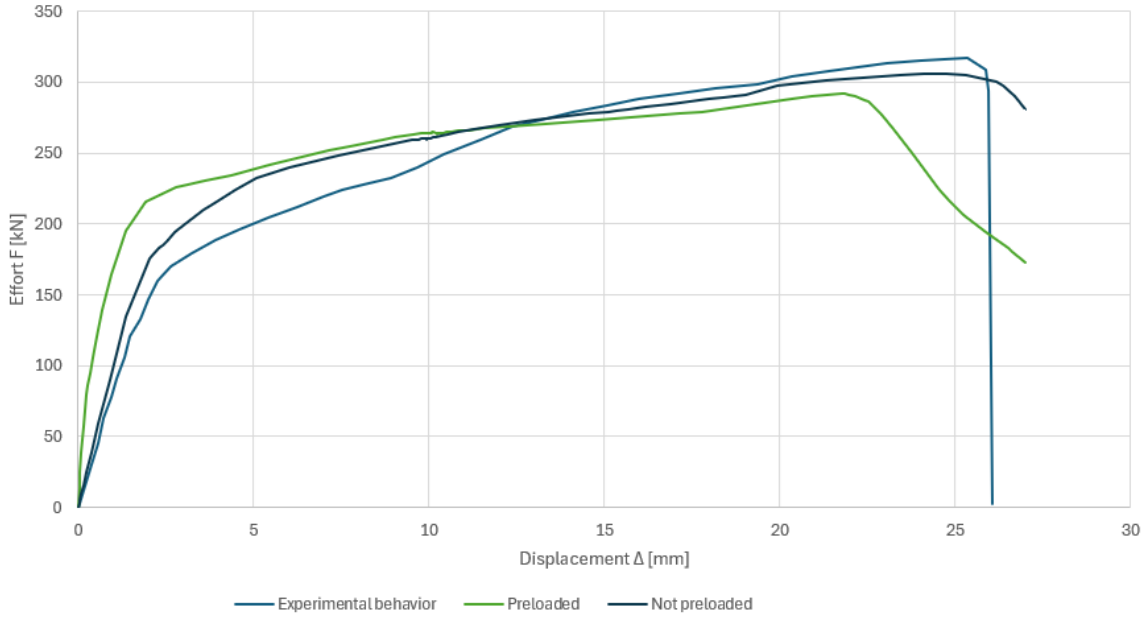

Figure 4.12: Results for the T-stub T-S-HR-20 and comparatif with Abaqus of the using of preloaded bolts

It can be observed that the preload primarily affects the pre-yielding part of the force-displacement curve, but not in a consistent or predictable manner. Attempting to determine the exact preload force applied to the bolts would shift the focus of this thesis toward a calibration exercise, which is not its intended objective. Therefore, in this study, bolts will be considered as not preloaded, especially since the simulations without preload provide results that better match the experimental data.

4.3 The length of a short T-stub

Thanks to this modelling approach, which appears to closely reflect the actual behaviour, it is now possible to investigate the response of the T-stub in more detail. By examining the distribution of equivalent plastic strain, the yield line pattern can be observed.

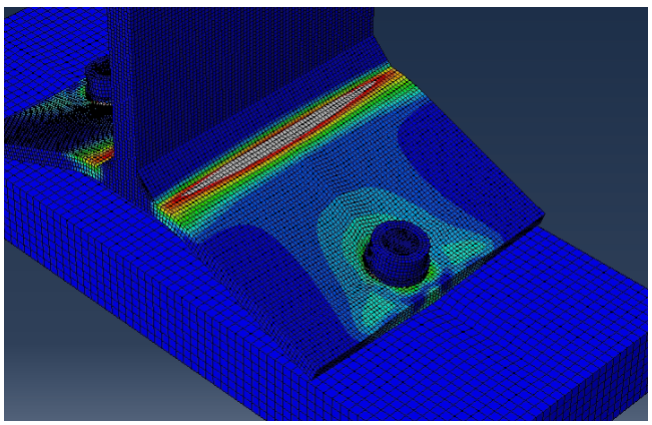

Figure 4.13: Yield line pattern for the T-stub T-S-HR-8

First, it is evident from Figure 4.13 that the yield line pattern does not consist of two straight lines. In order to conduct a high-quality parametric study, it is essential to control the parameters by varying only one at a time, to clearly understand its influence. As previously discussed, the effective length l_{eff} remains a topic of debate. To address this, a working condition has been established whereby only *short T-stubs* are considered. Although the T-stubs in question were predicted to be short according to the referenced article, this is not actually the case.

To satisfy this condition, the original width of 155 mm is reduced to ensure that the yield line pattern consists of two straight lines.

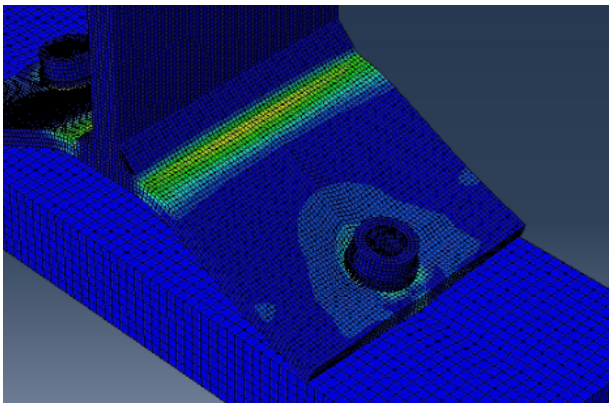

(a) Yield line pattern for a T-stub of 130 mm width

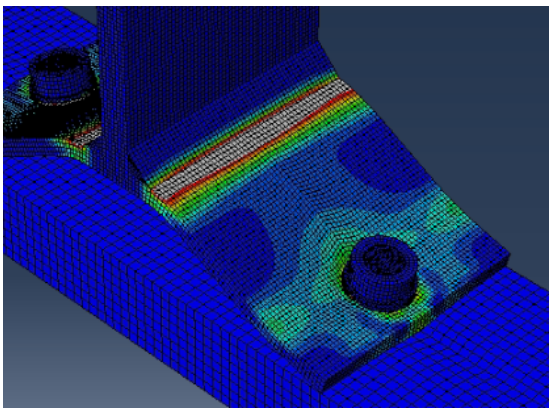

(b) Yield line pattern for a T-stub of 110 mm width

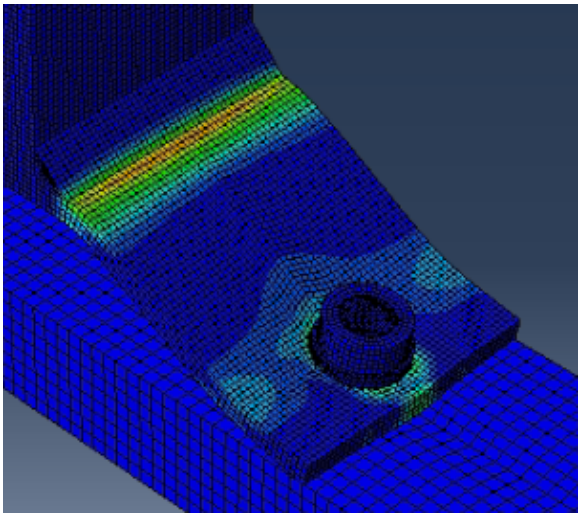

(c) Yield line pattern for a T-stub of 90 mm width

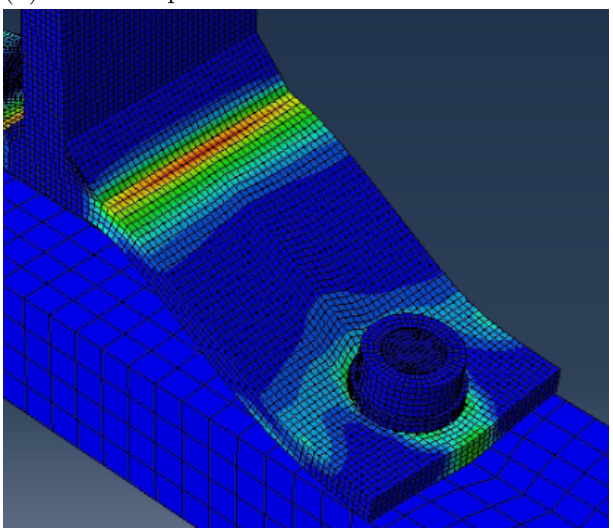

(d) Yield line pattern for a T-stub of 70 mm width

Figure 4.14: Different tests for the length of the T-stub

The yield line pattern observed for the initial T-stub looks like the mechanism identified by Zoetmijer. A transition in the yield line pattern is observed at widths of 130 mm and 110 mm. In the two shorter cases, a second line begins to appear, although the overall shape more closely looks like the improved yield line mechanism developed by Neutelers and Warnant which is characterized by a combination of a straight line and a circular arc around the bolt hole.

In these cases, *the edge distance e*, defined as the distance between the bolt axis and the edge of the flange, is very small. This configuration significantly *influences both the prying forces and the resulting yield line pattern.*

To maintain a standard and representative configuration, all subsequent specimens used in the parametric study is modified to have *a total flange width of 90 mm and an edge distance e of 50 mm.*

This configuration produces a yield line pattern that closely matches the theoretical mechanism described in the state-of-the-art.

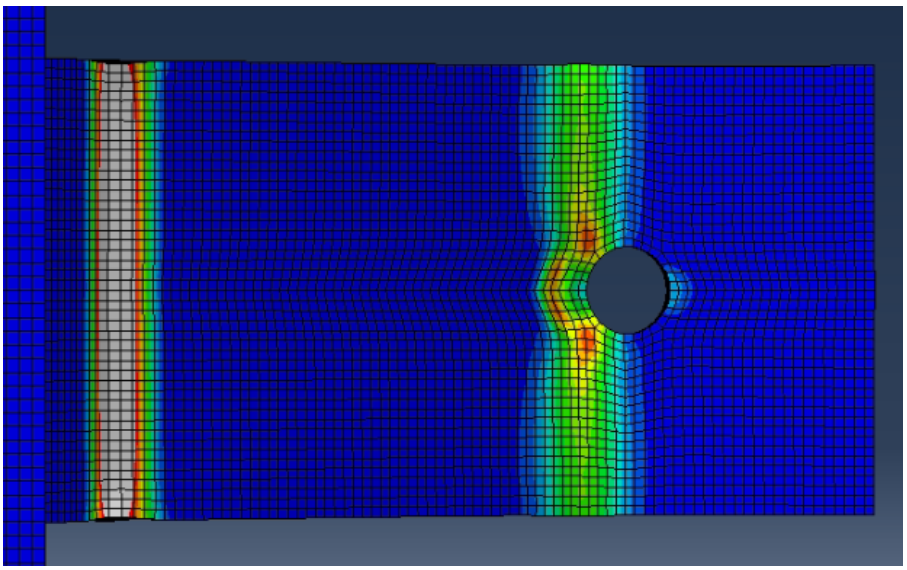

Figure 4.15: Yield line pattern with the modification of L and e

4.4 Summary

In conclusion, our modelling approach in Abaqus has proven to be a reliable tool for obtaining results that *closely approximate experimental observations*. Although the numerical results are not perfectly identical to the experimental data due to some missing input information, they remain sufficiently accurate to support further analysis.

In the next phase of this thesis, the bolts are modelled using an improved approach and positioned eccentrically, toward the inner edge near the web. Additionally, the T-stub flange width is fixed at 90 mm, with an edge distance e set to 50 mm. To ensure high precision, the mesh size is refined to a minimum of 2 mm for both the bolt and the T-stub, and 5 mm for the base plate.

The comparison between experimental and Abaqus results demonstrates good agreement, validating the use of this modelling approach. Consequently, it can be confidently extended to perform a comprehensive parametric study.

This section already reveals a shortcoming in Eurocode 3, as it does not account for the position of the bolt within the bolt hole.

Chapter 5

Parametric analysis

From the previous chapter, it has been observed that several studies have investigated T-stubs connected to a rigid base, as well as symmetric T-stubs. However, the literature appears to lack analysis of configurations in which *one T-stub is slightly thicker than the other*. A parametric study exploring the influence of such geometric variations would therefore be of significant interest.

To carry out this parametric study, *the non-linear finite element software Abaqus* is employed. The initial step involved validating the numerical model by ensuring that the results produced by Abaqus are consistent with available experimental data. In the previous chapter, two main specimens connected to a rigid base have been selected for this validation, which has yielded conclusive results.

In this chapter, following the selection of parameters and boundary conditions for the analysis, *an initial set of specimens* is defined. This set serves as the starting point for the parametric study and allows for a preliminary series of conclusions to be drawn. Additional specimens may be modelled as needed to refine the results and enhance the precision of the analysis.

5.1 Choosen parameters and assumptions

The objective of this analysis is to cover *a wide range of configurations*. To ensure the study is as effective and informative as possible, it is essential that, in the final comparison, configurations differ by only one parameter at a time. The most efficient way to achieve this is by employing *dimensionless parameters*.

In this thesis, three dimensionless parameters are used, each of which is assigned *three distinct values*. This approach enables a systematic and scalable comparison of the influence of each parameter while minimizing interaction effects.

5.1.1 Dimensionless parameters

The three dimensionless parameters influence various characteristics of the T-stub. In this thesis, each parameter is defined as a ratio between two geometric dimensions. As an illustration, the measurements used are shown on the T-stub in Figure 5.1.

The three imposed values are chosen arbitrarily, but they are consistent with the geometries of T-stubs used in experimental studies.

- 1^{st} **parameter:** $\frac{t_f}{C} \in [0,1; 0,2; 0,3]$: This parameter represents the ratio *between the T-stub flange thickness and the distance from the bolt axis to the weld toe.* Physically, this dimensionless ratio characterizes *the relative flexibility between the flange and the bolt.*

A low value of the parameter, such as 0,1, indicates a slender T-stub, where the flange is relatively flexible compared to the bolt. In such cases, the deformation of the flange dominates the behaviour. This ratio can also be interpreted as a measure of the interaction between flange deformation and the axial elongation of the bolt, thereby influencing the overall mechanical response of the T-stub connection.

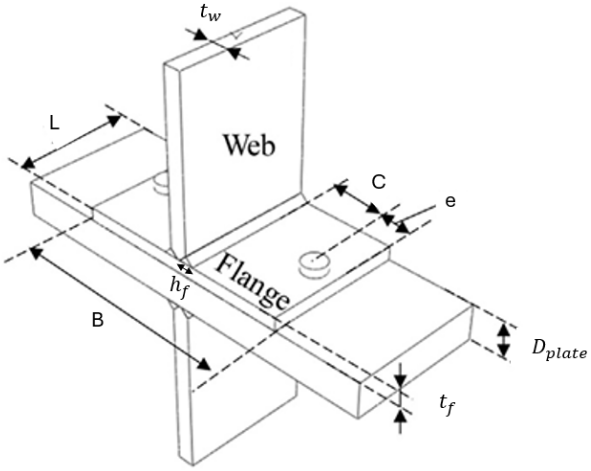

Figure 5.1: The geometry of the T-stub

This initial parameter set can be defined using the equation provided below.

$$(\frac{t_f}{C})' = \frac{Deflection_{T-stub}}{Elongation_{Bolt}} = \frac{\frac{P \cdot L^3}{48 \cdot E \cdot I}}{\frac{P}{\frac{E_b \cdot \pi \cdot \frac{d_b^2}{4}}{L_b}}} = \frac{\pi \cdot d_b^2 \cdot (2 \cdot C + 2 \cdot h_f + t_w)^3}{16 \cdot L \cdot (t_f + d_{plate}) \cdot t_f^3}$$

When the parameter t_f/C is equal to 0,1, the deflection of the T-stub is significantly greater than the elongation of the bolt, resulting in a high value of the derived parameter $(t_f/C)'$. In this thesis, for $t_f/C = 0,1$, the corresponding value of $(t_f/C)'$ ranges between 170 and 310. In contrast, when $t_f/C = 0,3$, the bolt elongation and the T-stub deflection are more comparable, and $(t_f/C)'$ falls within the range of 10 to 25. The comparison table of these two parameters is provided in Appendix B.

- 2^{nd} **parameter:** $\frac{t_f}{d_b} \in [0,7; 0,9; 1]$: The relation between *the flange thickness and the diameter of the bolt.*

- 3^{rd} **parameter:** $\frac{t_f}{d_{plate}} \in [0,6; 0,75; 0,9]$: The relationship between *the thickness of the flange and the one of the base.* It allows us to evaluate the system's behaviour across a range of configurations, from a rigid base to a symmetrical T-stub.

For instance, when the parameter is equal to 0,6, the base is significantly thicker than the flange, corresponding to a rigid base scenario. Conversely, when the parameter approaches 0,9, the system tends toward a more symmetrical configuration, where the flange and the base have comparable thicknesses.

To define an appropriate range for the dimensionless parameter, this ratio was calibrated from the four short specimens with HR bolts from the Tartaglia study.

Specimen	t_f/C	t_f/d_b	t_f/d_{plate}
T-S-HR-8	0,1	0,5	0,2
T-S-HR-12	0,2	0,75	0,3
T-S-HR-15	0,1875	0,9375	0,375
T-S-HR-20	0,25	1,25	0,5

Table 5.1: The ratio of the dimensionless parameter for the Tartaglia essay

Now that the parameters have been defined, the initial set of specimens for the parametric analysis can be established. To cover all possible combinations, *a first series of 27 specimens* has been selected. To identify all the specimen, they are named with the logistics "T" for T-stub than the diameter of the bolt following by the ratio t_f/C, the ratio t_f/d_b and the ratio t_f/d_{plate}.

	Name	d_b [mm]	t_f [mm]	C [mm]	d_{plate} [mm]	e [mm]	t_w [mm]	h_f [mm]	L [mm]	B [mm]	e_1 [mm]
1	T-16-01-07-06	16	11,2	112	18,67	50	15	12,5	90	364	45
2	T-14-01-07-075	14	9,8	98	13,07	50	15	12,5	90	336	45
3	T-16-01-07-09	16	11,2	112	12,44	50	15	12,5	90	364	45
4	T-16-01-09-06	16	14,4	144	24	50	15	12,5	90	428	45
5	T-14-01-09-075	14	12,6	126	16,8	50	15	12,5	90	392	45
6	T-18-01-09-09	18	16,2	162	18	50	15	12,5	90	464	45
7	T-18-01-1-06	18	18	180	30	50	15	12,5	90	500	45
8	T-16-01-1-075	16	16	160	21,33	50	15	12,5	90	460	45
9	T-20-01-1-09	20	20	200	22,22	50	15	12,5	90	540	45
10	T-16-02-07-06	16	11,2	56	18,67	50	15	12,5	90	252	45
11	T-12-02-07-075	12	8,4	42	11,2	50	15	12,5	90	224	45
12	T-12-02-07-09	12	8,4	42	9,33	50	15	12,5	90	224	45
13	T-16-02-09-06	16	14,4	72	24	50	15	12,5	90	284	45
14	T-16-02-09-075	16	14,4	72	19,2	50	15	12,5	90	284	45
15	T-14-02-09-09	14	12,6	63	14	50	15	12,5	90	266	45
16	T-16-02-1-06	16	16	80	26,67	50	15	12,5	90	300	45
17	T-16-02-1-075	16	16	80	21,33	50	15	12,5	90	300	45
18	T-16-02-1-09	16	16	80	17,78	50	15	12,5	90	300	45
19	T-16-03-07-06	16	11,2	37,33	18,67	50	15	12,5	90	214,67	45
20	T-20-03-07-075	20	14	46,67	18,67	50	15	12,5	90	233,33	45
21	T-16-03-07-09	16	11,2	37,33	12,44	50	15	12,5	90	214,67	45
22	T-16-03-09-06	16	14,4	48	24	50	15	12,5	90	236	45
23	T-14-03-09-075	14	12,6	42	16,8	50	15	12,5	90	224	45
24	T-16-03-09-09	16	14,4	48	16	50	15	12,5	90	236	45
25	T-16-03-1-06	16	16	53,33	26,67	50	15	12,5	90	246,67	45
26	T-16-03-1-075	16	16	53,33	21,33	50	15	12,5	90	246,67	45
27	T-18-03-1-09	18	18	60	20	50	15	12,5	90	260	45

Table 5.2: Geometrical properties for the specimens of the parametric study

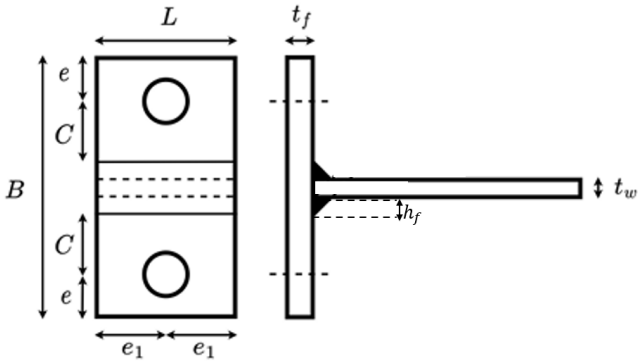

Figure 5.2: Geometry of the parametric study

5.1.2 Material's constitutive laws

To maintain consistency across the parametric study, all specimens is modelled using *S355 structural steel*. With this material selection established, the next step is to define *the appropriate constitutive law* for the material behaviour. Three modelling approaches are available in this context.

The first approach involves using an idealized elastic–perfectly plastic constitutive law, defined in terms of true stress–true strain. The second approach seeks to provide a more realistic representation of material behaviour. This can be achieved using the Yun–Gardner curve, as recommended in the Eurocode 3 [**16**]. For this method, the material response can be implemented either using the engineering stress–strain curve or the true stress–true strain curve. The true stress–true strain curve provides a more accurate representation of material behaviour by accounting for the change in cross-sectional area during loading.

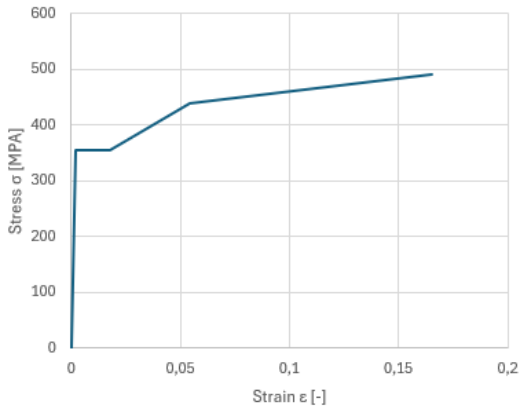

(a) Yun Gardner Engineering

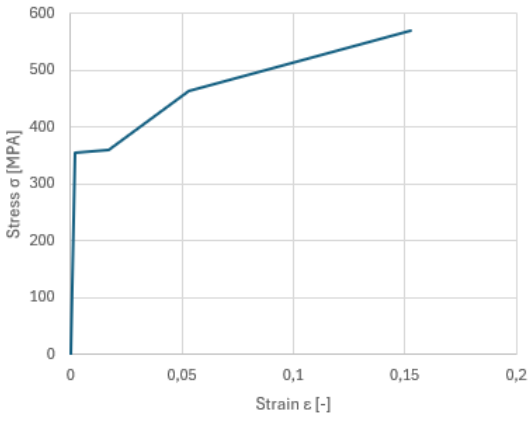

(b) Yun Gardner True stress-true strain

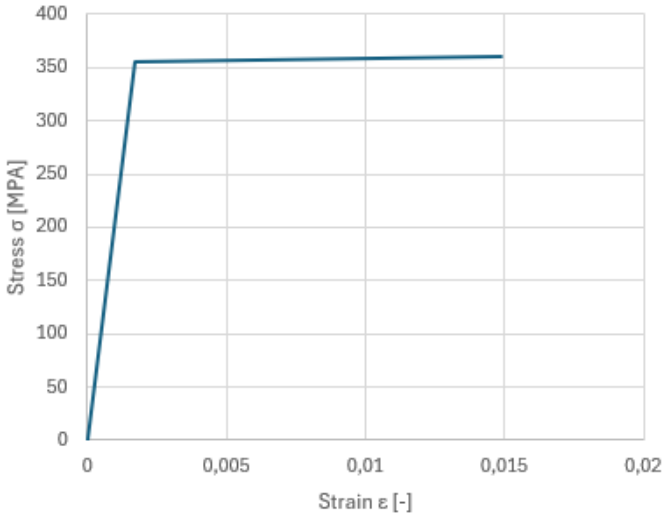

(c) Elastic-perfectly plastic True stress-true strain

Figure 5.3: Material's constitutive laws S235

To identify the most suitable constitutive law, a reference specimen is analysed using each of the proposed material models. The results obtained for each case are then compared to evaluate the influence of the chosen stress–strain curve on the structural response.

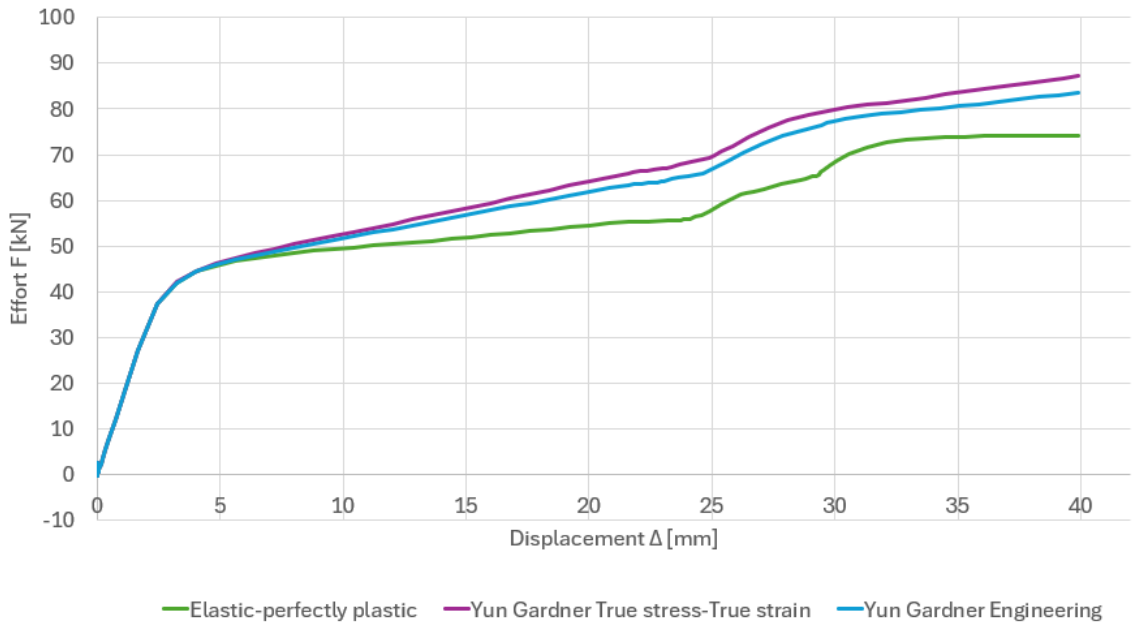

Figure 5.4: Results with different material's constitutive law

Although the three constitutive models produce slightly different results, the overall response remains similar in shape. It is observed that the two models based on the Yun–Gardner curve yield smoother responses, particularly when it's compared to the elastic–perfectly plastic model. However, since the primary objective of this thesis is to understand the behaviour and variation in behaviour of the T-stub connection, *the elastic–perfectly plastic model is preferred* for the T-stub and the base. This simplification facilitates the identification of key transitions in the response.

It must be noted, however, that this assumption limits the accuracy of the model near ultimate failure. The chosen material's constitutive law does not capture strain hardening or damage mechanisms, and therefore, *conclusions drawn near the ultimate state should be interpreted with caution.*

5.1.3 The measurement

Another important point to clarify is the location at which displacements are measured. In the experimental study by Tartaglia, *the precise position of the displacement measurements is not specified.* However, for the sake of consistency throughout the parametric study, a clear and consistent measurement location must be defined from the outset.

If the displacement is measured at the end of the web, the recorded value would include the deformation of both T-stub webs as well as the base plate displacement, thereby capturing a global elongation. Alternatively, the displacement can be taken directly at the flange level, by measuring *the relative displacement between the T-stub flange and the base flange.* This approach isolates the deformation due solely to the T-stub and the base, excluding other sources of elongation.

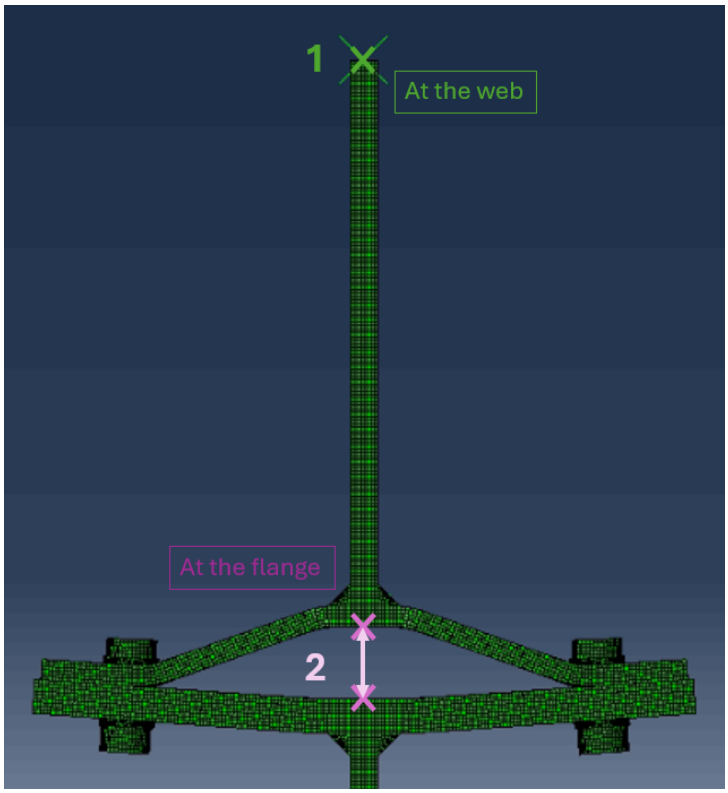

Figure 5.5: Different points of measurement

If the displacement is measured at the end of the web, the recorded value would include the deformation of both T-stub webs as well as the base plate displacement, thereby capturing a global elongation. Alternatively, the displacement can be taken directly at the flange level, by measuring *the relative displacement between the T-stub flange and the base flange.* This approach isolates the deformation due to the T-stub and the base, excluding other sources of elongation.

The latter option is more appropriate and accurate for the purpose of this study. It provides a clearer understanding of the local behaviour of the T-stub and forms a more reliable basis for comparison with analytical and numerical models.

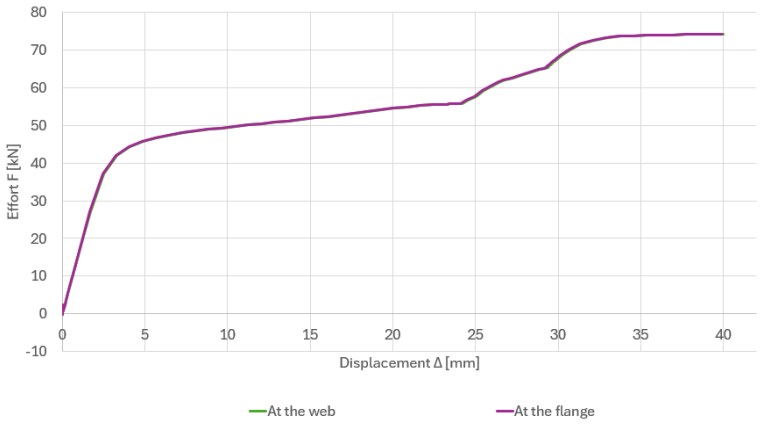

Figure 5.6: Results with different point of measure

As shown in Figure 5.6, the difference between the two displacement curves is negligible. However, to remain as close as possible to the actual deformation that should be considered, the displacement for all specimens in the parametric study are measured as *the relative displacement between the base and the T-stub at the midpoint along the length of the T-stub flange.*

5.2 Analysis of the results

Once all specimens were defined, they were modelled in Abaqus, allowing for the extraction of key behavioural data. Initially, the parametric analysis revealed a behavioural response that is rarely discussed in the literature. This new observation is addressed first. Subsequently, specific behaviours is examined in greater detail, particularly those that *affect parameters* used in the Eurocode approach and which may lead to improved modelling strategies.

Following this, a more systematic analysis is carried out by varying one *dimensionless parameter* at a time to better understand its influence. A discussion then focuses on the presence or absence of *membrane effects*, and how such effects may potentially enhance the performance of the connection.

Finally, all the analytical models presented in Section 2.3 and Section 2.4 is compared to the numerical results, to evaluate how accurately they predict the plastic resistance of the T-stub connection.

5.2.1 Coupled deformations

In general, the behaviour of T-stubs is studied either by considering a T-stub fixed to a rigid base—where only the T-stub undergoes deformation, as in the experimental campaigns presented in Section 3.1—or by analysing a symmetrical T-stub configuration, in which two identical T-stubs are connected back-to-back and deform symmetrically, as in the thesis of A. Neutelers [**2**]. In practice, these configurations represent idealized cases and do not always reflect real connection conditions. It is therefore of interest to investigate whether the behaviour of the T-stub significantly changes in more general configurations.

In this thesis, the dimensionless parameter $\frac{t_f}{d_{plate}}$, which ranges from 0,6 to 0,9, enables a transition from a configuration where the base plate is twice as thick as the T-stub flange to one approximating a symmetrical T-stub. This range allows for the evaluation of how varying base plate stiffness influences the overall response of the T-stub.

In this context, two significally different behaviours can be observed.

The first case corresponds to a T-stub deforming primarily according to failure mode 1, while the base remains sufficiently stiff and rigid to resist.

In contrast, the second case—somewhat unexpected—shows the T-stub still deforming in mode 1, but with the base plate also undergoing deformation. In this configuration, the base responds with a deformation pattern looking like a failure mode 2 or a failure mode 1, indicating that both components contribute to the overall mechanism.

The two images in Figure 5.7 illustrate the two configuration types. The yield line patterns are highlighted in colour.

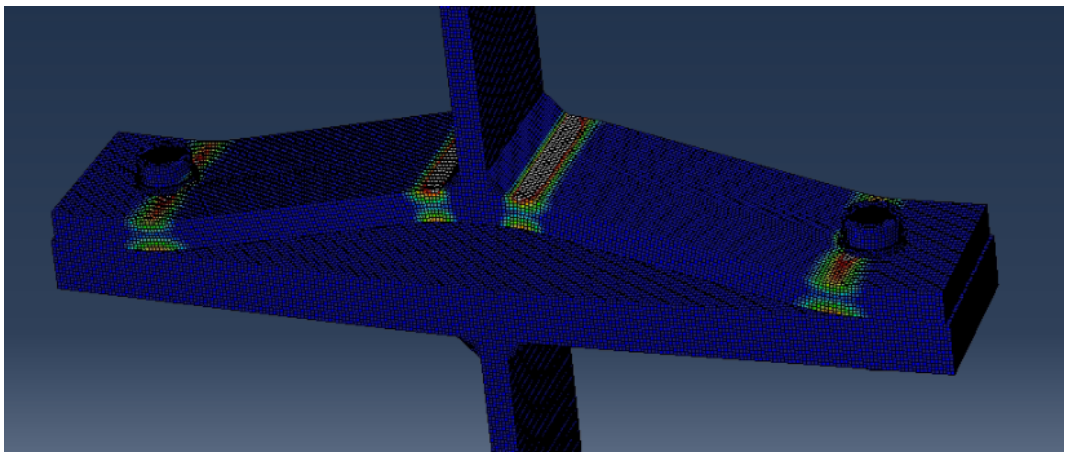

(a) Rigid Base for the specimen 7 : T-18-01-1-06

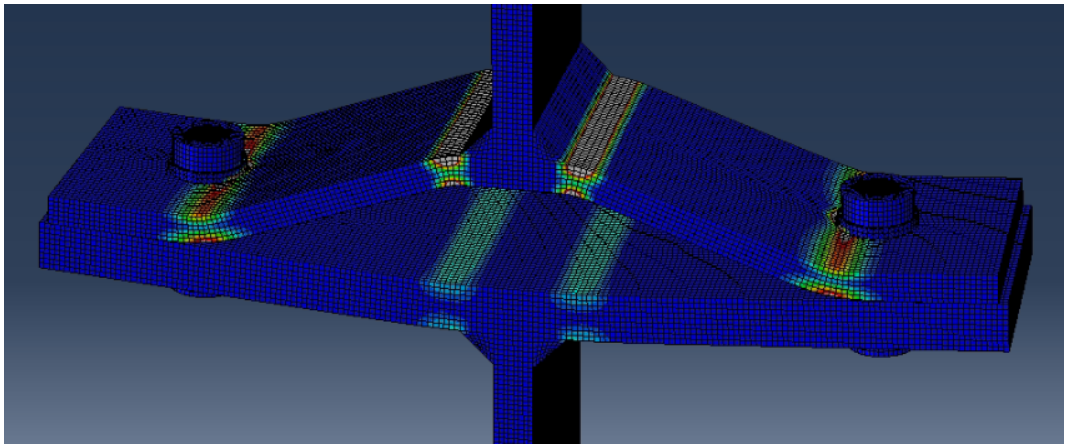

(b) Coupled effects for the specimen 1 : T-16-01-07-06

Figure 5.7: Plastic hinges for two different specimens

This coupled behaviour has not been extensively studied in the existing literature. Among the full set of specimens analysed, 8 exhibit a *rigid-base response*, while all others demonstrate *coupled effects* involving simultaneous deformation of the T-stub and the base plate.

Based on the parameters examined in this thesis, it was not possible to define a consistent criterion to predict the occurrence of coupled behaviour prior to numerical modelling. Moreover, this type of behaviour seems to reduce the demand on the bolts, as the T-stub and the base accommodate most of the deformation. Consequently, the bolts experience delayed loading and reach their ultimate resistance at a later stage. This behaviour stay an hypothesis.

However, it has been observed that when *the dimensionless parameter* $\frac{t_f}{d_{plate}} = 0,9$, the coupled behaviour is always present. This is consistent with expectations, as such a configuration closely resembles the symmetrical T-stub case, where both sides of the connection deform in a coordinated manner. Those cases are highlighted in blue in the Table 5.3.

	Name	t_f/d_b	t_f/C	t_f/d_{plate}	Coupled effects	Failure mode of the base
1	T-16-01-07-06	0,7	0,1	0,6	OUI	Mode 2
2	T-14-01-07-075	0,7	0,1	0,75	OUI	Mode 2
3	T-16-01-07-09	0,7	0,1	0,9	OUI	Mode 1
4	T-16-01-09-06	0,9	0,1	0,6	OUI	Mode 2
5	T-14-01-09-075	0,9	0,1	0,75	OUI	Mode 2
6	T-18-01-09-09	0,9	0,1	0,9	OUI	Mode 1
7	T-18-01-1-06	1	0,1	0,6	NON	/
8	T-16-01-1-075	1	0,1	0,75	OUI	Mode 2
9	T-20-01-1-09	1	0,1	0,9	OUI	Mode 2
10	T-16-02-07-06	0,7	0,2	0,6	NON	/
11	T-12-02-07-075	0,7	0,2	0,75	OUI	Mode 2
12	T-12-02-07-09	0,7	0,2	0,9	OUI	Mode 1
13	T-16-02-09-06	0,9	0,2	0,6	OUI	Mode 2
14	T-16-02-09-075	0,9	0,2	0,75	NON	/
15	T-14-02-09-09	0,9	0,2	0,9	OUI	Mode 1
16	T-16-02-1-06	1	0,2	0,6	OUI	Mode 2
17	T-16-02-1-075	1	0,2	0,75	OUI	Mode 2
18	T-16-02-1-09	1	0,2	0,9	OUI	Mode 1
19	T-16-03-07-06	0,7	0,3	0,6	NON	/
20	T-20-03-07-075	0,7	0,3	0,75	OUI	Mode 2
21	T-16-03-07-09	0,7	0,3	0,9	OUI	Mode 2
22	T-16-03-09-06	0,9	0,3	0,6	NON	/
23	T-14-03-09-075	0,9	0,3	0,75	NON	/
24	T-16-03-09-09	0,9	0,3	0,9	OUI	Mode 2
25	T-16-03-1-06	1	0,3	0,6	NON	/
26	T-16-03-1-075	1	0,3	0,75	NON	/
27	T-18-03-1-09	1	0,3	0,9	OUI	Mode 1

Table 5.3: The presence or not of the coupled effects

5.2.2 Hinges position

During the tests, plastic hinges are observed to form in the T-stub. In the case of failure mode 1, one plastic hinge develops near the weld, and another near the bolt. *According to the Eurocode 3 [4], the hinge near the bolt is assumed to lie along the bolt axis, while the hinge near the weld is predicted to occur at a distance of* $0,8 \cdot h_f$ *from the web face.*

With the model in Abaqus, the actual positions of the plastic hinges can be identified. On the Figure 5.8, the true hinge locations, derived from the simulations, are shown in pink dotes, while the undeformed geometry is represented in black, and the Eurocode 3 predictions are indicated with a blue dashed line.

(a) The position of the hinge close to the weld for the T-stub

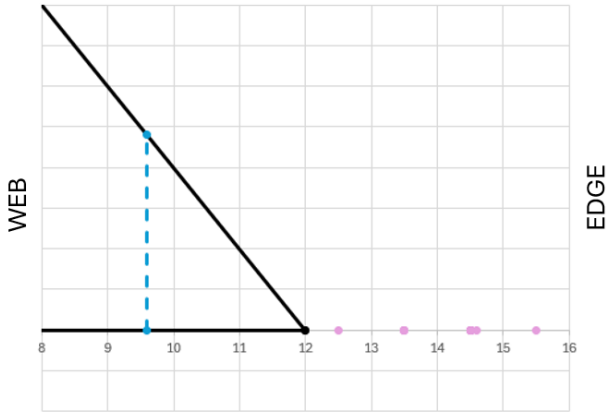

(b) The position of the hinge close to the weld for the Base

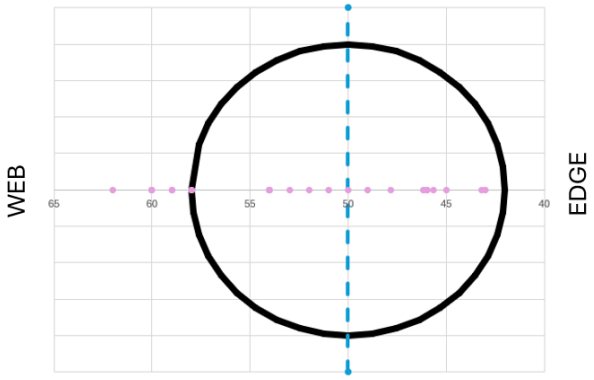

(c) The position of the hinge close to the bolt for the T-stub

Figure 5.8: Comparison between the real position of the hinge and the position predicted by the Eurocode

It is clearly observed that *the Eurocode 3 does not accurately predict the position of the plastic hinge near the weld*, while *the predicted position of the hinge near the bolt is more consistent* with the simulation results. However, a small subset of specimens shows hinge locations slightly outside the circular zone defined by the bolt diameter.

Upon further analysis, it appears that all specimens, exhibiting an plastic hinge outside of the circular zone, share a common parameter value of $t_f/C = 0,1$. This implies that the modified parameter $(t_f/C)'$ is significantly high, indicating that the flange is considerably more flexible than the bolt, leading to greater out-of-plane deformation of the flange compared to bolt elongation.

The actual hinge positions can also be compared with those predicted by alternative models. The Struik and De Back model provides a less accurate prediction for the hinge near the weld, assuming a location at $0,5 \cdot h_f$, which underestimates the true distance. Zhao's model adopts the same hinge assumptions as the Eurocode 3, and therefore yields similar inaccuracies.

In contrast, the Neutelers model introduces a more sophisticated calculation method that significantly improves the prediction of the hinge location near the bolt. However, the accuracy of the predicted hinge position near the weld remains unsatisfactory, showing little improvement over the Eurocode approach.

Table 5.4 compares the positions of the plastic hinges in both plates with the predictions obtained using Neutelers's method. The relative error is then calculated to highlight both the most and least accurate predictions. The cases highlighted in green correspond to results with an error below 5%, indicating high accuracy. In contrast, the red-highlighted cases represent the poorest predictions, where the error exceeds 10%.

		Hinge close to the bolt			Hinge close to the weld		
	Name	Real position	Prediction	Error [%]	Real position	Prediction	Error [%]
1	T-16-01-07-06	60	60,69	1,15	16,5	15,81	-4,17
2	T-14-01-07-075	59	59,88	1,5	15,5	15,79	1,91
3	T-16-01-07-09	62	61,05	-1,52	16,5	15,81	-4,13
4	T-16-01-09-06	59	60,26	2,15	16,5	15,8	-4,21
5	T-14-01-09-075	58	59,5	2,59	16,5	15,79	-4,3
6	T-18-01-09-09	60	58,45	-2,57	14,5	15,77	8,77
7	T-18-01-1-06	58	57,99	0	14,5	15,76	8,71
8	T-16-01-1-075	58	60,31	3,99	14,5	15,8	8,99
9	T-20-01-1-09	60	63,45	5,76	14,5	15,85	9,36
10	T-16-02-07-06	53	55,08	3,92	15,5	15,7	1,35
11	T-12-02-07-075	45,65	53,6	17,42	15,5	15,68	1,16
12	T-12-02-07-09	47,82	53,72	12,34	14,5	15,68	8,15
13	T-16-02-09-06	54	54,6	1,21	14,5	15,7	8,28
14	T-16-02-09-075	49	54,88	12,01	14,5	15,7	8,31
15	T-14-02-09-09	52	54,42	4,65	14,7	15,69	6,77
16	T-16-02-1-06	54	54,46	0,86	15,5	15,69	1,27
17	T-16-02-1-075	54	54,7	1,3	14,5	15,7	8,29
18	T-16-02-1-09	54	54,87	1,62	14,5	15,7	8,31
19	T-16-03-07-06	43	51,79	20,45	13,5	15,64	15,88
20	T-20-03-07-075	50	52,95	5,91	14,5	15,66	8,05
21	T-16-03-07-09	45	52,15	15,9	13,5	15,65	15,94
22	T-16-03-09-06	46,15	51,37	11,31	14,5	15,63	7,83
23	T-14-03-09-075	43,2	51,19	18,51	14,7	15,63	6,34
24	T-16-03-09-09	46	51,76	12,54	13,5	15,64	15,88
25	T-16-03-1-06	46	51,18	11,26	14,5	15,63	7,8
26	T-16-03-1-075	46	51,42	11,78	14,5	15,63	7,84
27	T-18-03-1-09	51	51,49	0,97	14,5	15,63	7,85

Table 5.4: Comparison of the real hinge position and the hinge position predicted by the Neutelers method

5.2.3 Prying force distribution

Another point of interest is the location of the prying forces. *According to the Eurocode 3 [4], these forces are assumed to act at the plate edge or at a distance of* $1,25 \cdot m$ *from the bolt axis.*

Based on the results of the parametric analysis, it appears that in most cases, the prying force is indeed applied at the edge.

However, 3 out of the 27 specimens exhibit *a different behaviour*, in which the prying force is applied at a certain distance from the flange edge. This differences can be observed in the two screenshots from the Abaqus simulation shown in Figure 5.9. *The prying force distribution* is visualised in Abaqus through *the contact pressure* plots: regions with the highest contact pressure appear in grey or red. Conversely, the regions shown in dark blue, constituting the majority of the area, indicate a lack of contact at those locations.

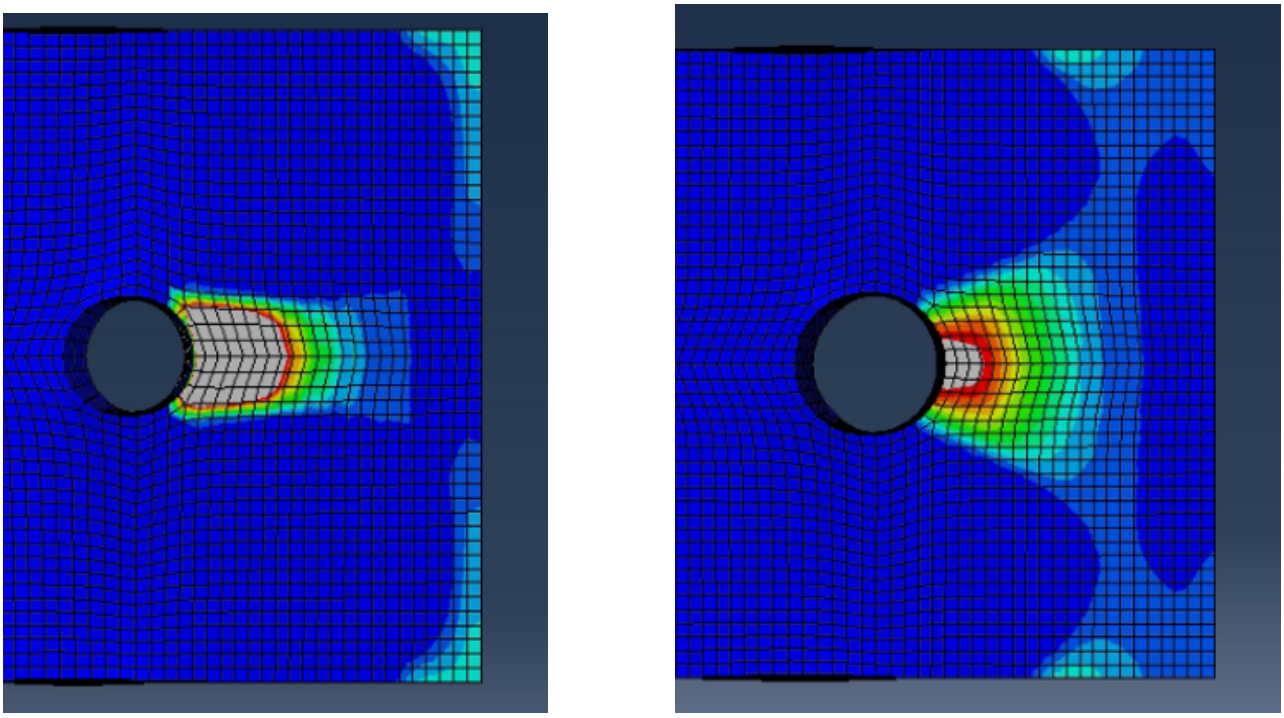

(a) The common behaviour for the prying force specimen 2 : T-14-01-07-075

(b) The other behaviour for the prying force specimen 6 : T-18-01-09-09

Figure 5.9: Different location for the prying force

This second behaviour, occurs only under *the specific conditions where* $t_f/C = 0,1$ *and* $t_f/d_{plate} = 0,9$. These values indicate that the flange exhibits significantly higher flexibility compared to the bolt, and that the base and T-stub dimensions closely approach a symmetrical configuration.

Given the uniqueness and potential implications of this behaviour, it is worthwhile to investigate this phenomenon further. To deepen the analysis, a 4^{th} **parameter** has been introduced. The dimensionless parameter C/e has been varied across the values [3;4;5,5] to explore the influence of the edge distance e on both the location and magnitude of the prying force, as well as the global force–displacement response. A total of nine new specimens have been modelled with the previously fixed conditions : $t_f/C = 0,1$ and $t_f/d_{plate} = 0,9$.

This extended parametric study investigates whether variations in e influence the mechanics of prying force distribution. The geometric characteristics of the newly defined specimens are provided in Table 5.5.

	Name	d_b [mm]	t_f [mm]	C [mm]	d_{plate} [mm]	e [mm]	t_w [mm]	h_f [mm]	L [mm]	B [mm]	e_1 [mm]
1’	T-16-01-07-09-3	16	11,2	112	12,44	37,33	15	12,5	90	338,66	45
2’	T-16-01-07-09-4	16	11,2	112	12,44	28	15	12,5	90	320	45
3’	T-16-01-07-09-5,5	16	11,2	112	12,44	20,36	15	12,5	90	304,72	45
4’	T-16-01-09-09-3	16	14,4	144	16	48	15	12,5	90	424	45
5’	T-16-01-09-09-4	16	14,4	144	16	36	15	12,5	90	400	45
6’	T-16-01-09-09-5,5	16	14,4	144	16	26,18	15	12,5	90	380,36	45
7’	T-16-01-1-09-3	16	16	160	17,77	53,33	15	12,5	90	466,66	45
8’	T-16-01-1-09-4	16	16	160	17,77	40	15	12,5	90	440	45
9’	T-16-01-1-09-5,5	16	16	160	17,77	29,09	15	12,5	90	418,18	45

Table 5.5: Specimens for the complementary analysis

With the results obtained from the additional specimens, it has been demonstrated that *variations in the length of e indeed influence the distribution of the prying force.* As the value of e decreases, a clear shift in the distribution pattern is observed, as illustrated in the Figure 5.10.

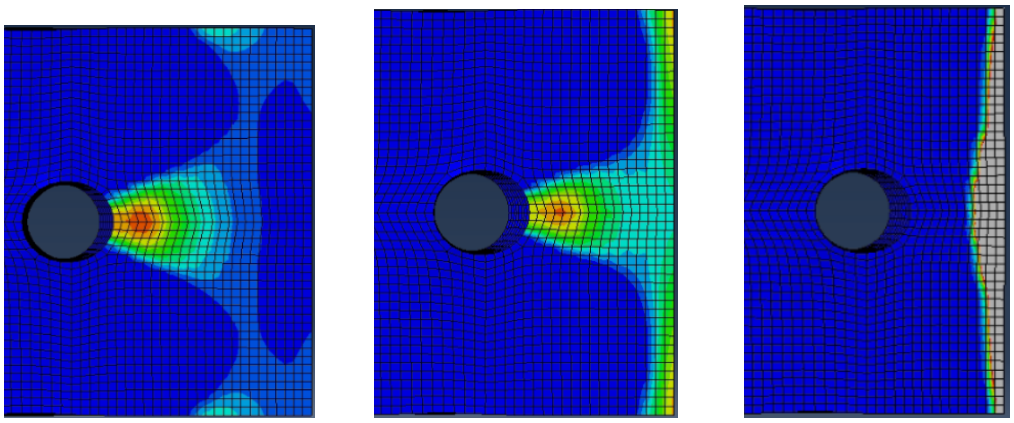

(a) The prying force distribution for the specimen 7' : T-16-01-1-09-3 with e = 53,33 mm

(b) The prying force distribution for the specimen 8' : T-16-01-1-09-4 with e = 40 mm

(c) The prying force distribution for the specimen 9' : T-16-01-1-09-5,5 with e = 29,09 mm

Figure 5.10: Evolution of the prying force distribution as a function of the length e

The results suggest that, in addition to the two cases currently considered in the Eurocode 3, there exists a third configuration in which the prying force is applied at an intermediate distance from the flange edge.

A more in-depth analysis reveals that, even among three geometrically similar specimens differing only in the value of the length e, the overall response observed in the force–displacement curve *remains largely unaffected* as it shown in the Figure 5.11. *This indicates that variations in the distribution of the prying force do not significantly influence the global resistance of the joint.*

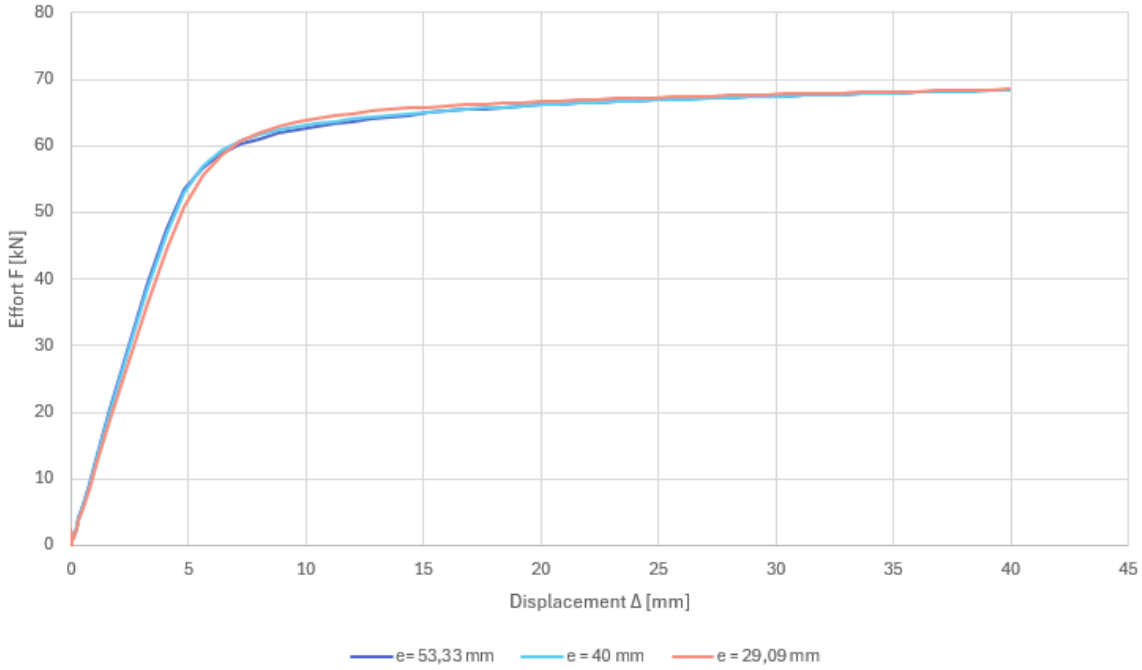

Figure 5.11: Results for specimens with different length for e.

5.2.4 Stress distribution under the bolt head

Another relevant aspect to investigate is the stress distribution beneath the bolt head. The contact pressure, as provided by Abaqus, offers also the stress distribution under the bolt head. In this thesis, it is particularly important to analyse two distinct cases: the stress distribution on the flange of the T-stub and the stress distribution on the flange of the base.

A comparison between the numerical results and the assumptions made by various analytical models is of particular interest. In the Eurocode 3, the initial method assumes *a concentrated load applied at the bolt axis*, whereas a more refined approach considers *an uniformly distributed pressure beneath the bolt head*. The Zhao model can also be applied using the same two load distribution assumptions proposed by the Eurocode 3.

While Struik and De Back consider *a concentrated load acting at the inner edge of the bolt hole*, Neutelers conducted a more detailed analysis of the contact behaviour and proposed *a triangular pressure distribution under the washer*.

This variation in load distribution *affects the formulation of the resistance for failure mode 1*. This refinement has led to the development of two distinct methods for calculating this resistance in the Eurocode 3. Further improvement of the formula is possible by *refining the value of* e_w, which represents the distance between the bolt axis and the equivalent load application point. *According to the Eurocode 3,* e_w *is taken as* $d_w/4$ *for a uniformly distributed load*. However, A.Neutelers proposed a simple yet effective solution to account for the triangular distribution by adopting a refined value of $e_w = \frac{3 \cdot d_w}{8}$, which more accurately represents the actual load transfer conditions.

On the flange

An analysis of the contact pressure on the flange reveals that *the uniform distribution assumed in the Eurocode 3 does not accurately reflect the actual pressure distribution.*

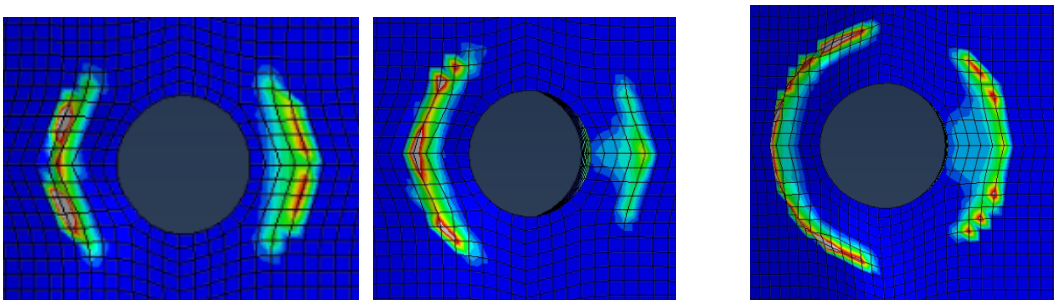

(a) The pressure contact of the flange of the specimen 3 : T-16-01-07-09

(b) The pressure contact of the flange of the specimen 4 : T-16-01-09-06

(c) The pressure contact of the flange of the specimen 20 : T-20-03-07-075

Figure 5.12: The pressure contact of the flange for different specimens

In all cases, the contact pressure takes on *a shape looking like an open parenthesis*, with the pressure being more significant toward the exterior of the flange.

As the T-stub begins to deform, one side tends to move upward while the other remains fixed, leading to the formation of a yield line pattern along the axis of the bolt. This asymmetric displacement induces *bending in the bolt*, which in turn causes stress concentrations at the edge of the washer. Consequently, the assumption of a uniform pressure distribution beneath the washer does not accurately represent the actual contact behaviour.

In this context, *the triangular pressure distribution proposed by A.Neutelers appears to be an appropriate representation of the contact conditions.* In the present parametric analysis, the displacements are significant, and the contact pressure are clearly concentrated at the edge of the washer, further validating the relevance of a non-uniform pressure distribution.

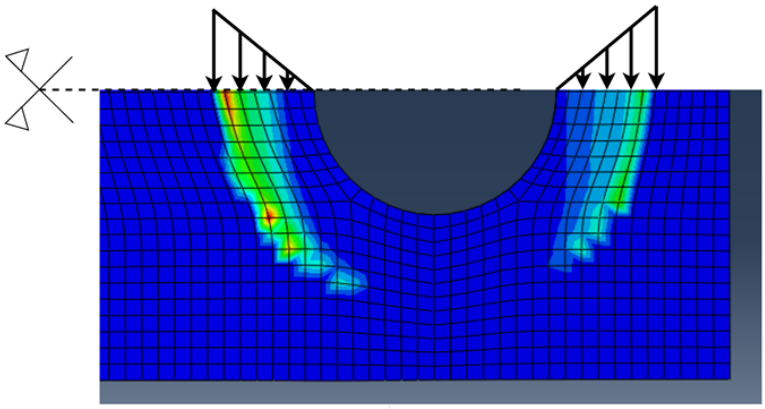

Figure 5.13: The stress distribution proposes in the Neutelers thesis [**2**]

On the base

Regarding the base, the behaviour is quite different. Just as the contact pressure on the flange of the T-stub was analysed, a similar approach can be applied to the base.

The distribution of contact pressure on the base is illustrated in Figure 5.14.

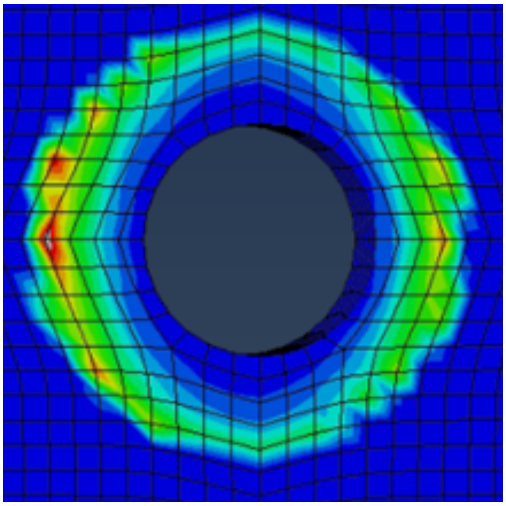

(a) The contact pressure at the start of the simulation

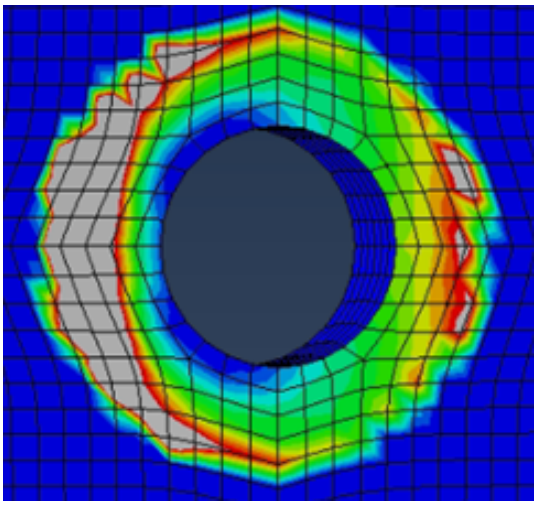

(b) The contact pressure at the end of the simulation

Figure 5.14: The contact pressure of the base of the specimen 3 : T-16-01-07-09

In this case, the contact pressure seems to be *closer to a uniform distribution*, although a parenthesis-like shape still emerges toward the end of the simulation. This suggests that, at the beginning of the loading process (Figure 5.14a), the base is not significantly affected by the bending of the bolt. This observation is consistent with the fact that the base is stiffer than the T-stub, causing the bolt to bend predominantly near the T-stub side. Therefore, assuming a uniform pressure distribution on the base appears to be reasonable in the early stages of deformation.

Toward the end of the simulation (Figure 5.14b), the bending of the bolt does begin to influence the stress distribution on the base. However, this effect remains less pronounced than on the flange side.

In this context, it may be appropriate to consider *an intermediate pressure distribution, such as a trapezoidal shape*, which would better reflect the transition between an uniform distribution and the parenthesis-like pattern observed under the flange. This trapezoidal distribution could offer a more accurate representation of the actual contact behaviour on the base, especially in the later stages of loading.

5.2.5 Variation of the 1^{st} parameter $\frac{t_f}{C}$

This first parameter is varied across three values: 0,1, 0,2 and 0,3. For consistency, assuming a fixed flange thickness of 10 mm, the corresponding values of C (the distance from the bolt axis to the weld toe) are 100 mm, 50 mm, and 33,3 mm, respectively.

When the parameter is small, the T-stub is slender, indicating high flexibility. In this configuration, the flange deforms significantly, and the overall behaviour is dominated by flange bending rather than bolt elongation.

Alternatively, if the reciprocal form of the parameter, $(t_f/C)'$, is considered, a high value reflects a system in which flange deflection plays a much greater role compared to bolt elongation.

Figure 5.15 presents two graphs, each corresponding to fixed values of the parameters t_f/d_b and t_f/d_{plate}. *Three force-displacement curves are plotted on each graph, with each curve representing a different value of the parameter under investigation in this section.*

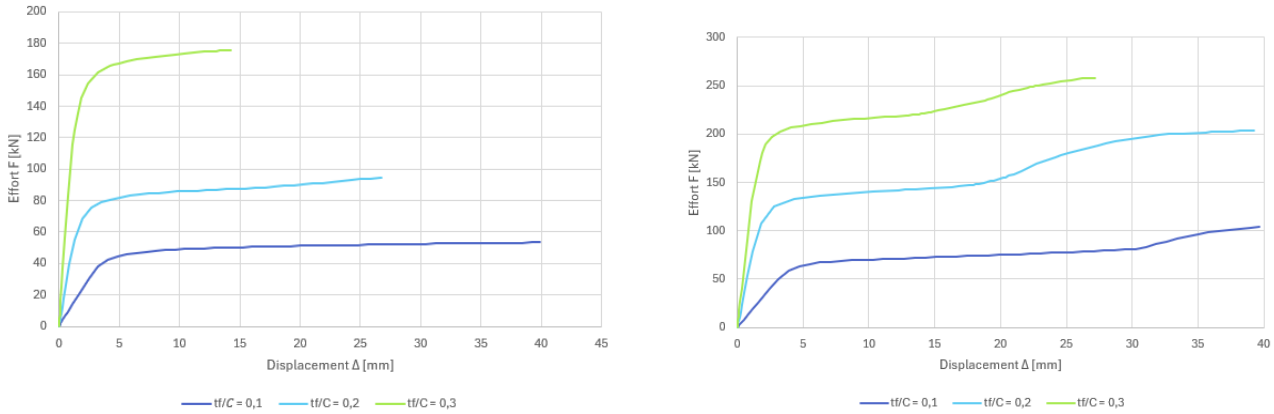

(a) $t_f/d_b = 0,7$ and $t_f/d_{plate} = 0,9$ (b) $t_f/d_b = 1$ and $t_f/d_{plate} = 0,6$

Figure 5.15: The variation of the parameter t_f/C

The behaviour of the three specimens follows a systematic trend: *as the parameter increases and the length C decreases, the plastic resistance increases accordingly.*

In this case, the slope of the elastic portion of the curves is not constant. *A higher parameter value corresponds to a steeper elastic slope.*

It also appears that as the parameter increases, the ultimate displacement observed in Figure 5.15a decreases. However, this observation should be *interpreted with caution*, as the scope and conditions of this thesis do not allow definitive conclusions regarding the ultimate behaviour.

The overall behaviour observed here is consistent with mechanical intuition. A more flexible T-stub, associated with a low parameter value, tends to undergo large displacements without developing significant resistance. Conversely, a thicker and stiffer T-stub (i.e., a higher parameter) quickly develops higher resistance, but is less capable of accommodating large displacements.

5.2.6 Variation of the 2^{nd} parameter $\frac{t_f}{d_b}$

It is interesting to observe the impact of the variation of this second parameter on the system's behaviour.

In particular, it is important to illustrate how this parameter affects the geometry of the T-stub. The parameter takes fixed values of 0,7, 0,9, and 1. Assuming a constant bolt diameter of 16 mm, the flange thickness varies accordingly: 11,2 mm for a value of 0,7, 14,4 mm for 0,9, and 16 mm for 1.

Thus, *as the parameter increases, the flange thickness also increases.* To ensure consistency in the analysis, all other parameters are kept constant.

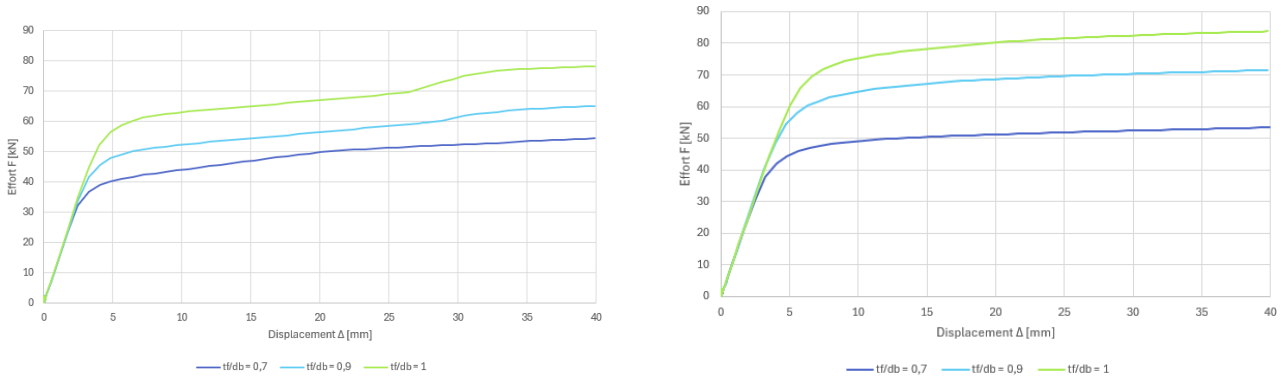

(a) $t_f/C = 0,1$ and $t_f/d_{plate} = 0,75$ (b) $t_f/C = 0,1$ and $t_f/d_{plate} = 0,9$

Figure 5.16: The variation of the parameter t_f/d_b

The behaviour of the three specimens is consistent across all comparisons. For each case, an increase in the parameter corresponds to a thicker flange (assuming a constant bolt diameter), which in turn *leads to a higher plastic resistance.*

Despite the differences in flange thickness, *the elastic slope of the three curves remains identical*, indicating similar stiffness in the initial phase of the response.

5.2.7 Variation of the 3^{rd} parameter $\frac{t_f}{d_{plate}}$

The final parameter to be analysed appears to be the most significant. Remember that the parameter t_f/d_{plate} represents the ratio between the flange thickness and the base plate thickness. A value of 0,6 corresponds to a configuration in which the base plate is nearly twice as thick as the flange. A value of 0,75 represents an intermediate case, while a value of 0,9 approaches a symmetrical configuration where the flange and base have similar thicknesses. Thus, *the higher the parameter t_f/d_{plate}, the thinner the base plate relative to the flange thickness.*

As in the previous comparisons, the other two parameters is held constant to isolate the effect of this variable in the Figure 5.17.

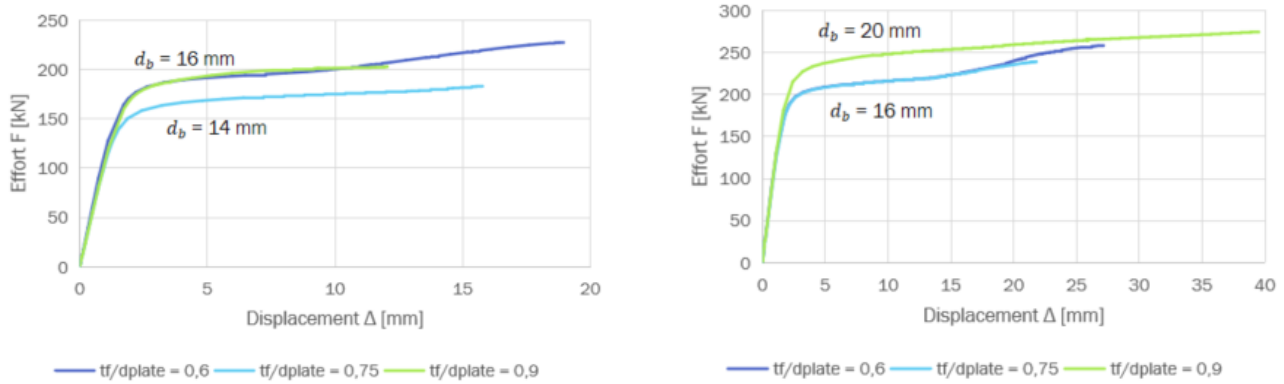

(a) $t_f/d_b = 0,9$ and $t_f/C = 0,3$ (b) $t_f/d_b = 1$ and $t_f/C = 0,3$

Figure 5.17: The variation of the parameter t_f/d_{plate}

From this initial analysis, it is clear that the results are not directly comparable. In previous parameter studies, the variation in bolt diameter did not pose a problem, as d_b was explicitly included in the dimensionless parameter definitions. However, in the case of the current parameter, this is not true. Since the bolt diameter has a direct influence on the plastic resistance, *no reliable conclusions can be drawn if the diameters are not identical across the compared cases.*

To address this issue and enable meaningful comparisons, additional modelling and simulations have been carried out using consistent bolt diameters.

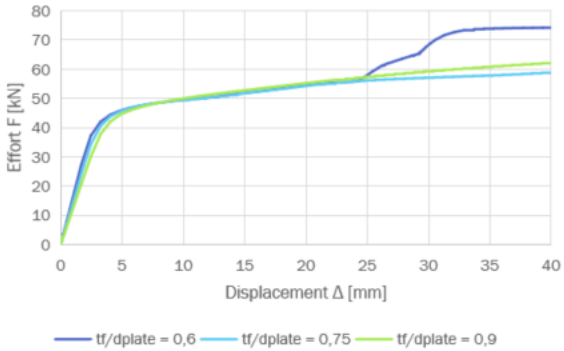

(a) $t_f/d_b = 0,7$ and $t_f/C = 0,1$

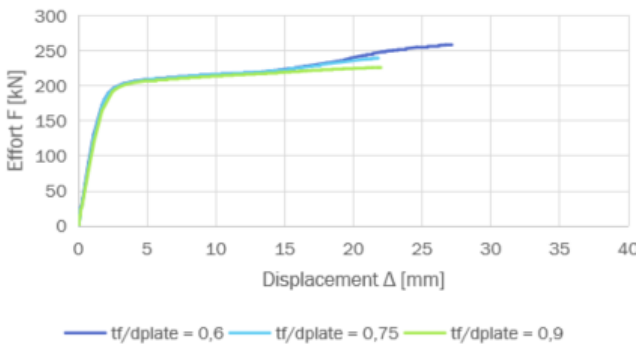

(b) $t_f/d_b = 1$ and $t_f/C = 0,3$

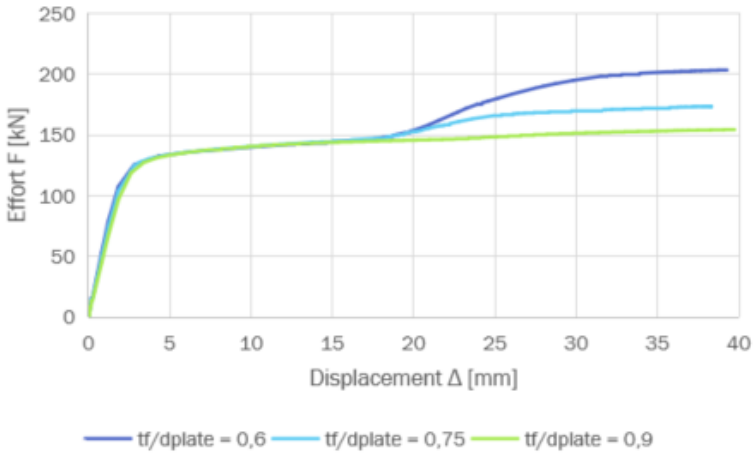

(c) $t_f/d_b = 1$ and $t_f/C = 0,2$

Figure 5.18: The variation of the parameter t_f/d_{plate} with comparable curves

The different curves can now be analysed and compared. All three graphs exhibit *a similar general trend along the loading path. In each case, the slope of the elastic portion is identical, the plastic resistance is the same, and the plastic plateau is comparable across the three parameter values.*

The main distinction between the curves becomes particularly apparent in the final graph (Figure 5.18c). The green curve, which corresponds to a configuration close to a symmetrical T-stub, exhibits a post-yielding behaviour that remains nearly linear and follows the extension of the plastic behaviour. In contrast, the dark blue curve, representing the most asymmetrical configuration, shows a pronounced deviation due to membrane effects developing in the system. The light blue curve, associated with the intermediate parameter value, displays a response that lies between the two extremes, both in shape and mechanical behaviour.

This trend is also observable in Figure 5.18b, although the differences between the curves are less pronounced than in the first graph due to the smaller overall displacements.

In the final graph, Figure 5.18a, only the dark blue curve, corresponding to the configuration with a thick base plate, exhibits clear membrane effects.

The observed evolution aligns with the onset of *membrane effects*, which develop when bending deformation is restrained. In such cases, to accommodate continued deformation, axial forces begin to develop within the flange. For this condition to occur, the base plate must be sufficiently stiff to restrict bending, thus allowing the more flexible T-stub to activate membrane action and ultimately reach higher resistance levels.

It is important to conclude that *the base plate thickness does not significantly affect the yield resistance*. However, it can contribute to a higher ultimate resistance by enabling the development of membrane effects in the later stages of deformation.

In general, based on the various simulations of the specimens tested in this thesis, membrane effects are clearly present when t_f/d_{plate} equals 0,6 and the flange flexibility is high, but not when the parameter $t_f/C = 0,3$.

5.2.8 Membrane effects

As observed in the analysis of the dimensionless parameter t_f/d_{plate}, *membrane effects* can develop, enabling the system to reach higher resistance levels. *The membrane effect refers to the redistribution of stresses in the deformed configuration, leading to the development of tensile forces within the flange.* These membrane actions can arise primarily in two ways: either through *geometric effects*, especially in configurations exhibiting large deformation angles, or through *mechanical constraints* that limit bending, such as the presence of the bolt or a rigid base. In both cases, *the structural system transitions from a predominantly bending-dominated response to one where axial forces* contribute significantly to the overall resistance.

To identify the presence of membrane effects, the force–displacement curve must be carefully analysed. The appearance of membrane action is typically indicated by *an increase in the slope of the curve beyond the plastic part*, reflecting a secondary stiffness associated with axial force development in the deformed flange. The presence or absence of membrane effects can be observed by comparing the two graphs shown in Figure 5.19.

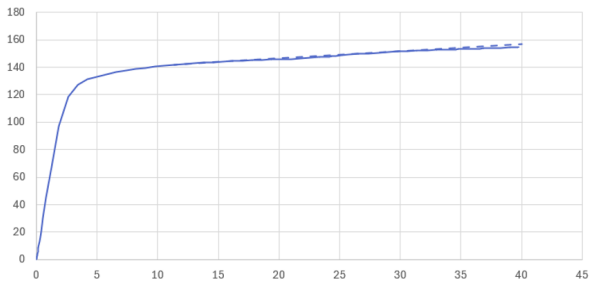

(a) T-stub without membrane effects specimen 18 : T-16-02-1-09

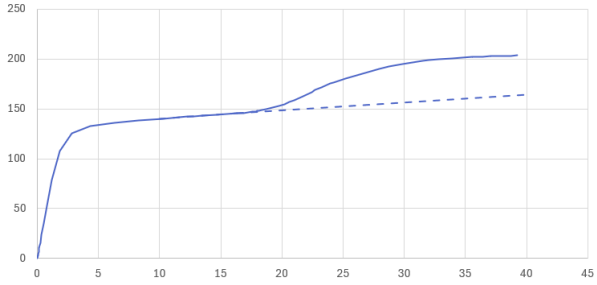

(b) T-stub without membrane effects specimen 16 : T-16-02-1-06

Figure 5.19: Presence or not for two similar effects with the parameter fixed $t_f/d_b = 1$ and $t_f/C = 0,2$

In the present study, the deformation angles are not large enough to trigger membrane effects purely due to geometric considerations. Although the simulations involve significant displacements, the angles at the plastic hinge remain substantial, but *not sufficient to induce membrane action based on geometry alone.*

To investigate the possible presence of membrane effects arising two points along the force–displacement curve have been selected for *detailed observation.* These points allow for an analysis of both the deformation patterns and the internal force distributions within the system.

Point A (in purple) corresponds to *the onset of yielding*, representing the behaviour at the initiation of plastic deformation. In contrast, Point B (in green) corresponds to *the end of the simulation*, where membrane effects have developed and significantly influence the structural response.

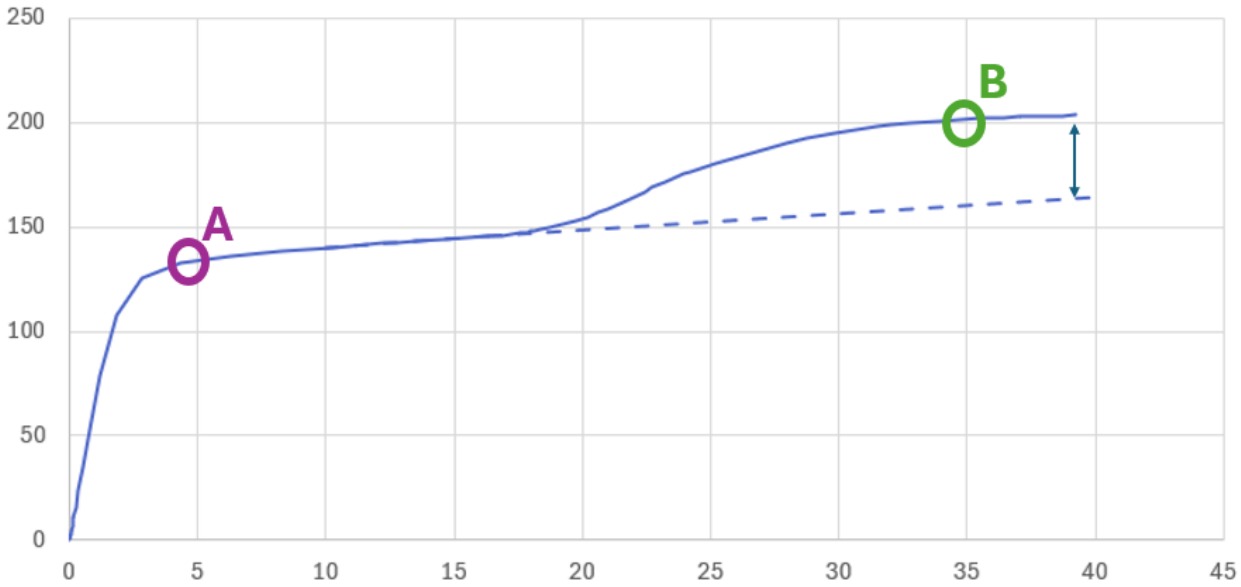

Figure 5.20: Position of the two points analysed on the force-displacement curve.

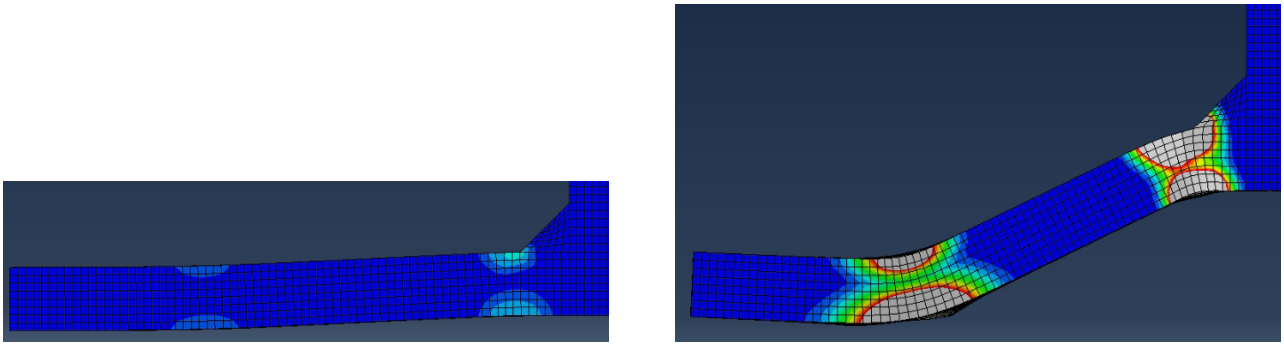

(a) The deformation of the T-stub at the position A specimen 16 : T-16-02-1-06

(b) The deformation of the T-stub at the position B specimen 16 : T-16-02-1-06

Figure 5.21: The deformation of the T-stub at 2 different points

- Point A : At the situation A, the deformed configuration remains very close to the initial undeformed state. The vertical displacement at the center between the T-stub and the base is only about 5 mm (Figure 5.21a). Nevertheless, the early stages of deformation are already visible, particularly the formation of the two plastic hinges and the emergence of the yield line pattern.

  In terms of internal forces (Figure 5.22), *the response is clearly dominated by vertical components*. The force normal to the flange is approximately six times greater than the force along the axis of the flange. Consequently, the resultant internal force vector is oriented almost entirely in the vertical direction.

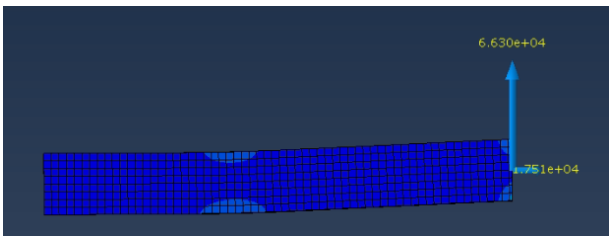

(a) The component

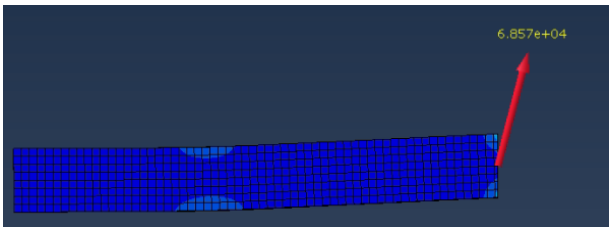

(b) The resultant

Figure 5.22: The internal effort of the T-stub at the position A specimen 16 : T-16-02-1-06

- Point B :At the situation B, the deformation is significantly more pronounced, with a vertical displacement of approximately 40 mm between the flange and the base (Figure 5.21b). *The two plastic hinges are fully developed*, allowing for substantial rotation between the different parts of the flange and between the flange and the web.

  In this configuration, the internal force distribution has evolved significally (Figure 5.23). The dominant component is now the axial force along the flange. *This prevalence of axial force is a clear manifestation of membrane effects.* Quantitatively, the axial force is slightly more than twice the magnitude of the force normal to the flange. As a result, the resultant force vector is oriented almost parallel to the flange.

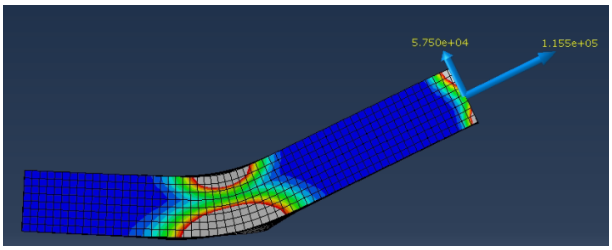

(a) The component

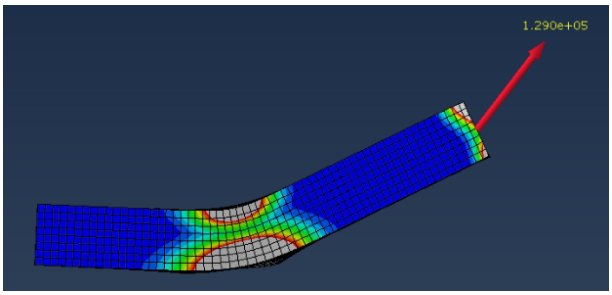

(b) The resultant

Figure 5.23: The internal effort of the T-stub at the position B specimen 16 : T-16-02-1-06

5.2.9 Application of the model on the parametric specimens

The final point of interest is *the evaluation of the analytical models to assess their ability to accurately predict the structural behaviour*. This analysis focuses specifically on *the plastic resistance*, as defined in Section 2.3. The calculation methodology follows the same approach to the experimental specimen T-S-HR-8 that could be find in the Appendix A.

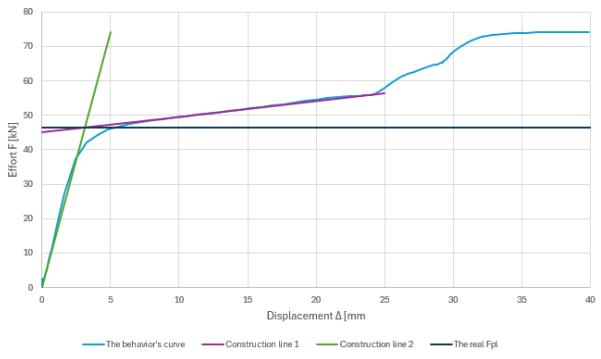

(a) Construction to establish the real Fpl

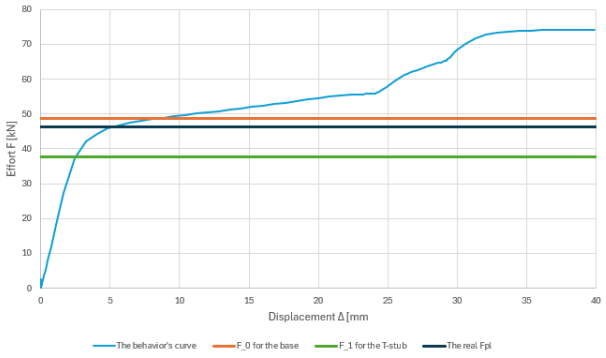

(b) The comparison between the real Fpl and two propositions of the Eurocode 3

Figure 5.24: Application of the Eurocode 3 to the parametric specimen

This type of graph can be developed for all specimens and for each configuration in order to evaluate the plastic resistance.

Additionally, *summary tables are included in the Appendix C, listing the plastic resistance values obtained using analytical models*. The objective is to *identify which analytical model provides the most accurate prediction* of the actual behaviour.

To begin, the reference plastic resistance has been determined using *the intersection method between the elastic and plastic slopes*, as previously described. This value is then compared first to the different formulations proposed in the Eurocode 3.

Subsequently, this reference value is compared with the predictions of the improved analytical models. A comprehensive comparison is then performed across all models of interest to evaluate their accuracy and reliability.

To ensure the analysis remains as readable as possible, the tables presented in the main text show *the relative error between the actual plastic resistance and the values obtained using the corresponding analytical formulas*. Key results are highlighted in bold, while other relevant elements are presented in italics to guide interpretation and support the development of conclusions.

Most of the specimens exhibit *coupled effects*. On the Table 5.6 aside, specimens characterized by a rigid base are marked with blue-colored numbers to clearly distinguish them within the dataset. Moreover, if the number is shown in grey, it indicates that the base deforms according to failure mode 2. Conversely, if the number is shown in pink, it signifies that the base deforms according to failure mode 1.

In this section, the Table 5.7 to the Table 5.12 follow a colour scale with four distinct ranges.

- If the relative error is between 0% and 5%, which corresponds to the most accurate results, it is highlighted in green.
- The next range, from 5% to 15%, represents errors that can still be considered acceptable for model evaluation. These values are shown in yellow.
- The third range, shown in orange, indicates results with relatively poor accuracy.
- Finally, the fourth range, in red, corresponds to the worst predictions, where the relative error is equal to or greater than 25%, indicating incorrect or highly inaccurate results.

	Name	F_{pl} Real [kN]
1	T-16-01-07-06	46,22
2	T-14-01-07-075	39,93
3	T-16-01-07-09	48,31
4	T-16-01-09-06	54,47
5	T-14-01-09-075	49,28
6	T-18-01-09-09	63,73
7	T-18-01-1-06	67,16
8	T-16-01-1-075	60,39
9	T-20-01-1-09	73,08
10	T-16-02-07-06	102,75
11	T-12-02-07-075	79,85
12	T-12-02-07-09	80,82
13	T-16-02-09-06	117,16
14	T-16-02-09-075	114,9
15	T-14-02-09-09	112,16
16	T-16-02-1-06	134,04
17	T-16-02-1-075	131,98
18	T-16-02-1-09	139,18
19	T-16-03-07-06	152,42
20	T-20-03-07-075	212,73
21	T-16-03-07-09	154,45
22	T-16-03-09-06	186,5
23	T-14-03-09-075	167,49
24	T-16-03-09-09	190,96
25	T-16-03-1-06	210,53
26	T-16-03-1-075	204,08
27	T-18-03-1-09	237,83

Table 5.6: Real plastic resistance of the specimens

The Eurocode 3

To begin the analysis, it is relevant to evaluate all the possibilities proposed by the Eurocode 3. The mode 3, which corresponds to bolt failure, is applicable to all specimens and is therefore calculated systematically. Modes 1 and 2 are evaluated using the T-stub thickness as a reference parameter. These modes can be calculated both for the base and for the T-stub. In addition, mode 0 defined in the section 2.6 has also been assessed for the base, to determine whether this alternative could provide a more accurate estimation of the actual plastic resistance.

As a reminder, the Eurocode 3 defines the plastic resistance of the T-stub as the minimum of the values $F_{Rd,1}$, $F_{Rd,2}$, and $F_{Rd,3}$, corresponding respectively to failure modes 1, 2, and 3. According to this methodology, the Eurocode 3 predicts that the T-stub fails in mode 1 each time, which aligns with the observed physical behaviour. However, this prediction is not always the value that most closely matches the actual plastic resistance observed in simulations.

In the Table 5.7, all values shown **in bold** represent the smallest relative errors in each row. These values correspond to the failure mode that provides the closest estimation to the actual plastic resistance.

		Base			T-stub	
	Name	$F_{Rd,0}$ [%]	$F_{Rd,1}$ [%]	$F_{Rd,2}$ [%]	$F_{Rd,1}$ [%]	$F_{Rd,2}$ [%]
1	T-16-01-07-06	***5,18***	126,93	185,40	-18,31	138,54
2	T-14-01-07-075	-32,03	46,54	150,93	**-17,57**	131,07
3	T-16-01-07-09	-55,31	**-3,58**	134,12	-21,84	128,22
4	T-16-01-09-06	*15,31*	146,80	136,70	**-11,15**	81,68
5	T-14-01-09-075	-28,80	52,22	91,67	**-14,38**	69,25
6	T-18-01-09-09	-50,63	**3,68**	87,23	-16,02	80,03
7	T-18-01-1-06	*17,30*	145,87	122,84	**-11,49**	63,91
8	T-16-01-1-075	-25,91	58,13	82,37	**-11,05**	57,58
9	T-20-01-1-09	-46,69	14,94	79,36	**-6,90**	71,24
10	T-16-02-07-06	***-7,39***	107,07	94,64	-25,45	62,69
11	T-12-02-07-075	-43,60	**25,38**	46,82	-29,47	35,20
12	T-12-02-07-09	-61,31	**-13,97**	37,04	-30,32	33,58
13	T-16-02-09-06	***5,42***	132,02	73,69	-16,47	33,31
14	T-16-02-09-075	-31,20	51,41	53,95	**-14,83**	35,93
15	T-14-02-09-09	-57,38	**-6,16**	19,52	-23,99	14,93
16	T-16-02-1-06	***2,73***	124,83	54,80	-19,06	13,86
17	T-16-02-1-075	-33,23	46,14	33,83	-17,80	**15,64**
18	T-16-02-1-09	-56,03	**-3,76**	14,86	-22,05	9,66
19	T-16-03-07-06	***-8,32***	112,42	58,48	-23,53	32,46
20	T-20-03-07-075	-46,78	**24,80**	45,88	-29,80	34,33
21	T-16-03-07-09	-59,79	**-6,83**	34,11	-24,53	30,72
22	T-16-03-09-06	***-2,30***	121,07	35,17	-20,42	3,75
23	T-14-03-09-075	-39,51	37,14	6,52	-22,86	**-5,94**
24	T-16-03-09-09	-57,59	-4,04	5,37	-22,27	**1,32**
25	T-16-03-1-06	***-3,36***	116,87	23,39	-21,93	-9,24
26	T-16-03-1-075	-36,19	43,18	8,36	-19,46	**-6,37**
27	T-18-03-1-09	-57,01	-6,85	**0,20**	-24,55	-4,34

Table 5.7: Visualisation of the best approximation of the plastic resistance with the classic method of the Eurocode 3

Several recurring patterns can be identified and highlighted throughout the results.

- The calculation of the plastic resistance using $F_{Rd,1}$ for the T-stub appears to be a suitable approach, as most cases are associated with an orange color or yellow color, are not completely incorrect. This approximation proves even more accurate when the dimensionless parameter t_f/C is close to 0,1, which reflects a highly flexible T-stub prone to significant deformation.
- For the calculation of $F_{Rd,1}$ applied to the T-stub, the relative error is always negative, which means that this formula consistently underestimates the resistance.
- An unexpected outcome of this method is that, when the T-stub exhibits very low flexibility, the approach identifies the formula for $F_{Rd,2}$ as providing the closest estimate to the actual plastic resistance of the T-stub.
- The formula for $F_{Rd,0}$ applied to the base provides the best approximation in 7 cases. This approach proves particularly effective for a specific pattern highlighted using *italic text*. It is the most accurate when the dimensionless parameter t_f/d_{plate} equals 0,6. Even in the two cases where $F_{Rd,0}$ is not the optimal choice under this condition, the estimated values remains acceptable, making it a reliable alternative for evaluation.
- Similarly, the application of $F_{Rd,1}$ to the base provides a good approximation in cases where the dimensionless parameter $t_f/d_{plate} = 0,9$, which corresponds to specimens approaching a symmetric configuration.

The Eurocode 3 with the real m

As explained previously, the parameter m according to the Eurocode 3 is defined as the distance between the bolt axis and 0,8 times the weld thickness projection. At the beginning of the parametric analysis, it was concluded that this assumption used in the Eurocode 3 does not accurately reflect reality, particularly in the context of the parametric study conducted in this thesis.

All formulas have been recalculated using the actual values of m measured from the Abaqus simulations. This allows us to evaluate whether adjusting the value of m affects the accuracy of the formulas, ideally improving the agreement with the real plastic resistance.

In the Table 5.8, as before, the errors shown **in bold** represent the smallest values in each row, indicating the best estimations.

	Name	Base			T-stub	
		$F_{Rd,0}$ [%]	$F_{Rd,1}$ [%]	$F_{Rd,2}$ [%]	$F_{Rd,1}$ [%]	$F_{Rd,2}$ [%]
1	T-16-01-07-06	22,89	179,43	217,22	**0,59**	165,14
2	T-14-01-07-075	-20,57	80,48	177,68	**1,52**	155,71
3	T-16-01-07-09	-46,69	21,38	163,78	**-1,61**	157,14
4	T-16-01-09-06	28,95	188,20	156,97	**3,75**	97,23
5	T-14-01-09-075	-19,74	79,15	108,62	**0,77**	84,21
6	T-18-01-09-09	-45,86	17,08	100,80	**-5,16**	93,09
7	T-18-01-1-06	25,93	171,27	135,50	**-2,34**	73,22
8	T-16-01-1-075	-19,74	78,23	93,77	**0,25**	67,43
9	T-20-01-1-09	-42,58	29,64	90,29	**5,01**	81,67
10	T-16-02-07-06	8,35	163,88	111,19	**-5,00**	76,51
11	T-12-02-07-075	-42,11	37,15	48,63	**-22,85**	36,87
12	T-12-02-07-09	-59,18	**-2,94**	40,49	-21,38	36,94
13	T-16-02-09-06	19,00	179,97	86,41	**0,79**	43,08
14	T-16-02-09-075	-27,81	68,57	58,40	**-5,18**	39,87
15	T-14-02-09-09	-52,52	11,66	26,88	**-9,55**	22,00
16	T-16-02-1-06	16,10	170,39	66,76	**-2,66**	22,66
17	T-16-02-1-075	-25,56	73,15	43,00	**-2,60**	23,57
18	T-16-02-1-09	-50,98	14,02	22,73	**-7,64**	17,18
19	T-16-03-07-06	**-15,72**	109,94	52,53	-24,42	27,49
20	T-20-03-07-075	-41,42	54,46	52,81	**-13,12**	40,72
21	T-16-03-07-09	-61,25	**-2,66**	31,90	-21,15	28,57
22	T-16-03-09-06	**-1,03**	141,15	36,05	-13,18	4,42
23	T-14-03-09-075	-42,23	39,93	**4,21**	-21,29	-7,98
24	T-16-03-09-09	-58,01	1,98	4,85	-17,40	**0,82**
25	T-16-03-1-06	**-2,48**	134,22	23,98	-15,68	-8,81
26	T-16-03-1-075	-35,62	54,64	8,87	-13,01	**-5,93**
27	T-18-03-1-09	-52,86	7,63	5,35	-12,82	**0,58**

Table 5.8: Visualization of the best approximation of the plastic resistance using the Eurocode 3 method improved by incorporating the actual value of m obtained from the simulation.

The results presented in the Table 5.8 clearly indicate that the most accurate estimation of the plastic resistance is often obtained using the $F_{Rd,1}$ formulation for the T-stub. This method provides the best approximation particularly when the dimensionless parameter t_f/C is equal to 0,1 or 0,2, corresponding to cases where the T-stub exhibits high flexibility. In these configurations, where the flange deformation dominates over the bolt elongation, the predictions are significantly improved — with some discrepancies being nearly zero. Conversely, for cases with low T-stub flexibility, this method no longer offers reliable results. This highlights a strong correlation between the T-stub's relative flexibility and the accuracy of the plastic resistance evaluation.

These findings also underline the critical influence of the parameter m. When the value of m is not correctly estimated — as is the case in the standard Eurocode 3 formulation — it can lead to significant deviations in the predicted resistance. Updating this value based on simulation results significally improves the accuracy.

The Eurocode 3 with e_w improved

In the thesis of A. Neutelers **[2]**, an improved evaluation of the position of the equivalent bolt load is proposed. It is assumed that the stress distribution beneath the bolt head follows a triangular shape. Consequently, the value of e_w, initially defined as $d_w/4$ by Japsart **[5]**, is revised to $3 \cdot d_w/8$.

This modification influences only the calculation of $F_{Rd,1}$. Therefore, the Table 5.9 presents a comparison of the plastic resistance $F_{Rd,1}$ for both the base and the T-stub, using the two definitions of e_w.

In this Table 5.9, the **bold values** indicate cases where the modified definition of e_w leads to an improved approximation of the plastic resistance.

		Base		T-stub	
	Name	$e_w = d_w/4$ [%]	$e_w = 3 \cdot d_w/8$ [%]	$e_w = d_w/4$ [%]	$e_w = 3 \cdot d_w/8$ [%]
1	T-16-01-07-06	126,93	136,80	-18,31	**-14,75**
2	T-14-01-07-075	46,54	52,83	-17,57	**-14,03**
3	T-16-01-07-09	-3,58	**0,62**	-21,84	**-18,44**
4	T-16-01-09-06	146,80	156,33	-11,15	**-7,72**
5	T-14-01-09-075	52,22	57,97	-14,38	**-11,14**
6	T-18-01-09-09	3,68	6,46	-16,02	**-13,77**
7	T-18-01-1-06	145,87	152,20	-11,49	**-9,21**
8	T-16-01-1-075	58,13	63,96	-11,05	**-7,77**
9	T-20-01-1-09	14,94	19,98	-6,90	**-2,82**
10	T-16-02-07-06	107,07	120,88	-25,45	**-20,48**
11	T-12-02-07-075	25,38	33,17	-29,47	**-25,09**
12	T-12-02-07-09	-13,97	**-8,63**	-30,32	**-25,99**
13	T-16-02-09-06	132,02	145,05	-16,47	**-11,78**
14	T-16-02-09-075	51,41	59,92	-14,83	**-10,05**
15	T-14-02-09-09	-6,16	**-0,88**	-23,99	**-19,71**
16	T-16-02-1-06	124,83	136,66	-19,06	**-14,80**
17	T-16-02-1-075	46,14	53,83	-17,80	**-13,47**
18	T-16-02-1-09	-3,76	**1,30**	-22,05	**-17,95**
19	T-16-03-07-06	112,42	131,88	-23,53	**-16,52**
20	T-20-03-07-075	24,80	37,55	-29,80	**-22,63**
21	T-16-03-07-09	-6,83	**1,70**	-24,53	**-17,62**
22	T-16-03-09-06	121,07	137,60	-20,42	**-14,46**
23	T-14-03-09-075	37,14	47,53	-22,86	**-17,01**
24	T-16-03-09-09	-4,04	**3,14**	-22,27	**-16,46**
25	T-16-03-1-06	116,87	131,86	-21,93	**-16,53**
26	T-16-03-1-075	43,18	53,08	-19,46	**-13,89**
27	T-18-03-1-09	-6,85	**-2,61**	-24,55	**-21,11**

Table 5.9: Visualization of the best approximation of the plastic resistance using the Eurocode method improved with a better estimation of the parameter e_w proposed by Neutelers [**2**]

This straightforward modification clearly enables a more accurate approximation of the plastic resistance. The improvement is consistent across all evaluated cases for the T-stub. For the base, the enhancement is only observed when the original approximation was already reasonably close to the actual resistance. In cases where the initial estimation was significantly inaccurate, this adjustment tends to result in a less precise evaluation.

The improved model

The next step consists in evaluating the accuracy of the improved models proposed previously in Section 2.4. The Table 5.10 presents the three models: Zhao, Struik and De Back and Neutelers. It compares the difference between the actual plastic resistance and the approximations provided by each method.

As before, the smallest error in each row is highlighted **in bold**, in order to clearly identify which model offers the closest estimation to the real value.

	Name	Zhao [%]	Neutelers [%]	Struik and De Back [%]
1	T-16-01-07-06	24,69	**-8,02**	-29,22
2	T-14-01-07-075	25,34	**-6,05**	-28,00
3	T-16-01-07-09	19,29	**-11,96**	-32,28
4	T-16-01-09-06	36,11	**-3,12**	-23,05
5	T-14-01-09-075	30,72	**-5,84**	-25,13
6	T-18-01-09-09	28,01	**-10,19**	-26,56
7	T-18-01-1-06	35,04	**-6,78**	-22,70
8	T-16-01-1-075	36,43	**-4,06**	-22,97
9	T-20-01-1-09	44,13	**-0,42**	-21,78
10	T-16-02-07-06	11,97	**-9,30**	-35,29
11	T-12-02-07-075	**4,93**	-13,31	-38,37
12	T-12-02-07-09	**3,67**	-13,99	-39,11
13	T-16-02-09-06	18,06	**-3,64**	-27,55
14	T-16-02-09-075	20,38	**-1,32**	-26,13
15	T-14-02-09-09	**2,07**	-10,98	-33,81
16	T-16-02-1-06	**5,15**	-8,25	-29,82
17	T-16-02-1-075	6,79	**-6,44**	-28,72
18	T-16-02-1-09	**1,26**	-11,03	-32,41
19	T-16-03-07-06	**8,33**	-12,10	-33,49
20	T-20-03-07-075	**4,76**	-16,74	-39,79
21	T-16-03-07-09	**6,91**	-11,35	-34,37
22	T-16-03-09-06	**-6,66**	-13,25	-30,87
23	T-14-03-09-075	-14,85	**-13,79**	-33,11
24	T-16-03-09-09	**-8,84**	-13,63	-32,49
25	T-16-03-1-06	**-14,64**	-16,37	-32,22
26	T-16-03-1-075	**-11,94**	-12,80	-30,07
27	T-18-03-1-09	**-11,01**	-58,80	-32,42

Table 5.10: Visualisation of the best approximation of the plastic resistance using the improved models

At first glance, it is evident that the Struik and De Back method is never identified as the best-performing improved model compared to the other two.

In contrast, the Neutelers model consistently provides the most accurate approximation for T-stubs exhibiting high flexibility. On the other hand, the Zhao model proves to be more reliable for T-stubs with relatively low T-stub deflection compared to the bolt elongation.

Consequently, it would be of particular interest to compare these improved models with the Eurocode 3 formulations. This comparison would allow for a comprehensive evaluation of their predictive performance across varying geometric configurations and stiffness ratios.

Comparison

As previously explained, the Eurocode 3 remains the reference method for evaluating plastic resistance. Although the standard approach — taking the minimum value among the three failure modes — correctly identifies the governing mode as mode 1, which aligns with the results from the Abaqus simulations, it does not always provide the most accurate estimate of the actual plastic resistance.

This standard method, however, can be refined through adjustments to specific parameters that are frequently debated in the literature.

The Table 5.11 presents the differences between the calculated plastic resistance and the actual values, considering only the evaluation of $F_{Rd,1}$, while incorporating several key refinements:

- The first column represents the standard Eurocode 3 formulation.
- The second column applies the revised bolt load eccentricity $e_w = 3 \cdot d_w/8$, as suggested by Neutelers.
- The third column incorporates the actual value of m, as extracted from Abaqus simulation data.
- The fourth column combines both improvements (modified e_w and the real m).

This comparative analysis enables a clearer understanding of the individual and combined impacts of these refinements on the accuracy of the plastic resistance prediction.

	Name	Eurocode [%]	e_w improved [%]	m improved [%]	e_w and m improved [%]
1	T-16-01-07-06	-18,31	-14,75	**0,59**	**0,59**
2	T-14-01-07-075	-17,57	-14,03	**1,52**	**1,52**
3	T-16-01-07-09	-21,84	-18,44	**-1,61**	**-1,61**
4	T-16-01-09-06	-11,15	-7,72	**3,75**	**3,75**
5	T-14-01-09-075	-14,38	-11,14	**0,77**	**0,77**
6	T-18-01-09-09	-16,02	-13,77	**-5,16**	**-5,16**
7	T-18-01-1-06	-11,49	-9,21	**-2,34**	**-2,34**
8	T-16-01-1-075	-11,05	-7,77	**0,25**	**0,25**
9	T-20-01-1-09	-6,90	**-2,82**	5,01	5,01
10	T-16-02-07-06	-25,45	-20,48	**-5,00**	**-5,00**
11	T-12-02-07-075	-29,47	-25,09	**-22,85**	**-22,85**
12	T-12-02-07-09	-30,32	-25,99	**-21,38**	**-21,38**
13	T-16-02-09-06	-16,47	-11,78	**0,79**	**0,79**
14	T-16-02-09-075	-14,83	-10,05	**-5,18**	**-5,18**
15	T-14-02-09-09	-23,99	-19,71	**-9,55**	**-9,55**
16	T-16-02-1-06	-19,06	-14,80	**-2,66**	**-2,66**
17	T-16-02-1-075	-17,80	-13,47	**-2,60**	**-2,60**
18	T-16-02-1-09	-22,05	-17,95	**-7,64**	**-7,64**
19	T-16-03-07-06	-23,53	-16,52	**-24,42**	**-24,42**
20	T-20-03-07-075	-29,80	-22,63	**-13,12**	**-13,12**
21	T-16-03-07-09	-24,53	-17,62	**-21,15**	**-21,15**
22	T-16-03-09-06	-20,42	-14,46	**-13,18**	**-13,18**
23	T-14-03-09-075	-22,86	-17,01	**-21,29**	**-21,29**
24	T-16-03-09-09	-22,27	**-16,46**	-17,40	-17,40
25	T-16-03-1-06	-21,93	-16,53	**-15,68**	**-15,68**
26	T-16-03-1-075	-19,46	-13,89	**-13,01**	**-13,01**
27	T-18-03-1-09	-24,55	-21,11	**-12,82**	**-12,82**

Table 5.11: Comparison of the different variation for the calculation of $F_{Rd,1}$

As previously explained, both improvements positively impact the evaluation of the plastic resistance. However, correcting *the value of m has a more significant effect on the accuracy than modifying* e_w. Therefore, prioritizing the improvement of m leads better results.

Interestingly, *combining both improvements does not further enhance the approximation beyond what is achieved by improving m alone.*

Hence, it is clear that the most effective way to refine the Eurocode 3 evaluation is to use the actual value of m. However, obtaining this value can be resource-intensive, as it requires modelling

the specimen, performing simulations, and then measuring on the specimen itself. This process is time-consuming and somewhat redundant if the simulation already provides the real plastic resistance.

A more comprehensive study could be carried out to develop an accurate estimation method for the distance m without extensive simulations.

On the other hand, the adjustment of the equivalent bolt load position parameter e_w is straightforward to implement since it depends solely on geometric data. This improvement alone already leads to a better estimation and can be easily adopted in practice.

It is then possible to compare the improved models with the various evaluations used in the Eurocode 3 without the previously discussed enhancements.

As before, the best estimation in each case is highlighted **in bold**.

					Base		T-stub		
	Name	Zhao [%]	Neutelers [%]	Struik and De Back [%]	$F_{Rd,0}$ [%]	$F_{Rd,1}$ [%]	$F_{Rd,1}$ [%]	$F_{Rd,2}$ [%]	m improved [%]
1	T-16-01-07-06	24,69	-8,02	-29,22	5,18	126,93	-18,31	138,54	**0,59**
2	T-14-01-07-075	25,34	-6,05	-28,00	-32,03	46,54	-17,57	131,07	**1,52**
3	T-16-01-07-09	19,29	-11,96	-32,28	-55,31	-3,58	-21,84	128,22	**-1,61**
4	T-16-01-09-06	36,11	**-3,12**	-23,05	15,31	146,80	-11,15	81,68	3,75
5	T-14-01-09-075	30,72	-5,84	-25,13	-28,80	52,22	-14,38	69,25	**0,77**
6	T-18-01-09-09	28,01	-10,19	-26,56	-50,63	**3,68**	-16,02	80,03	-5,16
7	T-18-01-1-06	35,04	-6,78	-22,70	17,30	145,87	-11,49	63,91	**-2,34**
8	T-16-01-1-075	36,43	-4,06	-22,97	-25,91	58,13	-11,05	57,58	**0,25**
9	T-20-01-1-09	44,13	**-0,42**	-21,78	-46,69	14,94	-6,90	71,24	5,01
10	T-16-02-07-06	11,97	-9,30	-35,29	-7,39	107,07	-25,45	62,69	**-5,00**
11	T-12-02-07-075	**4,93**	-13,31	-38,37	-43,60	25,38	-29,47	35,20	-22,85
12	T-12-02-07-09	**3,67**	-13,99	-39,11	-61,31	-13,97	-30,32	33,58	-21,38
13	T-16-02-09-06	18,06	-3,64	-27,55	5,42	132,02	-16,47	33,31	**0,79**
14	T-16-02-09-075	20,38	**-1,32**	-26,13	-31,20	51,41	-14,83	35,93	-5,18
15	T-14-02-09-09	**2,07**	-10,98	-33,81	-57,38	-6,16	-23,99	14,93	-9,55
16	T-16-02-1-06	5,15	-8,25	-29,82	2,73	124,83	-19,06	13,86	**-2,66**
17	T-16-02-1-075	6,79	-6,44	-28,72	-33,23	46,14	-17,80	15,64	**-2,60**
18	T-16-02-1-09	**1,26**	-11,03	-32,41	-56,03	-3,76	-22,05	9,66	-7,64
19	T-16-03-07-06	8,33	-12,10	-33,49	**-8,32**	112,42	-23,53	32,46	-24,42
20	T-20-03-07-075	**4,76**	-16,74	-39,79	-46,78	24,80	-29,80	34,33	-13,12
21	T-16-03-07-09	6,91	-11,35	-34,37	-59,79	**-6,83**	-24,53	30,72	-21,15
22	T-16-03-09-06	-6,66	-13,25	-30,87	**-2,30**	121,07	-20,42	3,75	-13,18
23	T-14-03-09-075	-14,85	-13,79	-33,11	-39,51	37,14	-22,86	**-5,94**	-21,29
24	T-16-03-09-09	-8,84	-13,63	-32,49	-57,59	-4,04	-22,27	**1,32**	-17,40
25	T-16-03-1-06	-14,64	-16,37	-32,22	**-3,36**	116,87	-21,93	-9,24	-15,68
26	T-16-03-1-075	-11,94	-12,80	-30,07	-36,19	43,18	-19,46	**-6,37**	-13,01
27	T-18-03-1-09	-11,01	-58,80	-32,42	-57,01	-6,85	-24,55	**-4,34**	-12,82

Table 5.12: Visualisation of the best approximation of the plastic resistance with all the models

The Neutelers method provides a better estimation than the standard evaluation method. The Struik and De Back model is never the best approximation. The evaluation of the resistance for failure mode 0 of the base gives a good approximation when the base is relatively thick, while the resistance evaluation for mode 1 applied to the base is accurate when the base thickness is close to the one of the T-stub.

Despite these observations, *the standard Eurocode method using the real value of m remains the best option*, offering the closest estimation to the actual plastic resistance and correctly predicting the deformation mode. Moreover, when the error is slightly less accurate, it is negative, which means that the approximation underestimates the value and is therefore conservative.

Furthermore, *it is important to distinguish between specimens exhibiting coupled effects and those without, as this doesn't influence the evaluation of the plastic resistance.*

5.3 Conclusion

In this section, a parametric study was carried out based on 27 specimens using three dimensionless parameters: t_f/C, t_f/d_b and t_f/d_{plate}.

Each of these parameters was varied across three specific values. When only these parameters are altered, *a consistent comparison between the force-displacement curves becomes possible.* A logical evolution in the structural response is observed across these variations:

- An increase in t_f/C leads to both a higher plastic resistance and an increase in the slope of the pre-yielding region.
- An increase in t_f/d_b maintains a similar pre-yielding slope but results in an increase in plastic resistance.
- An increase in t_f/d_{plate} —indicating a more symmetric configuration — leads to a significant rise in *membrane effects*, thereby increasing testitthe ultimate resistance.

This parametric investigation has also suggested the existence of a new prying force configuration. Although not yet fully characterized, this configuration appears to *have no significant impact on the overall force-displacement curve, despite changes in the prying force location.*

Two critical assumptions from the Eurocode model were tested:

- *The stress distribution beneath the bolt head on the flange* aligns more closely with the triangular distribution proposed in the thesis by A. Neutelers **[2]**, rather than the uniform distribution assumed in the Eurocode 3.
- Conversely, *the stress distribution beneath the bolt head on the base* is consistent with the Eurocode's assumption of a uniformly distributed load.
- *The plastic hinge near the bolt* is accurately predicted at the bolt axis.
- However, *the hinge near the weld* is poorly predicted. The Eurocode 3 assumes it lies at 0,8 times h_f, while this parametric analysis shows it is located around 1,16 times h_f in this thesis. This misprediction significantly affects the determination of m.

The Eurocode 3 formulations and three improved models were applied to the parametric specimens to evaluate which method best approximates the actual plastic resistance. These comparisons lead to the following conclusions:

- The formulas $F_{Rd,0}$ and $F_{Rd,1}$ for the base yield accurate estimates in specific configurations.
- The resistance calculated using $F_{Rd,1}$ for the T-stub performs well in a limited number of cases and can be significantly improved by adopting $e_w = 3 \cdot d_w/8$, and further refined using the actual value of m.
- In all cases, the resistance $F_{Rd,1}$ applied to the T-stub consistently represents the minimum among the three calculated resistances.

- Nevertheless, this method becomes less relevant compared to the Neutelers model, which consistently provides better approximations. It's observed that the Struik and De Back model was not the most accurate among the options tested for the referenced configuration.
- Since determining the actual value of m requires extensive simulations, further studies could help establish a reliable estimation method for this critical parameter.

Traditionally, *T-stubs are studied under the assumptions of either a rigid base or symmetric configurations*. This thesis highlights the emergence of a new behavioural phenomenon: *coupled effects*. In this configuration, the thinner T-stub deforms following a mode 1 mechanism, while the thicker T-stub may deform either in mode 1 or mode 2. However, the parametric study did not reveal clear trends or consistent dependencies in the evaluation of plastic resistance related to the presence or absence of these coupled effects.

Chapter 6

Research perspectives

6.1 The coupled effect

Until now, existing literature has focused primarily on the study of simple T-stubs. All experimental investigations have been conducted either on rigid bases or under symmetric configurations.

However, these two configurations are rarely representative of the whole of real-world structural joints. In practice, it is restrictive to assume perfectly symmetric setups or cases where one of the T-stubs is significantly thicker than the other. To more accurately reflect realistic conditions and capture the true mechanical behaviour, *it is essential to examine the influence of base thickness variation.*

This thesis aims to explore the effects induced by varying the ratio between the flange thickness and the base thickness. Surprisingly, although such coupled effects have already been observed in prior studies, they have not been thoroughly investigated. During this research, traces of these effects were *identified in Faralli's experimental work* **[13]**, which was originally conducted on rigid bases.

(a) Specimen of the Faralli's study M20-5-15

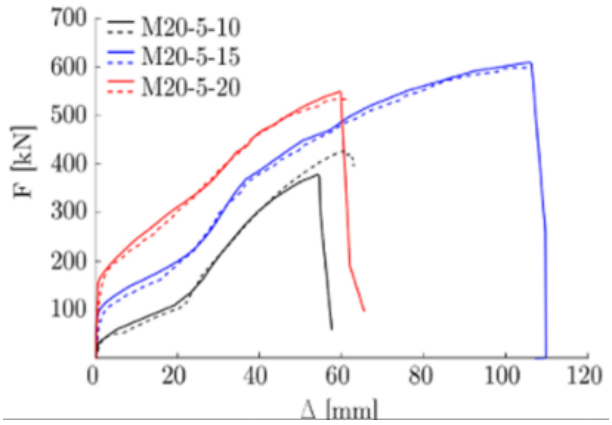

(b) Curve force-displacement corresponding to the specimen M20-5-15

Figure 6.1: Coupled effects ignored in the Faralli's study

No further analysis or discussion regarding this phenomenon is provided in the referenced article **[13]**. *It is plausible that the authors of the experimental study considered this particular specimen to be an outlier or testing error*, leading to its exclusion from the main analysis.

However, with a renewed perspective, this specimen now appears to be the most relevant and intriguing case in the study. The article includes complete data and provides the force-displacement curve of this specific specimen, which clearly exhibits coupled effects.

In the Figure 6.1b, the behaviour of this specimen is represented by the blue curve, while the black and red curves correspond to two other similar specimens tested with a rigid base.

Although the ultimate resistance of the specimen (M20-5-15) is only marginally higher than that of the red curve specimen, the key observation lies in *its displacement capacity*. The specimen affected by coupled effects demonstrates a significantly greater displacement before failure, almost twice that of its rigid-base counterpart. This indicates that *the presence of coupled effects introduces a substantial ductility reserve*, which could be considered exceptional.

This ductility reserve may offer both benefits and drawbacks. From a structural robustness perspective, it is highly advantageous, allowing the joint to undergo *large deformations before collapse*. However, such high deformations could also present challenges in terms of serviceability and post-event reusability of the connection. This makes it crucial to account for these behaviours early in the design process.

Further investigations are required to assess the magnitude and implications of these deformations, and to develop reliable methods to predict and quantify them.

Chapter 7

Conclusions

In conclusion, **robustness** remains a central challenge in the field of structural engineering. It is essential to maximize the time during which a structure can maintain its stability in the event of extreme loading, thereby allowing for safe evacuation. Two main strategies have been proposed to achieve this: the development of **membrane effects** and the enhancement of **ductility reserves** within structural joints.

This thesis is fully aligned with this challenge, aiming to deepen the understanding of T-stub behaviour by building upon existing models and experimental studies. Unlike most works in the literature, which typically focus on symmetrical T-stubs or those connected to rigid bases, this study explores T-stub joints with varied thickness combinations — a configuration rarely addressed — thereby offering a more realistic and comprehensive perspective.

A second major challenge in steel construction is the potential for **structural reuse**. Significant efforts are currently being made to revolutionize construction practices in order to reduce environmental impact. Achieving this goal requires a precise understanding of joint behaviour under various loading conditions.

With this objective, the study aims to model, analyse, and compare the behaviour of various joint configurations. To achieve this, several analytical models have been considered and applied. The **Eurocode 3**, which serves as the standard reference model, was evaluated alongside **three improved models** available in the literature. These models exhibit fundamental differences in their formulation and assumptions. Additionally, minor modifications to the Eurocode 3 were proposed and analysed, with the goal of enhancing the accuracy of plastic resistance predictions.

To validate the methodology employed in this thesis, selected experimental campaigns were analysed, and specific specimens were modelled using **the nonlinear finite element software Abaqus**. The modelling was carried out independently, with a focus on understanding and calibrating the parameters within the tool Abaqus. Significant effort was dedicated to controlling the modelling of components, defining appropriate boundary conditions, assessing mesh sensitivity, and implementing strategies to ensure proper convergence of the simulations.

The comparison between simulation results and experimental data confirmed that Abaqus simulation can reliably reproduce the mechanical behaviour of the specimens, thereby validating its use for further analysis.

This validation enabled the implementation of **a parametric study involving 27 specimens**, in which **three dimensionless parameters** were systematically varied. The first parameter represents **the ratio between the flexibility of the T-stub and that of the bolt**. The second corresponds to **the ratio of the T-stub flange thickness to the bolt diameter**. The third represents **the ratio between the flange thickness and the base plate thickness**.

The selection of the 27 specimens and the definition of the dimensionless parameters were based on a personal reflection aimed at maximising the relevance of the results and ensuring meaningful comparisons. The study follows a rigorous methodology in the organisation of simulations and the

interpretation of results.

The finite element modelling was carried out based on a **series of assumptions**, particularly regarding the material's constitutive laws and the points of result extraction. Specific constraints were imposed to ensure consistency across simulations. For example, the mesh size was standardized across all models, and the width of the T-stub was fixed at 90 mm to maintain the behaviour characteristic of **a short T-stub** and avoid the emergence of different effective lengths. Furthermore, the distance between the bolt axis and the plate edge was fixed at 50 mm to eliminate the influence of edge effects caused by too short a distance between the bolt hole and the edge.

Additionally, nine supplementary specimens were modelled to investigate particular behaviours in greater details. These models introduced a fourth dimensionless parameter, defined as **the ratio between the distance from the weld to the bolt axis and the distance from the bolt axis to the plate edge**. This allows for an analysis of the influence of edge distance variations.

It is important to note that, due to the limited availability of detailed material properties, especially regarding the constitutive behaviour beyond yielding, **the simulation results cannot be used to draw definitive conclusions about ultimate resistance and displacements**.

Thanks to the rigorous structuring of the analysed cases, this parametric study allows for the identification of essential trends and the formulation of critical observations regarding the behaviour of T-stub connections. It has notably been used to re-examine certain **key parameters** of the standard method from a constructive perspective. **The prying force** location assumed in the Eurocode 3 provides a reasonable approximation; however, an alternative configuration may also be characterized. Nevertheless, variations in the prying force position or in the lever arm length e do not significantly affect the force–displacement response.

Regarding **the stress distribution beneath the bolt head**, the Eurocode 3 (later refined by professor Jaspart) assumes a uniform distribution, while the thesis by A. Neutelers proposes a triangular distribution. The present study highlights the necessity of distinguishing between the T-stub and the base—an aspect that is rarely addressed in detail by existing models. This distinction emerges from a critical analysis of the simulation results.

Based on the simulations carried out in Abaqus (whose implementation required an initial learning phase and the resolution of several technical challenges), it was concluded that the stress distribution beneath the bolt head is relatively uniform on the base plate, while it exhibits a triangular pattern on the T-stub side.

Another important consideration is the Eurocode's prediction of **plastic hinge locations**. The assumption that a hinge forms at the bolt axis is generally accurate, except in cases where the T-stub is highly flexible. In contrast, the Eurocode's assumption of a hinge forming near the weld often proves inaccurate, leading to errors in the calculated plastic resistance.

To predict the behaviour of a T-stub, it has been demonstrated that the position of the bolt within the bolt hole has a significant influence, particularly near the ultimate state. However, this parameter is not considered in the current formulation of the Eurocode 3.

In the Eurocode 3, **the plastic resistance** is taken as the minimum among the three failure modes. In the studied cases, mode 1 consistently governs, which aligns with the actual failure behaviour. However, the associated resistance value is not always the best approximation of the true plastic capacity.

The Zhao model tends to yield accurate results, except when the T-stub is highly flexible. In such cases, the resistance $F_{Rd,1}$ applied to the T-stub can be significantly improved using Neutelers model or by adjusting the lever arm length e_w as proposed in Neutelers thesis. Another way to enhance the Eurocode's predictive accuracy is by incorporating the actual value of the shape factor m. However, determining this real value currently requires a substantial amount of computational effort.

This thesis has also highlighted a new type of behaviour referred to as **coupled effects**. This behaviour, in which the two T-stubs deform in different modes, has been rarely studied so far, although it appears to more closely represent realistic structural conditions. While the presence or absence of coupled effects seems to have little impact on the calculated plastic resistance, observations from a specific case in Faralli's study suggest that these effects could influence the ultimate behaviour. In particular, they appear to offer slightly higher ultimate resistance and, more importantly, **an exceptional reserve of ductility**.

This phenomenon presents both **opportunities and challenges**. On one hand, the increased ductility could significantly enhance the robustness of structures during extreme events. On the other hand, such large deformations may pose serious difficulties in terms of structural reusability. The insights gained, particularly regarding coupled effects and improved evaluation methods, underline the substantial potential for further investigation and development in the domain of joint behaviour and structural robustness.

Beyond the technical knowledge acquired, this thesis has enabled me to develop as a research engineer by fostering a critical mindset towards existing models and the ability to implement a rigorous scientific approach. Focusing on a topic that is regularly studied but still underexplored in the literature has given me the opportunity to make an original contribution, particularly in analysing coupled effects and highlighting the limitations of the assumptions in Eurocode 3.

The progress of this thesis benefited from regular discussions with a supervisor and a doctoral researcher specializing in the field. These exchanges provided valuable critical feedback. This collaborative environment also helped me develop essential technical communication skills for a professional setting.

In conclusion, this thesis offers a modest contribution to a broad and complex field of research and may serve as a foundation for the further development of studies on coupled effects.

Bibliography

[1] Warnant, A., *Contribution à l'étude des assemblages de construction métallique sous charges exceptionnelles*, University of Liège, Liège, Belgium, 2010.

[2] Neutelers, A. *Improvement of the mechanical model for mode 1 T-stub plastic strength*, University of Liège, Liège, Belgium, 2023.

[3] Jaspart, J.-P. and Demonceau, J.-F., *Assemblages structuraux*, European comittee for standardization, Liège, 2023.

[4] CEN, EN, *Eurocode 3 : Design of Steel Structures-Part 1-8 : Design of joints*, European comittee for standardization, Brussels, 2005.

[5] Jaspart, J.-P. and K.Weynand, K., *Design of joints in steel and composite structures*, University of Liège, Liège, Belgium, 2016

[6] Zoetemijer, P.,*A design method for the tension side of statically loaded, bolted beam-to-column connections*, HERON, 1974.

[7] Lyu and al., *Mechanical model for the full range behaviour of bolted T-stubs*, Tongji University, China, 2023

[8] Piluso and al, *Ultimate behavior of bolted T-stubs. I : Theoritical model*, p. 686-693, No 6, Journal of structural engineering, American Society of Civil Engineers, 2001

[9] Piluso and al, *Ultimate behavior of bolted T-stubs. II : Model validation*, p. 694-704, No 6, Journal of structural engineering, American Society of Civil Engineers, 2001

[10] Swanson, J.A., *Ultimate strength prying models for bolted T-stub connections*, 2002

[11] Tartaglia and al., *Experimental and numerical study on the T-stub behaviour with preloaded bolts under large deformation* , University of Naples, Naples, Italie, 2020.

[12] Bezerra and al., *Behavior of T-stub steel connections bolted to rigid bases*, University of Brasìlia, Brazil, 2022

[13] Faralli and al, *Experimental investigation and modelling of T-stubs undergoing large displacements*, University College London, London, United Kingdom

[14] Khani and al., *Nonlinear response of coupled and tied-to-rigid base T-stub T-stub connections*, University of Tabriz, Tabriz, Iran, 2024

[15] Özkiliç, Y.O.,*The capacities of unstiffened T-stubs with thin plates and large bolts*, Necmettin Erbakan University, Konya, Turkey, 2021

[16] CEN, EN, *Eurocode 3 : Design of steel structures-Part 1-8 : Design assisted by finite element anaysis*, European comittee for standardization, Brussels, 2021, page 19-23.

[17] Neutelers, A., *Tutorial 0: basic commands in Abaqus*, ABAQUS© TUTORIAL, Basic commands, 2023

[18] FATOR, General Catalogue

List of Figures

List of Tables

Appendix

A The application of the models on the experimental specimen T-S-HR-8

In sections 2.3 and 2.4, several models are considered. The most prominent is the Eurocode 3, which is the current official and most widely used standard. In addition, three alternative models have been developed to identify the most suitable approach. As a preliminary analysis, the three Eurocode models is applied to the two primary specimens selected.

To facilitate understanding of the development, the models is applied to specimen T-S-HR-8, and the methodology may be extended to specimen T-S-HR-20.All the information are presented here below.

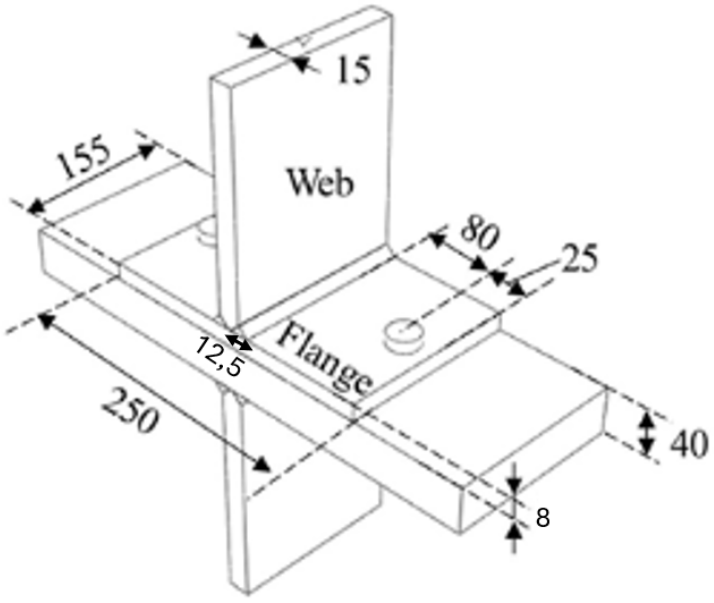

Figure 1: Geometry of the specimen T-S-HR-8

d_w [mm]	l_w [mm]	A_s [mm^2]	l_{head} [mm]	l_{nut} [mm]	$f_{u,b}$ [MPa]	$f_{y,b}$ [MPa]	$\epsilon_{u,b}$ [-]	$\epsilon_{y,b}$ [-]	E_b [MPa]
30	4	156,82	10	13	1 143	1 001	0,044	0,0069	143 024

Table 1: Bolt's information

E [MPa]	f_y [MPa]	f_u [MPa]	ϵ_u [-]
208 247	369	858	0,28

Table 2: Informations for the material's constitutive laws for the flange

A.1 Application of the Eurocode

All the data required to apply the Eurocode model are summarized in Figure 1 and Tables 1 and 2. Additional geometrical parameters are also necessary and are summarized below:

$$e_{min} = e = 25\text{mm}$$
$$m = \frac{B-t_w}{2} - e - 0,8 \cdot h_f = \frac{250-15}{2} - 25 - 0,8 \cdot 12,5 = 82,5\text{mm}$$
$$n = min(e; 1,25 \cdot m) = min(25; 100) = 25\text{mm}$$
$$e_w = \frac{d_w}{4} = 7,5\text{mm}$$

As explained in section 2.2.2, the determination of this length—required for further use in the model—has been the subject of considerable discussion. Therefore, as a starting point, the three main possible values for the effective length are compared. Furthermore, since the specimen is considered short according to the study, the expected yield line pattern should be linear.

$$l_{eff,cp} = 2 \cdot \pi \cdot m = 518,363\text{mm}$$
$$l_{eff,nc1} = 4 \cdot m + 1,25 \cdot e = 361,25\text{mm}$$
$$l_{eff,nc2} = L = 155\text{mm}$$

These possibilities allow the determination of the effective length for both failure mode 1 and failure mode 2, based on the minimum length among the potential yield line patterns that corresponds to the mechanism that minimises the required energy.

$$l_{eff,1} = min(l_{eff,cp}; l_{eff,nc1}; l_{eff,nc2}) = 155\text{mm}$$
$$l_{eff,2} = min(l_{eff,nc1}; l_{eff,nc2}) = 155\text{mm}$$

A preliminary verification is required to ensure the correct use of the table provided by the Eurocode 3. The bolt elongation length, denoted as L_b, must be compared to a reference parameter L_b^*. If $L_b \leq L_b^*$, prying forces may occur.

$$L_b = 2 \cdot l_{washer} + t_f + d_{plate} + \frac{l_{head}+l_{nut}}{2} = 2 \cdot 4 + 8 + 40 + \frac{10+13}{2} = 67,5\text{mm}$$
$$L_b^* = \frac{8,8 \cdot m^3 \cdot A_s \cdot n_b}{l_{eff} \cdot t_f^3} = \frac{8,8 \cdot 82,5^3 \cdot 156,82 \cdot 1}{155 \cdot 8^3} = 9\,764,89\text{mm} > L_b$$

This condition is satisfied; therefore, prying forces are indeed present.

Now that all additional geometrical parameters have been determined, the calculation of the bending moment for failure modes 1 and 2, using effective lengths 1 and 2 respectively, becomes straightforward. With this, the ultimate resistance of the bolt is also determined, enabling the straightforward application of the three formulas developed in section 2.3.

$$B_{T,Rd} = 0,9 \cdot f_{ub} \cdot A_s = 0,9 \cdot 1\,143 \cdot 156,82 = 161\,329\text{N}$$
$$M_{pl,1,Rd} = 0,25 \cdot l_{eff} \cdot t_f^2 \cdot f_y = 0,25 \cdot 155 \cdot 8^2 \cdot 369 = 915\,120\text{Nmm}$$
$$M_{pl,2,Rd} = M_{pl,1,Rd} = 915\,120\text{Nmm}$$

In this case, $M_{pl,2,Rd} = M_{pl,1,Rd}$ because $l_{eff,1} = l_{eff,2}$

The formulas can then be readily applied to identify the governing failure mode. Indeed, the failure mode corresponding to the lowest resistance governs the behaviour. As previously explained, there are two methods to calculate $F_{T,1,Rd}$; however, it has been demonstrated that the second method provides improved accuracy, and thus only this approach is developed here.

$$F_{T,1,Rd} = \frac{(8 \cdot n - 2 \cdot e_w) \cdot M_{pl,1,Rd}}{2 \cdot m \cdot n - e_w \cdot (m+n)} = \frac{(8 \cdot 25 - 2 \cdot 7,5) \cdot 915\,120}{2 \cdot 82,5 \cdot 25 - 7,5 \cdot (82,5+25)} = 51\,012,34\text{N}$$
$$F_{T,2,Rd} = \frac{2 \cdot M_{pl,2,Rd} + 2 \cdot B_{T,Rd} \cdot n}{m+n} = \frac{2 \cdot 915\,120 + 2 \cdot 161\,539 \cdot 25}{82,5+25} = 92\,062,36\text{N}$$
$$F_{T,3,Rd} = 2 \cdot B_{T,Rd} = 2 \cdot 161\,539 = 322\,658,56$$

$$F_{T,Rd} = min(F_{T,1,Rd}; F_{T,2,Rd}; F_{T,3,Rd}) = 51\,012,34\text{N} = 51,012\text{kN}$$

Therefore, the governing failure mode for this specimen is mode 1, involving four yield lines.

Now that the failure mode and its corresponding resistance have been identified, it is possible to determine the stiffness of the specimen in order to construct the load–displacement curve. To achieve this, the stiffness of each sub-component is evaluated individually.

$$k_{base} = \frac{0{,}9 \cdot l_{eff} \cdot d_{plate}^3}{m^3} = \frac{0{,}9 \cdot 155 \cdot 40^3}{82{,}5^3} = 15,89mm$$
$$k_{plate} = \frac{0{,}9 \cdot l_{eff} \cdot t_f^3}{m^3} = \frac{0{,}9 \cdot 155 \cdot 8^3}{82{,}5^3} = 0,1272mm$$
$$k_{bolt} = \frac{1{,}6 \cdot A_s}{L_b} = \frac{1{,}6 \cdot 156{,}82}{67{,}5} = 3,72\text{mm}$$

The stiffness of the assembly can be calculated from the stiffnesses of these three sub-components and is given by:

$$k_{eff} = \frac{1}{\sum \frac{1}{k_i}} = \frac{1}{\frac{1}{k_{base}} + \frac{1}{k_{plate}} + \frac{1}{k_{bolt}}} = \frac{1}{\frac{1}{15{,}89} + \frac{1}{0{,}1272} + \frac{1}{3{,}72}} = 0,122\text{mm}$$

The last step permits to build the $\Delta - F$ curve. Two options are possible and is presented the bilinear curve and the trilinear curve.

$F_0 = 0\text{kN}$	$F_1 = 51,01\text{kN}$	$F_2 = 51,01\text{kN}$
$\Delta_0 = 0\text{mm}$	$\Delta_1 = \frac{F_1}{E \cdot k_{eff}} = \frac{51{,}01}{208{,}247 \cdot 0{,}121} = 2,01\text{mm}$	$\Delta_2 = +\infty$

$F_0 = 0\text{kN}$	$F_1 = \frac{2 \cdot F_{T,Rd}}{3} = 34,01\text{kN}$	$F_2 = 51,01\text{kN}$	$F_3 = 51,01\text{kN}$
$\Delta_0 = 0\text{mm}$	$\Delta_1 = \frac{F_1}{E \cdot k_{eff}} = \frac{34}{208{,}247 \cdot 0{,}121} = 1,33\text{mm}$	$\Delta_2 = \frac{F_2}{E \cdot \frac{k_{eff}}{3}} = 6,021\text{mm}$	$\Delta_3 = +\infty$

This table, along with these values, leads to the following two specific curves.

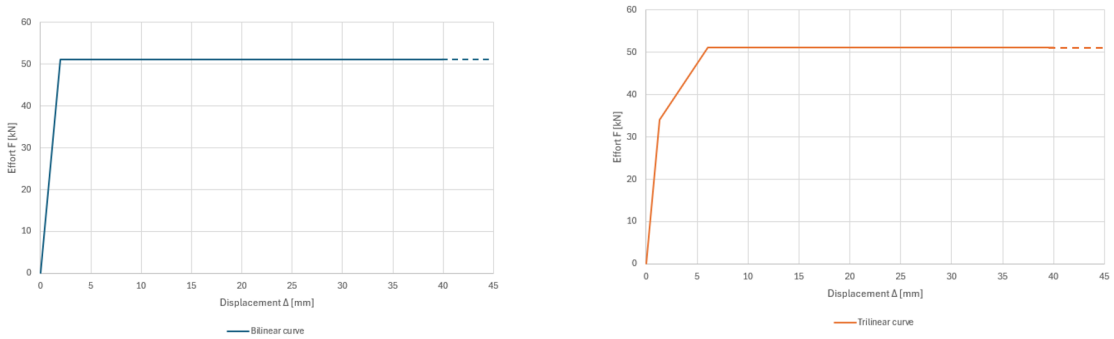

(a) The bilinear curve

(b) The trilinear curve

Figure 2: Curves with the Eurocode model for the T-stub T-S-HR-8

A.2 Application of the Zhao model

As explained in Section 2.4.1, the Zhao model is an enhancement of the Piluso model. One of the improvement of this method is that it allows to calculate some points of the curve. Here, the development is done for four different points for the flange shown with four letters. "y" corresponds at the end of the elastic part, "h" is the end of the plastic plateau, "m" is an intermediate point obtain with the ϵ_u of engineer form of the flange and u is for the ultimate point. Only two points are used for the bolt : "y" that corresponds to the end of the elastic part and "u" for the ultimate behaviour.

One of the key improvements of this method is that it enables the calculation of specific points along the stress–strain curve. In this development, four characteristic points are considered for the flange, each denoted by a letter:

- "y" corresponds to the yielding,

- "h" marks the end of the plastic plateau,
- "m" is an intermediate point defined using the engineering ultimate strain $\epsilon_u$of the flange,
- "u" represents the ultimate point.

For the bolt, only two points are considered:

- "y", corresponding to the yielding,
- "u", representing the ultimate behaviour.

The first step involves obtaining and converting all relevant data from the materials' constitutive laws, transforming them from engineering stress–strain to true stress–true strain representation.

$$\epsilon_y = \frac{f_y}{E} = \frac{369}{208\,247} = 0,0017[-]$$
$$\epsilon_{m,true} = ln(1+\epsilon_u) = ln(1+0,28) = 0,2468[-]$$
$$f_{m,true} = f_u \cdot (1+\epsilon_u) = 858 \cdot (1+0,28) = 1\,098,24\text{MPa}$$
$$\epsilon_h = 0,015 = 1,5\%$$

This value is not provided, so an assumption has been made, as explained in Section 3.2.1.

$$\epsilon_{h,true} = ln(1+\epsilon_h) = ln(1+0,0037) = 0,0148[-]$$
$$E_{h,true} = \frac{f_{m,true}-f_y}{\epsilon_{m,true}-\epsilon_{h,true}} = \frac{1\,098,24-369}{0,2468-0,0148} = 3\,143,662\text{MPa}$$

In the article, E_u and $\epsilon_{u,true}$ are not given. These values are typically taken between $E_u \in [200;600]$ and $\epsilon_{u,true} \in [0,;0,25]$.

To determine which values to select, the Zhao model was applied to multiple combinations of E_u and $\epsilon_{u,true}$. After evaluating approximately ten combinations, it was observed that the variation in these parameters had a negligible impact on the results.

Let choose $E_u = 400\text{MPa}$ and $\epsilon_{u,true} = 0,25[-]$

To initiate the model, the moment-curvature relationship for the steel is established.

$$\chi_y = \frac{2\cdot\epsilon_y}{t_f} = 0,0004\text{rad/mm}$$
$$\chi_h = \frac{2\cdot\epsilon_h}{t_f} = 0,0037\text{rad/mm}$$
$$\chi_m = \frac{2\cdot\epsilon_m}{t_f} = 0,0617\text{rad/mm}$$
$$\chi_u = \frac{2\cdot\epsilon_u}{t_f} = 0,0625\text{rad/mm}$$

Piluso developed a method to determine all bending moments based on the ratio between the moment at a point and the bending moment at yielding, which is calculated using the previously established moment-curvature relationships for the steel.

$$\frac{M_h}{M_y} = \frac{1}{2}\cdot\left(3-\left(\frac{\chi_y}{\chi_h}\right)^2\right) = 1,492$$

$$\frac{M_m}{M_y} = \frac{1}{2}\cdot\left(3-\left(\frac{\chi_y}{\chi_m}\right)^2\right) + \frac{1}{2}\cdot\frac{E_{h,true}}{E}\cdot\left(\frac{\chi_m-\chi_h}{\chi_y}\right)\cdot\left(1-\frac{\chi_h}{\chi_m}\right)\cdot\left(2+\frac{\chi_h}{\chi_m}\right) = 3,413$$

$$\frac{M_u}{M_y} = \frac{1}{2}\cdot\left(3-\left(\frac{\chi_y}{\chi_u}\right)^2\right) + \frac{1}{2}\cdot\frac{E_{h,true}}{E}\cdot\left(\frac{\chi_u-\chi_h}{\chi_y}\right)\cdot\left(1-\frac{\chi_h}{\chi_u}\right)\cdot\left(2+\frac{\chi_h}{\chi_u}\right)$$
$$-\frac{1}{2}\cdot\frac{E_{h,true}-E_{u,true}}{E}\cdot\left(\frac{\chi_u-\chi_m}{\chi_y}\right)\cdot\left(1-\frac{\chi_m}{\chi_u}\right)\cdot\left(2+\frac{\chi_m}{\chi_u}\right) = 3,439$$

Knowing l_{eff}, the bending moment at yielding can be determined. With this information, the bending moments at the various points of interest can be calculated.

$$M_y = \frac{l_{eff} \cdot t_f^2 \cdot f_y}{6} = 610\,080\text{Nmm}$$
$$M_h = \frac{M_h}{M_y} \cdot M_y = 910\,799,4\text{Nmm}$$
$$M_m = \frac{M_m}{M_y} \cdot M_y = 2\,082\,230\text{Nmm}$$
$$M_u = \frac{M_u}{M_y} \cdot M_y = 2\,098\,279\text{Nmm}$$

It is now possible to determine the failure mode of the specimen. Remember that the Zhao model proposes four failure modes. Modes 2 and 3 correspond exactly to those defined in the Eurocode 3. Mode 1 is further subdivided into two possibilities: FM-1-FF, where failure occurs in the flange, and FM-1-BR, where failure is due to bolt failure.

$$\lambda = \frac{n}{m} = \frac{25}{82{,}5} = 0,303$$
$$\zeta = \frac{M_h}{M_u} = \frac{910\,799{,}4}{2\,098\,279} = 0,434$$
$$c = 1 - \frac{d_w}{8 \cdot m} \cdot \frac{1+\lambda}{\lambda} = 0,8045$$
$$a = \frac{1 - \frac{d_w}{8 \cdot m} \cdot \frac{1+\lambda}{\lambda} + \frac{d_w}{8 \cdot m} \cdot \frac{1+2 \cdot \lambda}{\lambda \cdot \zeta}}{\frac{1+2 \cdot \lambda}{\lambda \cdot \zeta} - (1 - \frac{d_w}{8 \cdot m} \cdot \frac{1+\lambda}{\lambda})} = 0,1192$$
$$b = \frac{2 \cdot (1 + \frac{d_w}{8 \cdot m}) \cdot (1 - \frac{d_w}{8 \cdot m} \cdot \frac{1+\lambda}{\lambda})}{1 - \frac{d_w}{8 \cdot m} \cdot \frac{1+\lambda}{\lambda} + \frac{1+2 \cdot \lambda}{\lambda \cdot \zeta}} = 1,2373$$
$$\beta_2 = \frac{-(\frac{1+\lambda}{\lambda} + 2 \cdot \lambda) + \sqrt{(\frac{1+\lambda}{\lambda} \cdot b - 2 \cdot c)^2 + \frac{8 \cdot c \cdot b}{a}}}{2 \cdot (\frac{1}{a} - \frac{1+\lambda}{\lambda})} = 0,375$$
$$\frac{2 \cdot \lambda \cdot \zeta}{1+2 \cdot \lambda} \cdot c = 0,1638 \cdot 0,8045 = 0,1317$$

All these parameters allow the definition of intervals corresponding to each failure mode.

FM-1-FF : $\beta \in [0; 0,1317]$
FM-1-BR : $\beta \in]0,1317; 0,3751]$
FM-2 : $\beta \in]0,3751; 2]$
FM-3 : $\beta \in]2; +\infty[$

The value of β can now be compared against all the intervals to determine the appropriate failure mode.

$$B_{u,Rd} = A_s \cdot f_{u,b} = 156,83 \cdot 1\,143 = 179\,257,8\text{N}$$
$$\beta = \frac{2 \cdot M_h}{m \cdot B_{u,Rd}} = 0,123$$

The parameter β falls within the interval [0;0,1317]; therefore, the failure mode corresponds to flange failure (FM-1-FF). In this case, $\psi = 1$.

The value of ψ depends on the corresponding interval. For example, for the second specimen analysed, T-S-HR-20, the method identifies failure mode 2. In this case, ψ is calculated as follows:

$$\psi = a \cdot \frac{(b - \beta)}{\beta}$$

The expected ultimate resistance should be close to:

$$F_{u-1-FF} = \frac{(32 \cdot n - 2 \cdot d_w) \cdot M_u}{(8 \cdot m \cdot n - (m+n) \cdot d_w)} = 116\,966,2\text{N}$$

To further evaluate the behaviour of the flange, the plastic rotations at the hinge are assessed.

$$C_h = \frac{\chi_h^3}{2 \cdot \chi_h \cdot \chi_y} - \frac{(\chi_h - \chi_y)^3}{2 \cdot \chi_h \cdot \chi_y} = 0,004945\text{rad/mm}$$
$$C_m = \frac{\chi_m^3}{2 \cdot \chi_m \cdot \chi_y} - \frac{(\chi_m - \chi_y)^3}{2 \cdot \chi_m \cdot \chi_y} + \frac{E_h \cdot (\chi_m - \chi_h)^3}{2 \cdot E \cdot \chi_m \cdot \chi_y} = 0,1457\text{rad/mm}$$
$$C_u = \frac{\chi_u^3}{2 \cdot \chi_u \cdot \chi_y} - \frac{(\chi_u - \chi_y)^3}{2 \cdot \chi_u \cdot \chi_y} + \frac{E_h \cdot (\chi_u - \chi_h)^3}{2 \cdot E \cdot \chi_u \cdot \chi_y} - \frac{(E_h - E_u) \cdot (\chi_u - \chi_m)^3}{2 \cdot E \cdot \chi_u \cdot \chi_y} = 0,1484\text{rad/mm}$$

$$\theta_{h,p} = \frac{m}{1+\psi} \cdot (\chi_h - \frac{M_y}{M_h} \cdot C_h - \frac{1}{2} \cdot \chi_y \cdot \frac{M_h}{M_y}) = 0,003263\text{rad}$$
$$\theta_{m,p} = \frac{m}{1+\psi} \cdot (\chi_m - \frac{M_y}{M_m} \cdot C_m - \frac{1}{2} \cdot \chi_y \cdot \frac{M_m}{M_y}) = 0,7529\text{rad}$$
$$\theta_{u,p} = \frac{m}{1+\psi} \cdot (\chi_u - \frac{M_y}{M_u} \cdot C_u - \frac{1}{2} \cdot \chi_y \cdot \frac{M_u}{M_y}) = 0,7662\text{rad}$$

For each selected point, the resistance force can now be calculated. In this thesis, the Zhao method has been extended using the second method from the Eurocode 3 to determine the resistance associated with failure mode 1. To do so, a parameter has been calculated and is used in the determination of the resistance:

$$\mu = \frac{(1+\psi)-\frac{d_w}{8 \cdot m}}{1-\frac{d_w}{8 \cdot m} \cdot \frac{1+\lambda}{\lambda}} = 2,429$$
$$F_y = \frac{2 \cdot M_y}{m} \cdot \mu = 35,93\text{kN}$$
$$F_h = \frac{2 \cdot M_h}{m} \cdot \mu = 53,64\text{kN}$$
$$F_m = \frac{2 \cdot M_m}{m} \cdot \mu = 168,06\text{kN}$$
$$F_u = \frac{2 \cdot M_u}{m} \cdot \mu = 171,52\text{kN}$$

The next step is to determine the displacements at the various points. To do so, the total displacement is considered as the sum of the elastic and plastic components. First, the elastic displacement is calculated as follows:

$$\Delta_{y,e} = \frac{1,18 \cdot m^3 \cdot F_y}{E \cdot l_{eff} \cdot t_f^3} = 1,44\text{mm}$$
$$\Delta_{h,e} = \frac{1,18 \cdot m^3 \cdot F_h}{E \cdot l_{eff} \cdot t_f^3} = 2,15\text{mm}$$
$$\Delta_{m,e} = \frac{1,18 \cdot m^3 \cdot F_m}{E \cdot l_{eff} \cdot t_f^3} = 6,74\text{mm}$$
$$\Delta_{u,e} = \frac{1,18 \cdot m^3 \cdot F_u}{E \cdot l_{eff} \cdot t_f^3} = 6,87\text{mm}$$

Then, the contribution of the plastic component is evaluated.

$$\Delta_{y,p} = 0\text{mm}$$
$$\Delta_{h,p} = m \cdot sin(\theta_{h,p}) = 0,269\text{mm}$$
$$\Delta_{m,p} = m \cdot sin(\theta_{m,p}) = 56,41\text{mm}$$
$$\Delta_{u,p} = m \cdot sin(\theta_{u,p}) = 57,21\text{mm}$$

The two components can then be added to obtain the total displacement.

$$\Delta_y = \Delta_{y,e} + \Delta_{y,p} = 1,44\text{mm}$$
$$\Delta_h = \Delta_{h,e} + \Delta_{h,p} = 2,42\text{mm}$$
$$\Delta_m = \Delta_{m,e} + \Delta_{m,p} = 63,15\text{mm}$$
$$\Delta_u = \Delta_{u,e} + \Delta_{u,p} = 64,09\text{mm}$$

Using these forces and displacements, the force–displacement curve of the plate can be constructed.

A similar methodology is applied to develop the force–displacement curve for the bolt. As previously explained, only two points on the bolt's curve is analysed due to the limited availability of data.

$$\alpha = \frac{2 \cdot \lambda \cdot (1+\psi)}{\lambda \cdot (1+\lambda) \cdot \psi} = 0,7547$$
$$F_{y,b} = \alpha \cdot A_s \cdot f_{y,b} = 118,63\text{kN}$$
$$F_{u,b} = \alpha \cdot A_s \cdot f_{u,b} = 135,46\text{kN}$$

Then the displacements for the bot at the two studied points can be calculated.

$$\Delta_{y,b} = L_b \cdot \epsilon_{y,b} = 0,472\text{mm}$$
$$\Delta_{u,b} = L_b \cdot \epsilon_{u,b} = 2,97\text{mm}$$

To construct the complete force–displacement curve according to the Zhao model, the combined behaviour of the plate and bolt can be assembled manually. In this case, since $F_u > F_{y,b}$, failure is expected to occur in the bolt. Therefore, the corresponding forces and displacements can be determined to construct the full force–displacement curve of the specimen.

$F_0 = 0\text{kN}$	$F_1 = F_y = 35,93\text{kN}$	$F_2 = F_h = 53,64\text{kN}$	$F_3 = F_{y,b} = 118,63\text{kN}$	$F_4 = F_{u,b} = 135,462\text{kN}$
$\Delta_0 = 0\text{mm}$	$\Delta_1 = \Delta_y$ $+\Delta_{y,b} \cdot \frac{F_y}{F_{y,b}}$ $= 1,583\text{mm}$	$\Delta_2 = \Delta_h$ $+\Delta_{y,b} \cdot \frac{F_h}{F_{y,b}}$ $= 2,63\text{mm}$	$\Delta_3 = \Delta_h + \Delta_{y,b}$ $+\frac{(F_{y,b}-F_h)(\Delta_m-\Delta_h)}{(F_m-F_h)}$ $= 37,38\text{mm}$	$\Delta_4 = \Delta_h + \Delta_{y,b}$ $+\frac{(F_{u,b}-F_h)(\Delta_m-\Delta_h)}{(F_m-F_h)}$ $= 39,88\text{mm}$

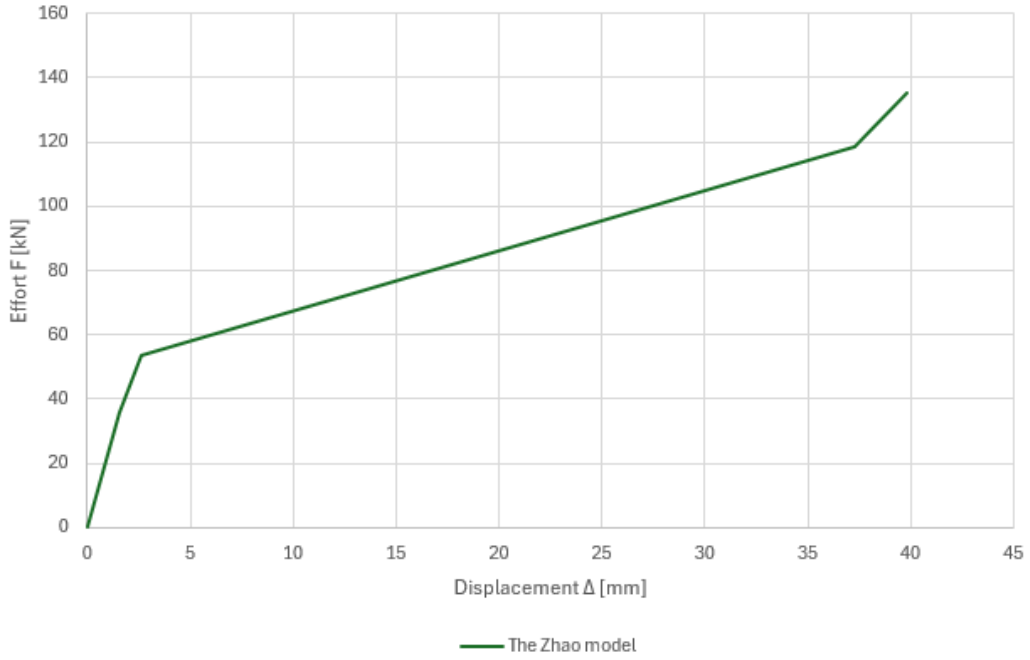

Figure 3: The force-displacment curve with Zhao model

A.3 Application of the Neutelers model

The Neutelers model uses different geometric parameters compared to the previous model. These parameters need to be calculated.

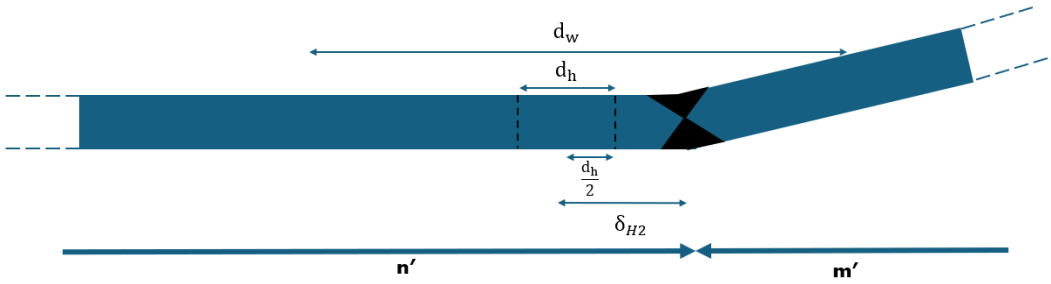

Figure 4: The information to understand parameters from Neutelers model

First, the additional geometrical parameters are calculated.

$$l_{min,req} = l_{nut} + 2 \cdot l_{washer} + d_{plate} + t_f = 13 + 2 \cdot 4 + 40 + 8 = 69\text{mm}$$
$$C = \frac{b}{2} - e - \frac{t_w}{2} - h_f = 80\text{mm}$$

These parameters allow for the calculation of the stiffness of both the bolt and the plate. Subsequently, the ratio between these two stiffnesses is obtained and used to determine the value of δ_{H1} and δ_{H2}.

$$k_{plate} = \frac{0{,}9 \cdot l_{eff} \cdot t_f^3}{C^3} = 0,1395\text{mm}$$
$$k_{bolt} = \frac{1{,}6 \cdot A_s}{l_{min,req}} = \frac{1{,}6 \cdot 156{,}82}{69} = 3,636\text{mm}$$
$$k_{rel} = \frac{k_{bolt}}{k_{plate}} = 26,0688$$

$$\delta_{H1} = 1,05 \cdot ln(k_{rel}) - 1 = 2,424\text{mm}$$
$$\delta_{H2} = d_w \cdot (0,09 \cdot ln(k_{rel}) - 0,015) = 8,353\text{mm}$$

These last two parameters are calculated using an empirical formula derived from a combination of experimental data and a parametric study. Officially, these parameters define the position of the plastic hinges, as illustrated by δ_{H2} in Figure 4.

These two important parameters introduce by this method permits to calculate a better approximation of the two parameters m' and n'.

$$m' = C - \delta_{H1} - \delta_{H2} = 69,22\text{mm}$$
$$n' = n + \delta_{H2} = 33,35\text{mm}$$

All the geometrical data are now known. The two parameters introduced to simplify the expression of the resistance can now be determined, and the bending moment is calculated in the same manner as previously.

$$G = (2 \cdot \delta_{H2} - d_h)^3 + (d_w - d_h)^2 \cdot (6 \cdot \delta_{H2} + d_h + 2 \cdot d_w - 12 \cdot n') = -39\,188\text{mm}^3$$
$$\zeta = 2 \cdot \delta_{H2} - 3 \cdot d_h + 2 \cdot d_w = 22,71\text{mm}$$
$$M_{pl,1,Rd} = M_{pl,2,Rd} = \frac{L_{eff} \cdot t_f^2 \cdot f_y}{4} = 915\,120\text{Nmm}$$

The final step consists in calculating the resistance for the three failure modes. The formulas for modes 2 and 3 remain unchanged from the previous approach. However, the formula for failure mode 1 has been improved by Neutelers to better reflect reality, incorporating all the enhancements introduced in the method.

$$F_1 = M_{pl,1,Rd} \cdot \frac{(4 \cdot G - 2 \cdot \zeta \cdot (d_w - 2 \cdot \delta_{H2})^2)}{m' \cdot G + n' \cdot \zeta \cdot (d_w - 2 \cdot \delta_{H2})^2} = 58,47\text{kN}$$
$$F_2 = \frac{2 \cdot M_{pl,2,Rd} \cdot n' \cdot B_{T,Rd} \cdot n_{bolt}}{n' + m'} = 122,75\text{kN}$$
$$F_3 = 2 \cdot B_{T,Rd} = 322,658\text{kN}$$

In conclusion, the overall resistance is defined as the minimum of the three calculated forces. In this case, once again, failure mode 1 governs the response.

$$F_{T,Rd} = min(F_1; F_2; F_3) = 58,47\text{kN}$$

A.4 Application of the Struik and De Back model

The last model considered for application to specimen T-S-HR-8 is the Struik and De Back model.

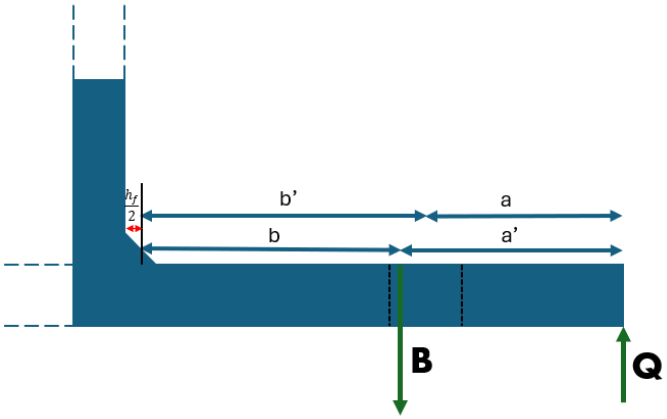

Figure 5: The information to understand parameters from Struik and De Back model

As explained previously, the main modification in this method, compared to the others, lies in the position of the concentrated force. Consequently, new geometrical parameters must be calculated. Furthermore, while the Eurocode 3 assumes that the plastic hinge near the weld is located at 0.8 times the weld length, in this model it is considered to be at 0.5 times the weld length.

$$
\begin{aligned}
a &= e = 25\text{mm} \\
b &= \tfrac{B-t_w}{2} - e - \tfrac{h_f}{2} = 86,25\text{mm} \\
a' &= a + \tfrac{d_b}{2} = 25 + \tfrac{16}{2} = 33\text{mm} \\
b' &= b - \tfrac{d_b}{2} = 86,25 - \tfrac{16}{2} = 78,25\text{mm}
\end{aligned}
$$

Here, a factor p is introduced, primarily used for T-stubs fixed with multiple rows of bolts. The factor p indicates that the developed mechanism acts along a line, and the method is simplified by considering the width of the T-stub corresponding to a single row of bolts.

$$
p = \tfrac{2 \cdot L}{n_{bolt}} = 155\text{mm}
$$

The bending moment is recalculated as before, and a factor δ is obtained. This factor represents the ratio of the net cross-sectional area of the flange at the bolt line to the gross cross-sectional area at the web face.

$$
\begin{aligned}
M_{pl,Rd} &= \tfrac{p \cdot t_f^2 \cdot f_y}{4} = 915\,120\text{Nmm} \\
\delta &= 1 - \tfrac{d_h}{p} = 1 - \tfrac{18}{155} = 0,8838
\end{aligned}
$$

Next, the equilibrium of the specimen is established to identify the different cases to consider: two moment equilibrium equations and one force equilibrium equation for the entire T-stub. By solving these equilibrium conditions, the three possible force scenarios are determined.

$$
\begin{aligned}
F_{T,1,Rd} &= \tfrac{1+\delta}{2 \cdot b'} \cdot (p \cdot t_f^2 \cdot f_y) = \tfrac{1+0,8838}{2 \cdot 78,25} \cdot (155 \cdot 8^2 \cdot 369) = 44,063\text{kN} \\
F_{T,2,Rd} &= \tfrac{2 \cdot a' \cdot B_{T,Rd}}{a'+b'} + \tfrac{p \cdot f_y \cdot t_f^2}{2 \cdot (a'+b')} = \tfrac{2 \cdot 33 \cdot 161\,329}{33+78,25} + \tfrac{155 \cdot 369 \cdot 8^2}{2 \cdot (33+78,25)} = 112,161\text{kN} \\
F_{T,3,Rd} &= 2 \cdot B_{T,Rd} = 2 \cdot 161\,329 = 322,658\text{kN}
\end{aligned}
$$

A certain similarity can be observed between the formulas derived in this development and those used in the Eurocode 3.

$$
F_{T,Rd} = min(F_{T,1,Rd}; F_{T,2,Rd}; F_{T,3,Rd}) = 44,063\text{kN}
$$

B Comparison table between the parameters t_f/C and $(t_f/C)'$

	Name	t_f/C	$(t_f/C)'$
1	T-16-01-07-06	0,1	244,905368
2	T-14-01-07-075	0,1	261,155017
3	T-16-01-07-09	0,1	309,412309
4	T-16-01-09-06	0,1	171,881912
5	T-14-01-09-075	0,1	181,022701
6	T-18-01-09-09	0,1	234,458181
7	T-18-01-1-06	0,1	161,60456
8	T-16-01-1-075	0,1	170,403352
9	T-20-01-1-09	0,1	220,076833
10	T-16-02-07-06	0,2	46,7430758
11	T-12-02-07-075	0,2	51,5609605
12	T-12-02-07-09	0,2	56,98843
13	T-16-02-09-06	0,2	30,3432513
14	T-16-02-09-075	0,2	34,6780015
15	T-14-02-09-09	0,2	36,7599104
16	T-16-02-1-06	0,2	25,5663465
17	T-16-02-1-075	0,2	29,2186817
18	T-16-02-1-09	0,2	32,2943324
19	T-16-03-07-06	0,3	20,0677225
20	T-20-03-07-075	0,3	23,0767505
21	T-16-03-07-09	0,3	25,3487021
22	T-16-03-09-06	0,3	12,2525186
23	T-14-03-09-075	0,3	13,8627548
24	T-16-03-09-09	0,3	15,4768656
25	T-16-03-1-06	0,3	10,0826095
26	T-16-03-1-075	0,3	11,5229823
27	T-18-03-1-09	0,3	13,0644529

Table 3: Comparison between the parameter t_f/C and $(t_f/C)'$

C The application of the models on the specimens of the parametric study

C.1 Efforts for the different failure mode

		Base			T-stub			
	Name	$F_{Rd,0}$ [kN]	$F_{Rd,1}$ [kN]	$F_{Rd,2}$ [kN]	$F_{Rd,1}$ [kN]	$F_{Rd,2}$ [kN]	F_{Rd} [kN]	F_{Pl} Real [kN]
1	T-16-01-07-06	48,61	104,89	131,91	**37,76**	110,25	37,76	46,22
2	T-14-01-07-075	27,14	58,51	100,19	**32,91**	92,27	32,91	39,93
3	T-16-01-07-09	21,59	46,58	113,10	**37,76**	110,25	37,76	48,31
4	T-16-01-09-06	62,81	134,43	128,93	**48,40**	98,96	48,40	54,47
5	T-14-01-09-075	35,09	75,01	94,46	**42,20**	83,41	42,20	49,28
6	T-18-01-09-09	31,46	66,07	119,32	**53,52**	114,74	53,52	63,73
7	T-18-01-1-06	78,78	165,13	149,66	**59,45**	110,08	59,45	67,16
8	T-16-01-1-075	44,74	95,49	110,13	**53,71**	95,16	53,71	60,39
9	T-20-01-1-09	38,96	84,00	131,08	**68,04**	125,14	68,04	73,08
10	T-16-02-07-06	95,15	212,76	199,99	**76,59**	167,16	76,59	102,75
11	T-12-02-07-075	45,03	100,12	117,23	**56,32**	107,96	56,32	79,85
12	T-12-02-07-09	31,27	69,53	110,76	**56,32**	107,96	56,32	80,82
13	T-16-02-09-06	123,51	271,83	203,49	**97,86**	156,19	97,86	117,16
14	T-16-02-09-075	79,05	173,97	176,88	**97,86**	156,19	97,86	114,9
15	T-14-02-09-09	47,80	105,25	134,05	**85,25**	128,90	85,25	112,16
16	T-16-02-1-06	137,70	301,37	207,49	**108,49**	152,62	108,49	134,04
17	T-16-02-1-075	88,13	192,88	176,63	**108,49**	152,62	108,49	131,98
18	T-16-02-1-09	61,20	133,94	159,86	**108,49**	152,62	108,49	139,18
19	T-16-03-07-06	139,74	323,77	241,55	**116,56**	201,89	116,56	152,42
20	T-20-03-07-075	113,21	265,49	310,33	**149,34**	285,77	149,34	212,73
21	T-16-03-07-09	62,11	143,90	207,13	**116,56**	201,89	116,56	154,45
22	T-16-03-09-06	182,21	412,29	252,08	**148,42**	193,49	148,42	186,5
23	T-14-03-09-075	101,32	229,69	178,42	**129,20**	157,54	129,20	167,49
24	T-16-03-09-09	80,98	183,24	201,22	**148,42**	193,49	148,42	190,96
25	T-16-03-1-06	203,46	456,57	259,78	**164,37**	191,08	164,37	210,53
26	T-16-03-1-075	130,22	292,21	221,13	**164,37**	191,08	164,37	204,08
27	T-18-03-1-09	102,24	221,53	238,30	**179,44**	227,50	179,44	237,83

C.2 Efforts for the different failure mode with the real value of m

		Base			T-stub			
	Name	$F_{Rd,0}$ [kN]	$F_{Rd,1}$ [kN]	$F_{Rd,2}$ [kN]	$F_{Rd,1}$ [kN]	$F_{Rd,2}$ [kN]	F_{Rd} [kN]	F_{Pl} Real [kN]
1	T-16-01-07-06	56,8	129,15	146,61	**46,50**	122,54	46,50	46,22
2	T-14-01-07-075	31,72	72,06	110,87	**40,54**	102,1	40,54	39,93
3	T-16-01-07-09	25,75	58,64	127,43	**47,53**	124,22	47,53	48,31
4	T-16-01-09-06	70,24	156,98	139,97	**56,51**	107,43	56,51	54,47
5	T-14-01-09-075	39,55	88,28	102,81	**49,66**	90,78	49,66	49,28
6	T-18-01-09-09	34,50	74,61	127,97	**60,44**	123,05	60,44	63,73
7	T-18-01-1-06	84,57	182,18	158,16	**65,59**	116,33	65,59	67,16
8	T-16-01-1-075	48,47	107,63	117,01	**60,54**	101,11	60,54	60,39
9	T-20-01-1-09	41,96	94,74	139,06	**76,74**	132,76	76,74	73,08
10	T-16-02-07-06	111,32	271,14	216,99	**97,61**	181,36	97,61	102,75
11	T-12-02-07-075	46,22	109,52	118,68	**61,60**	109,28	61,60	79,85
12	T-12-02-07-09	32,99	78,44	113,54	**63,54**	110,67	63,54	80,82
13	T-16-02-09-06	139,42	328	218,4	**118,08**	167,63	118,08	117,16
14	T-16-02-09-075	82,944	193,69	181,99	**108,95**	160,7	108,95	114,9
15	T-14-02-09-09	53,25	125,24	142,31	**101,44**	136,83	101,45	112,16
16	T-16-02-1-06	155,61	362,42	223,52	**130,47**	164,41	130,47	134,04
17	T-16-02-1-075	98,25	228,52	188,73	**128,54**	163,08	128,54	131,98
18	T-16-02-1-09	68,23	158,69	170,82	**128,54**	163,08	128,54	139,18
19	T-16-03-07-06	128,45	319,99	232,49	**115,19**	194,32	115,20	152,42
20	T-20-03-07-075	124,62	328,57	325,08	**184,82**	299,35	184,82	212,73
21	T-16-03-07-09	59,85	150,349	203,72	**121,78**	198,58	121,78	154,45
22	T-16-03-09-06	184,58	449,75	253,72	**161,91**	194,75	161,91	186,5
23	T-14-03-09-075	96,75	234,36	174,54	**131,83**	154,12	131,83	167,49
24	T-16-03-09-09	80,18	194,74	200,22	**157,74**	192,53	157,74	190,96
25	T-16-03-1-06	205,3	493,11	261	**177,52**	191,98	177,52	210,53
26	T-16-03-1-075	131,39	315,59	222,18	**177,52**	191,98	177,52	204,08
27	T-18-03-1-09	112,1	255,98	250,54	**207,35**	239,19	207,35	237,83

C.3 Efforts improved with the modification of the parameter e_w

		Base		T-stub		
	Name	$e_w = d_w/4$ [kN]	$e_w = 3 \cdot d_w/8$ [kN]	$e_w = d_w/4$ [kN]	$e_w = 3 \cdot d_w/8$ [kN]	F_{pl} Real [kN]
1	T-16-01-07-06	104,89	109,45	37,76	39,40	46,22
2	T-14-01-07-075	58,51	61,03	32,91	34,33	39,93
3	T-16-01-07-09	46,58	48,61	37,76	39,40	48,31
4	T-16-01-09-06	134,43	139,62	48,40	50,26	54,47
5	T-14-01-09-075	75,01	77,85	42,20	43,79	49,28
6	T-18-01-09-09	66,07	67,85	53,52	54,95	63,73
7	T-18-01-1-06	165,13	169,38	59,45	60,98	67,16
8	T-16-01-1-075	95,49	99,02	53,71	55,70	60,39
9	T-20-01-1-09	84,00	87,68	68,04	71,02	73,08
10	T-16-02-07-06	212,76	226,95	76,59	81,70	102,75
11	T-12-02-07-075	100,12	106,33	56,32	59,81	79,85
12	T-12-02-07-09	69,53	73,84	56,32	59,81	80,82
13	T-16-02-09-06	271,83	287,10	97,86	103,36	117,16
14	T-16-02-09-075	173,97	183,75	97,86	103,36	114,9
15	T-14-02-09-09	105,25	111,17	85,25	90,05	112,16
16	T-16-02-1-06	301,37	317,22	108,49	114,20	134,04
17	T-16-02-1-075	192,88	203,02	108,49	114,20	131,98
18	T-16-02-1-09	133,94	140,99	108,49	114,20	139,18
19	T-16-03-07-06	323,77	353,43	116,56	127,24	152,42
20	T-20-03-07-075	265,49	292,61	149,34	164,59	212,73
21	T-16-03-07-09	143,90	157,08	116,56	127,24	154,45
22	T-16-03-09-06	412,29	443,13	148,42	159,53	186,5
23	T-14-03-09-075	229,69	247,10	129,20	138,99	167,49
24	T-16-03-09-09	183,24	196,95	148,42	159,53	190,96
25	T-16-03-1-06	456,57	488,13	164,37	175,73	210,53
26	T-16-03-1-075	292,21	312,40	164,37	175,73	204,08
27	T-18-03-1-09	221,53	231,62	179,44	187,61	237,83

C.4 Efforts for the $F_{Rd,1}$ with different method

	Name	F_{pl} Real [kN]	Eurocode [kN]	e_w improved [kN]	m improved [kN]	m and e_w improved [kN]
1	T-16-01-07-06	46,22	37,76	39,40	46,50	46,50
2	T-14-01-07-075	39,93	32,91	34,33	40,54	40,54
3	T-16-01-07-09	48,31	37,76	39,40	47,53	47,53
4	T-16-01-09-06	54,47	48,40	50,26	56,51	56,51
5	T-14-01-09-075	49,28	42,20	43,79	49,66	49,66
6	T-18-01-09-09	63,73	53,52	54,95	60,44	60,44
7	T-18-01-1-06	67,16	59,45	60,98	65,59	65,59
8	T-16-01-1-075	60,39	53,71	55,70	60,54	60,54
9	T-20-01-1-09	73,08	68,04	71,02	76,74	76,74
10	T-16-02-07-06	102,75	76,59	81,70	97,61	97,61
11	T-12-02-07-075	79,85	56,32	59,81	61,60	61,60
12	T-12-02-07-09	80,82	56,32	59,81	63,54	63,54
13	T-16-02-09-06	117,16	97,86	103,36	118,08	118,08
14	T-16-02-09-075	114,9	97,86	103,36	108,95	108,95
15	T-14-02-09-09	112,16	85,25	90,05	101,45	101,45
16	T-16-02-1-06	134,04	108,49	114,20	130,47	130,47
17	T-16-02-1-075	131,98	108,49	114,20	128,54	128,54
18	T-16-02-1-09	139,18	108,49	114,20	128,54	128,54
19	T-16-03-07-06	152,42	116,56	127,24	115,20	115,20
20	T-20-03-07-075	212,73	149,34	164,59	184,82	184,82
21	T-16-03-07-09	154,45	116,56	127,24	121,78	121,78
22	T-16-03-09-06	186,5	148,42	159,53	161,91	161,91
23	T-14-03-09-075	167,49	129,20	138,99	131,83	131,83
24	T-16-03-09-09	190,96	148,42	159,53	157,74	157,74
25	T-16-03-1-06	210,53	164,37	175,73	177,52	177,52
26	T-16-03-1-075	204,08	164,37	175,73	177,52	177,52
27	T-18-03-1-09	237,83	179,44	187,61	207,35	207,35

C.5 Efforts for the improved models

	Name	Zhao [kN]	Struik and De Back [kN]	Neutelers [kN]	F_{pl} Real [kN]
1	T-16-01-07-06	57,63	32,72	**42,51**	46,22
2	T-14-01-07-075	50,05	28,75	**37,51**	39,93
3	T-16-01-07-09	57,63	32,72	**42,53**	48,31
4	T-16-01-09-06	74,14	41,92	**52,77**	54,47
5	T-14-01-09-075	64,42	36,90	**46,40**	49,28
6	T-18-01-09-09	81,58	46,80	**57,23**	63,73
7	T-18-01-1-06	90,69	51,91	**62,60**	67,16
8	T-16-01-1-075	82,39	46,52	**57,94**	60,39
9	T-20-01-1-09	105,33	57,16	**72,77**	73,08
10	T-16-02-07-06	115,05	66,49	**93,19**	102,75
11	T-12-02-07-075	**83,79**	49,21	69,22	79,85
12	T-12-02-07-09	**83,79**	49,21	69,51	80,82
13	T-16-02-09-06	138,32	84,88	**112,90**	117,16
14	T-16-02-09-075	138,32	84,88	**113,38**	114,9
15	T-14-02-09-09	**114,48**	74,24	99,84	112,16
16	T-16-02-1-06	**140,94**	94,07	122,98	134,04
17	T-16-02-1-075	140,94	94,07	**123,48**	131,98
18	T-16-02-1-09	**140,94**	94,07	123,83	139,18
19	T-16-03-07-06	**165,12**	101,37	133,98	152,42
20	T-20-03-07-075	**222,86**	128,08	177,11	212,73
21	T-16-03-07-09	**165,12**	101,37	136,93	154,45
22	T-16-03-09-06	**174,07**	128,92	161,79	186,5
23	T-14-03-09-075	142,61	112,04	**144,39**	167,49
24	T-16-03-09-09	**174,07**	128,92	164,93	190,96
25	T-16-03-1-06	**179,71**	142,71	176,06	210,53
26	T-16-03-1-075	**179,71**	142,71	177,96	204,08
27	T-18-03-1-09	**211,64**	160,73	97,99	237,83